H. M. Rønnow: Magnetic Properties of Holmium–Erbium Alloys

Magnetic Properties of Holmium–Erbium Alloys

Henrik Moodysson Rønnow

Master's Thesis
February 21, 1997

Ørsted Laboratory,
Niels Bohr Institute,
University of Copenhagen

Foreword

This thesis is dedicated to the memory of my late professor A.R. Mackintosh — meant as a student's tribute to his work of great insight. Through our unfortunately short acquaintance I owe Allan my interest in the field of solid state physics in general and rare earth magnetism in particular.

I am grateful to my supervisors Jens Jensen from the Ørsted Laboratory, Niels Bohr Institute and Des McMorrow from the Solid state department, Risø National Laboratory.

For their help and suggestions on various problems, I also wish to thank the people in the solid state department, my fellow students and my family.

The work falls into three main parts, namely experiments, theory and calculations. On the other hand the examined system shows several different interesting features. I have chosen to start by supplying the background knowledge, occasionally mentioning the implications on the features. Afterwards I discuss each of the features individually. This procedure has led to some overlapping in the report, but on the other hand I found it the most instructive way.

Available on request through author at

Solid State Departement
Risø National Laboratory
P. O. Box 49, 4000 Roskilde
Denmark

Document typeset in LaTeX 2$_\varepsilon$
Printed by Grafisk Service, Risø

ISBN 87-550-2221-9

Contents

Chapter 1

General properties of Ho and Er

Prior to a discussion of the effect of alloying the two elements, their individual respective properties shall be outlined. Both Ho and Er belongs to the rare earth series, which in terms of electronic configuration are characterized by the filling of the $4f$ shell with 0 to 14 electrons.

The electronic configuration of an individual rare earth atom can be calculated by means of local density theory as formulated by Hohenberg and Kohn (1964), Kohn and Sham (1965). As a result it is seen that the $4f$ electrons are close to the nuclei, well shielded by the 5d and 6s electrons as is illustrated in figure 1.1.

Of great importance to the magnetic properties is the spin orbit coupling, which for the $4f$ electrons is accurately described by the *Russell–Saunders* coupling scheme. Within this procedure the individual electron spins are coupled by the exchange interaction into a total spin $\boldsymbol{S} = \sum_i \boldsymbol{s}_i$ and the orbital angular momenta are coupled by the coulomb interaction into a total angular momentum $\boldsymbol{L} = \sum_i \boldsymbol{l}_i$. These two couplings are sufficiently large to confine the system to the ground state values of S and L which are found by *Hund's rules*:

1. Maximize S.

2. Maximize L within the constraints of rule 1.

3. $J = |L \mp S|$ with the sign changing at half filling of the shell.

The spin and orbital angular momentum operators are thus combined into a total angular momentum operator $\boldsymbol{J} = \boldsymbol{L} + \boldsymbol{S}$ of length $J = |L \mp S|$. The actual values for holmium and erbium are summarized in table 1.1.

Within the ground state multiplet $\{|JLSM_J\rangle\}$ the *Wigner–Eckart* theorem implies, that the matrix elements of any operator can be related to those of $\boldsymbol{J}$. Taking the electronic gyro magnetic factor g_0 as 2 this provides some very

Figure 1.1: Radial wave functions for Ce illustrating the confinement of the $4f$ electrons.

	$4f^n$	L	S	J	g	Δ[K]
Ho	10	6	2	8	$\frac{5}{4}$	7500
Er	11	6	$\frac{3}{2}$	$\frac{15}{2}$	$\frac{6}{5}$	9350

Table 1.1: Values for the spin orbit coupling in holmium and erbium. Δ is the energy to the first excited multiplet.

useful relations between the quantum operators $\boldsymbol{S}$, $\boldsymbol{L}$ and $\boldsymbol{J}$. It is not necessary to put $g_0 \simeq 2$, but the simplicity of the resulting expressions justifies the approximation. The Wigner–Eckart theorem gives:

$$\langle JLSM_J|\boldsymbol{L}+2\boldsymbol{S}|JLSM_J\rangle = g_{\text{Landé}}(JLS)\langle JLSM_J|\boldsymbol{J}|JLSM_J\rangle, \tag{1.1}$$

where the *Landé factor* (in the following denoted just g) is

$$g_{\text{Landé}}(JLS) = \frac{3}{2} + \frac{S(S+1)-L(L+1)}{2J(J+1)}. \tag{1.2}$$

Bearing in mind, that it is only valid within the ground state multiplet, the matrix element proportionality along with two implications can be written in direct operator form:

$$\begin{aligned} g\boldsymbol{J} &= \boldsymbol{L}+2\boldsymbol{S} \\ \boldsymbol{L} &= (2-g)\boldsymbol{J} \\ \boldsymbol{S} &= (g-1)\boldsymbol{J}. \end{aligned} \tag{1.3}$$

1.1 Rare earth metals

When combined into a solid metal the well embedded $4f$ electrons remain localized and the coupling of angular momenta take place as described for the individual atom. The conduction electron gas is built from 5d and 6s electrons moving in delocalized *Bloch states*. The direct magnetic contribution from the conduction gas is negligible, but it plays an important role as mediator of magnetic interaction between the localized $4f$ angular momenta.

Most of the rare earths form hexagonal closed packed (*hcp*) or double hexagonal closed packed (*dhcp*) lattices, both of which can be viewed as closed packed trigonal symmetry planes (*basal planes*) stacked with a translation scheme as ABAB or ABAC respectively. Actually both the fcc structure of Yb and Ce(α,γ) and the rhombohedral symmetry of Sm can be identified with stacking of closed packed planes in the sequence ABCABC and ABABCBCAC respectively. Belonging to the heavy rare earths, both holmium and erbium have *hcp* structure with lattice parameters a and c given in table 4.2.

Figure 1.2: The hcp and dhcp lattices

The hexagonal closed packed lattice can be treated as a simple hexagonal *Bravais lattice* with two atoms per unit cell. The three primitive axes are defined as:

$$\begin{aligned} \boldsymbol{a}_1 &= a\hat{\boldsymbol{x}} \\ \boldsymbol{a}_2 &= a(\frac{-\hat{\boldsymbol{x}}}{2} + \frac{\sqrt{3}}{2}\hat{\boldsymbol{y}}) \\ \boldsymbol{a}_3 &= c\hat{\boldsymbol{z}}. \end{aligned} \tag{1.4}$$

In the discussion of the magnetic anisotropy it is convenient to distinguish between the directions along which the nearest neighbours lie and those in be-

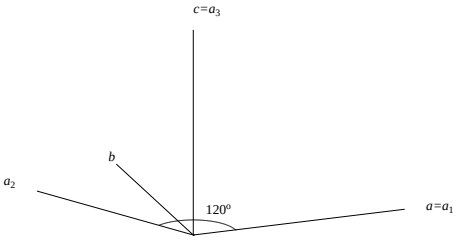

(a) Real space (b) Reciprocal space

Figure 1.3: The real and reciprocal hexagonal lattice notation

tween. Therefore the crystal directions are defined orthogonal and parallel to $\{\hat{\boldsymbol{x}}, \hat{\boldsymbol{y}}, \hat{\boldsymbol{z}}\}$ respectively:

$$\begin{aligned} \boldsymbol{a} &= a\hat{\boldsymbol{x}} = \boldsymbol{a}_1 \\ \boldsymbol{b} &= a\hat{\boldsymbol{y}} = \boldsymbol{a}_1 + 2\boldsymbol{a}_2 \\ \boldsymbol{c} &= c\hat{\boldsymbol{z}} = \boldsymbol{a}_3. \end{aligned} \tag{1.5}$$

For a crystal with more than one atom per unit cell, the relative position $\boldsymbol{d}_n$ of each site is specified with respect to the origin of the unit cell. In the *hcp* crystal, the two atoms are situated at:

$$\begin{aligned} \boldsymbol{d}_0 &= \mathbf{0} \\ \boldsymbol{d}_1 &= \frac{2\boldsymbol{a}_1}{3} + \frac{\boldsymbol{a}_2}{3} + \frac{\boldsymbol{a}_3}{2} = \frac{\boldsymbol{a}}{2} + \frac{\boldsymbol{b}}{6} + \frac{\boldsymbol{c}}{2}. \end{aligned} \tag{1.6}$$

The *reciprocal lattice* is defined with respect to the primitive axes through $\exp i\boldsymbol{k} \cdot \boldsymbol{R} = 1$ for $\boldsymbol{R}$ and $\boldsymbol{k}$ belonging to the lattices spanned by $\{\boldsymbol{a_1}, \boldsymbol{a_2}, \boldsymbol{a_3}\}$ and $\{\boldsymbol{b_1}, \boldsymbol{b_2}, \boldsymbol{b_3}\}$ respectively. Though inconsistent, it is standard to call the reciprocal primitive vectors $\boldsymbol{b_1}$ and $\boldsymbol{b_3}$ for $\boldsymbol{a}^*$ and $\boldsymbol{c}^*$ respectively despite the fact that they are defined from $\{\boldsymbol{a_1}, \boldsymbol{a_2}, \boldsymbol{a_3}\}$. It is convenient to specify positions in the reciprocal space in terms of *Miller indices* (h, k, l) where integer h, k and l correspond to reciprocal lattice points. This choice of units is referred to as reciprocal lattice units. A direction in reciprocal space is similarly written as $[h, k, l]$.

The fact that the unit cell is twice as high (in the c-direction) as the distance d between two succesive basal planes is reflected in the reciprocal space scattering, where $(0, 0, 2)$ is the first allowed reciprocal lattice point, while $(0, 0, 1)$ is extinct by the *geometric structure factor* as an artifact of the unit cell.

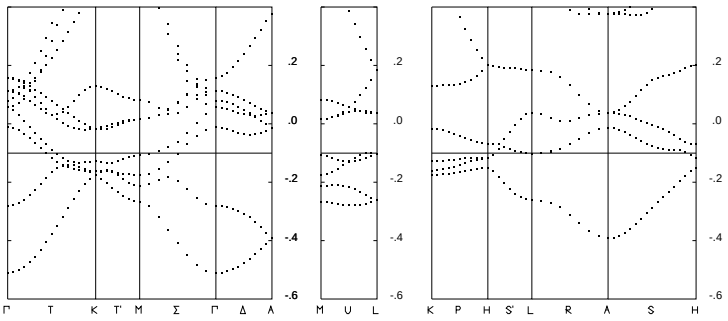

(a) Ho

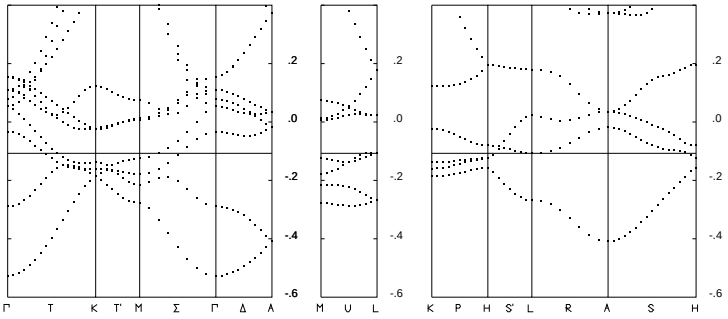

(b) Er

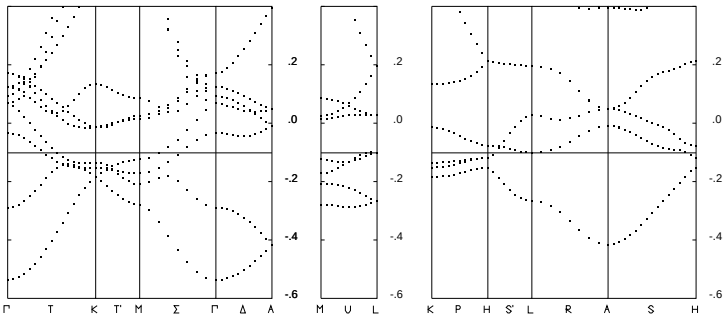

(c) Tm

Figure 1.4: Band structure in Ho, Er and Tm from top to bottom. Energies are in *Ry*. The Horizontal line in the middle is the Fermi energy.

As for the electronic configuration of the atom, local density methods such as the Linear Muffin Tin Orbital method can be used in self consistent *band structure* calculations in the metals. With help from H.L. Skriver, the band structures of Ho ($4f^{10}$), Er ($4f^{11}$) and Tm ($4f^{12}$) have been calculated, using the TB-LMTO-ASA method developed by Skriver et al. (Andersen 1975, Skriver 1984, Andersen *et al.* 1985, Andersen and Jepsen 1984) Although very similar, all three have been plotted in figure 1.4 as an illustration of how little the electronic structure changes during the filling of the $4f$ shell.

The integrated *density of states* in figure 1.5 defines the *Fermi energy* E_F as the energy where there are 6 electrons (3 for each atom in the *hcp* unit cell). There are 3 electrons per atom in the conduction bands, but the s, p and d bands

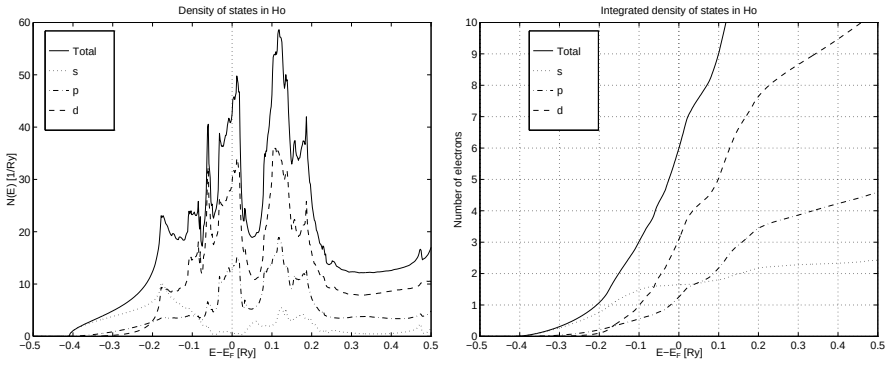

(a) Density of states (b) Number of electrons

Figure 1.5: Density of states and integrated number of electrons in Ho.

are fractionally filled as follows: $N_s = 1.54$, $N_p = 0.822$ and $N_d = 0.628$. Since there are no p electrons in the free atom, the p electrons are called s electrons, and the 3 electrons are hence equally distributed among the s and the d bands. Therefore the usual assignment $4f^n5d^26s^1$ is to be treated as a formal choice.

Though the right numerical values for the magnetic interactions are generally not accessible, some qualitative features can be understood with a knowledge of the electronic configuration. The form of the *Fermi surface* is believed to explain the periodicity of the magnetic structures as discussed in section 2.2.4 on page 22.

The Fermi surface is defined by $E(\boldsymbol{k}) = E_F$ and is found from the band structure as the intersection between the bands and the Fermi energy. However, a reasonable determination of the Fermi energy requires calculation of the band structure not only along the symmetry lines as in figure 1.4 but in a fine mesh through the reduced Brillouin zone. This quite comprehensive task has not been performed. Instead the Fermi surface of Tb is shown in figure 1.6.

As illustrated for the band structure there are only small differences in the Fermi surface for the different rare earths, and hence the Fermi surfaces of Ho,

Figure 1.6: The Fermi surface of Tb illustrating how the parallel regions between the toes result in periodic structures of periodicity $\boldsymbol{q}$.

Er and Tm can be assumed to have similar forms.

The two parallel regions separated by $\boldsymbol{q}$ are believed to be responsible for the periodicity of the structures in the rare earths (see section 2.2.4) and is therefore worth a closer examination (Keeton and Loucks 1968). The center of the dog-bone is denoted L. The axis parallel to $\boldsymbol{q}$ is the ML axis, and the axis perpendicular to $\boldsymbol{q}$ is the LH axis, both of which are seen in the band structures. The dog-bone shaped region of the Fermi surface can be identified in the band structure. The ends of the dog-bone are seen as a band crossing the Fermi surface between H and L, close to H. The width of the dog-bone is more difficult to identify, but as seen in the closeup of the band structure in figure 1.7 it is present.

The Fermi surface intersects the ML line about 1/5 from L. This corresponds qualitatively to the universal periodicity $Q(T_N) \simeq 0.28$ observed in most of the heavy rare earths.

Another interesting feature of the ML band structures is that the band dips at L. In Ho L is outside the Fermi surface, in Er it is at the Fermi surface, whereas it is just inside the Fermi surface in Tm. If this is a real feature it means, that there is a small hole in the center of the dog bone. It is however doubtful if such a hole will have any physical implications. Perhaps it can be resolved in state of the art de Haas–van Alphen measurements.

On the other hand the feature is an effect of very small energy variations, and in fact this might be one of the few cases where the Tight Binding and Atomic Sphere approximations are too coarse. The spin orbit coupling, which is not included in the presented calculations, does not split the degeneracy at L, but the coupling to other bands could result in a shift of the two degenerate energies across the Fermi energy. Therefore any further discussion of the details of the dog-bone should be done on the basis of full LMTO calculations including the spin-orbit coupling.

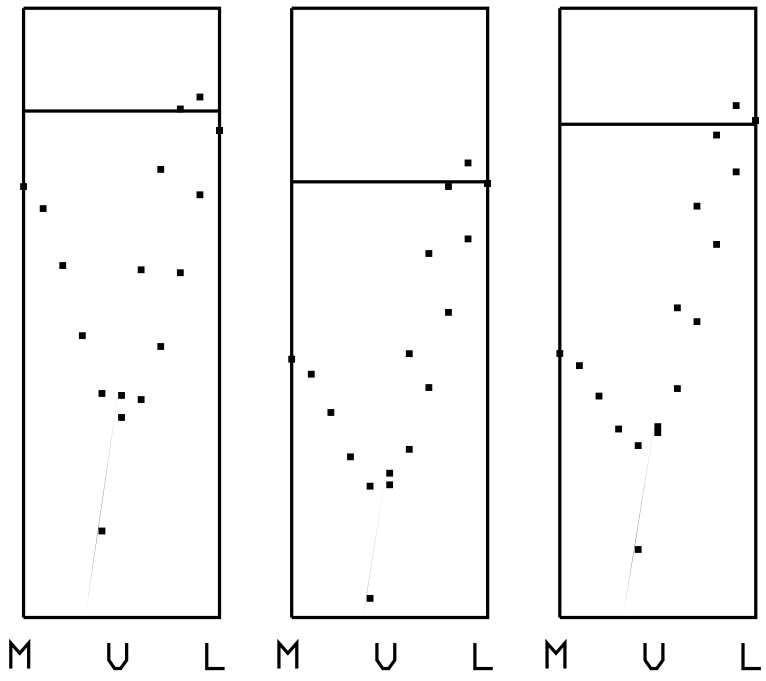

(a) Ho (b) Er (c) Tm

Figure 1.7: Closeup of band structure the vertical axis run from -0.15Ry to -0.09Ry. The Horizontal line in the middle is the Fermi energy.

1.2 Magnetic phases

The vast range of exotic and beautiful kinds of magnetic structures found in the rare earths is the result of a "competition" between different magnetic interactions acting on the $4f$ momenta of varying size.

Below the Néel temperature the rare earths order magnetically with all the magnetic moments within a particular *basal plane* aligned parallel. But the direction of the moments vary from plane to plane giving rise to different periodic structures. If the structure repeats itself m times during N double layers, the periodicity is described by $q = m/N$ given in reciprocal lattice units or $q = mc^*/N$ as a reciprocal length.

Each of the rare earths show several different structures. The periodicity of the structures decrease with decreasing temperatures, but in addition phase transitions occur where the form of the structure changes in either a first or a second order transition.

In general the periodicity is incommensurable with the lattice, but as it decreases it passes integer fractions of the lattice periodicity and a lock-in can

occur. The introduction of an external magnetic field can produce other kinds of structures thus adding an extra dimension to the phase space. Since all experiments described herein are performed in zero field, the field dependency will not be discussed.

1.2.1 Holmium

The perhaps most pronounced structure is the *helix* — a helical structure where the expectation values of $\boldsymbol{J}$ rotate with a constant angle between succeeding planes. A variant of the helix is the *cone* where the helix is lifted out of the basal plane building a constant c-axis component.

Those two structures describes the magnetism in holmium (Cowley and Bates 1988). Holmium orders magnetically below the Néel temperature $T_N = 133$ K where a helical structure is formed. The periodicity varies from $q \simeq 0.28$ at T_N to a lock-in to $q = 1/6$ around 20 K. The commensurate lock-in is supplemented by a second order transition to a cone phase where the angle of the moments to the basal plane approach 10^o in the zero temperature limit.

Magnetic fields in the c-axis will promote the cone phase. A field in the plane eventually causes a basal plane ferromagnet, but for lower fields a *fan* structure with the moments oscillating around the field axis will appear. Most interesting Jensen and Mackintosh (1992) found so-called *helifans* in intermediate fields. The helifans are periodic fractional combinations of the helix and the fan structures.

All these structures as well as magnetization and spin wave measurements are well described by the standard *spin Hamiltonian* for the rare earths.

Recent the higher harmonics have been studied in details, which have resulted in quite accurate knowledge about the types and numeric strength of interactions in the crystals. For instance, evidence of an interaction with trigonal symmetry has been seen (Simpson *et al.* 1995).

Finally the lock-in to commensurable structures has been comprehensively studied by Jensen (1996a) within the same Hamiltonian and interpreted in terms of so called *spin slip* structures (see page 39).

1.2.2 Erbium

The phases of erbium are a bit more complicated (Cowley and Jensen 1992). Below the ordering temperature $T_N = 84$ K a sinusoidally modulated c-axis (CAM) structure appears with a periodicity of approximately $q \simeq 0.29$. At a second transition temperature $T'_N = 52$ K the moments order in an elliptical *cycloid* in the ac-plane, while the periodicity decreases to $q = 1/4$ at 18 K. Below $T_C = 18$ K erbium forms a cone structure just as holmium.

Besides the interactions present in holmium, spin wave measurements indicated that anisotropic two-ion interactions play an important role (Cowley and Jensen 1993). This along with the somewhat more complicated phase diagram makes it difficult to account for the properties through the spin Hamiltonian. Partly because there are too many free parameters leaving several choices for

their numerical values, partly because there are some actual discrepancies between the model and the measurements.

For instance, the model predicts the cone phase to be only *meta-stable* with a free energy per atom about 1 meV higher than the basal plane helix. Also the basal plane high field magnetization curves are not satisfactorily described by the present model for erbium.

Spin wave measurements have only been performed at liquid He temperatures, and hence the temperature dependent interaction parameters are only well determined at this temperature.

Generally, the problem in erbium is that the relatively low $S = \frac{3}{2}$ makes the simple isotropic exchange interaction sufficiently weak, that other two-ion interactions play a substantial role. The many possible choices of such two-ion interactions cannot be uniquely distinguished with the present experimental data.

Bearing this in mind a model for the holmium–erbium alloys would be expected to be most successful when rich in holmium and at low temperatures.

1.2.3 The alloy

The magnetic properties of the rare earths are determined by the competition between different terms in the Hamiltonian. This interplay can be investigated by alloying different elements thus continuously changing the conditions of competition between the different interactions.

There exist quite a lot of work on rare earth alloys both theoretically and experimental (Larsen 1987, Larsen *et al.* 1986, 1987, 1988). The work that most directly connects to the holmium–erbium problem is presented in the following.

Magnetization measurements

Magnetization experiments have been performed on a number of compositions of holmium and erbium at liquid He temperature (Bozorth *et al.* 1968, 1972). A few of the magnetization curves are shown in figure 1.8.

It is seen, that the zero field limit of the c-axis susceptibility diverges, which means that there is a ferromagnetic ordered moment along the c-axis. This is the cone structure and the cone angle can be deduced as $M/M_S = \sin\theta$ in the limit of zero field. It was furthermore seen, that for Ho_xEr_{1-x} with $x > 30\%$ a transition from the cone phase to a pure ferromagnetic phase occurs at higher fields.

Pure Ho is very easily magnetized in the basal plane, whereas $Ho_{87.5}Er_{12.5}$, $Ho_{50}Er_{50}$ and Er have a non zero critical field until which the structures are magnetized linearly. All of the basal plane magnetization curves showed non trivial development which indicates, that the zero field cone passes several intermediate structures on the way to a basal plane ferromagnet.

In Ho the b-axis is most easily magnetized in agreement with the *crystal field easy axis* being in that direction. In Er the a-axis is preferred, whereas in $Ho_{50}Er_{50}$ the competing easy axes of Ho and Er result in similar magnetization

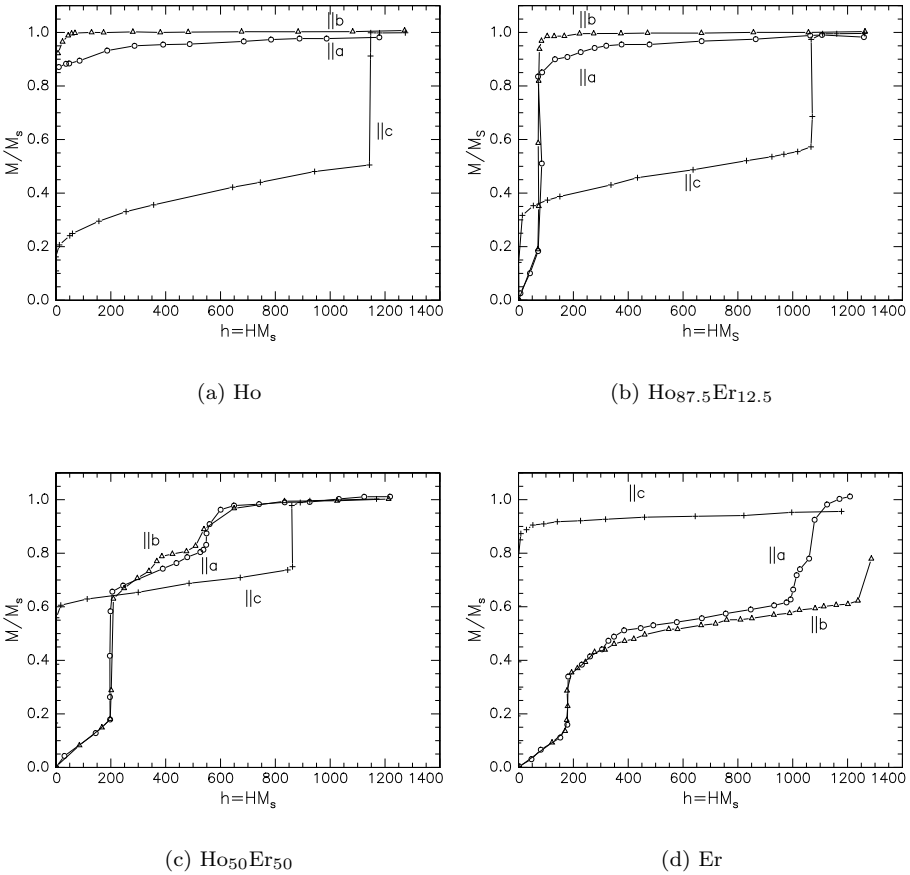

(a) Ho

(b) $Ho_{87.5}Er_{12.5}$

(c) $Ho_{50}Er_{50}$

(d) Er

Figure 1.8: Magnetization curves by Bozorth *et al.* (1972)

curves for the two axes. The competition between the a and b-axis might be responsible for the formation of an intermediate phase in $Ho_{50}Er_{50}$ as discussed in section 5.3.2.

Finally Bozorth *et al.* (1972) presents a measurement of the transition temperatures T_N and T_C as shown in figure 1.9 The linear behaviour of T_N and the rise in T_C is in complete agreement with the present neutron scattering results.

Neutron scattering from $Ho_{50}Er_{50}$

A single crystal of $Ho_{50}Er_{50}$ has been studied using thermal (1.012Å) neutron diffraction at the four circle diffractometer TAS2, Risø by Howard and Bohr (1991). They measured the relative intensities of 50 nuclear peaks $\boldsymbol{\tau}$ and the corresponding 100 magnetic peaks $\boldsymbol{\tau} \pm \boldsymbol{q}$, where $\boldsymbol{q}$ is the periodicity of the

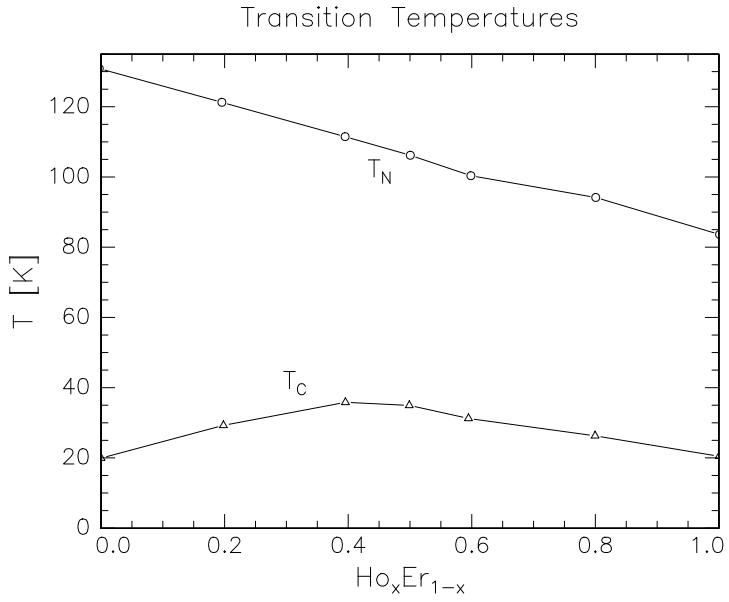

Figure 1.9: Transition temperatures T_N and T_C measured by magnetization

magnetic structure.

The data were corrected with the *Lorenz factor* $\sin^{-1} 2\theta$ coming from the spectrometer resolution (page 53) and for absorption. *Extinction* corrections were estimated to be less than 5%. Using various analytic structures the intensity of each peak was calculated from the scattering cross-section expression:

$$I(\boldsymbol{\kappa})e^{2W(\kappa)}/A = \left|\sum_j b_j e^{i\boldsymbol{\kappa}\cdot\boldsymbol{r}_j}\right|^2 + \left|\sum_j \frac{\hbar\gamma e^2}{mc^2}\tfrac{1}{2}gF(\boldsymbol{\kappa})\hat{\boldsymbol{\kappa}}\times(\boldsymbol{J}_j\times\hat{\boldsymbol{\kappa}})e^{i\boldsymbol{\kappa}\boldsymbol{r}_j}\right|^2, \quad (1.7)$$

where A is a scaling factor, $b_j \simeq 0.8055\times10^{-12}cm$ the nuclear scattering length taken to be the average between Ho and Er. $W(\kappa) \simeq B\kappa^2$ is the *Debye–Waller factor*, γ the gyro magnetic ratio of the neutron, g the *Landé factor*, $F(\boldsymbol{\kappa})$ the *magnetic form factor* and $\boldsymbol{J}_j$ the angular momentum of the j'th plane.

The intensities calculated so were fitted to the experimental data using least squares. Among the structures investigated were the basal plane *helix*, a cone structure with either common or different cone angles for the two elements. as well as a *cycloidal* structure and finally a "distinguishable modulated c-axis basal plane spiral structure". This structure must be a binary tilted helix with different tilt angles θ'_{Ho} and θ'_{Er} respectively.

As depicted in figure 1.10, three distinct phases were observed. The low temperature phase characterized by a ferromagnetic addition to the $(1,0,0)$ peak was found to be a single cone structure with identical cone angles $\theta_{\mathrm{Ho}} =$

Figure 1.10: Previously proposed magnetic phases of $Ho_{50}Er_{50}$ as deduced from neutron and x-ray scattering experiments (Howard and Bohr 1991, Pengra *et al.* 1994)

$\theta_{Er} \simeq 20°$, only qualitatively in agreement with the approximately 35° found in both earlier magnetization measurements, the present data and predicted by the mean field model. The intermediate phase revealing a 50% increased $I_{(0,0,2-Q)}$ (figure 5.23) was assumed to be a basal plane helix.

A full parameter fit gave the simple basal plane helix ($\theta_{Ho} = \theta_{Er} \simeq 0$)for all $T > T_C = 35$ K, but upon constraining to a slowly varying ordered moment, the model responded with the *binary tilted helix* with opposite tilt directions $\theta_{Ho} = 27°$ and $\theta_{Er} = -43°$ respectively in order to accommodate the reduction of scattering above 45 K. Tilting the helix enables a reduction of the *c*-axis scattering, while the opposite tilt angles minimizes the in-plane effects by cancellation of the out-of-plane moments.

In general the investigation suffered from relatively high χ^2 with as little difference as from 12.8 for the best fit to 12.9 for other structures. As such it serves as a good example of the inadequacy of "excercice brut" collection and fitting of integrated peak intensities in magnetic structure analysis.

Magnetic x-ray diffraction experiments

Following up on the neutron scattering results the same sample was studied using resonance-enhanced magnetic *x-ray* diffraction at the beam line W1 at HASYLAB in Hamburg (Pengra *et al.* 1994).

In the technique of resonance-enhanced scattering the incident energy is tuned to an absorption edge, which causes a resonance-enhancement of the scattering from a magnetic structure (Hannon *et al.* 1988, Gibbs *et al.* 1988).

By tuning the incident energy to the L_{III} edge in either holmium or erbium the magnetic ordering of each element can be studied partially separated.

A priori it could be imagined that the two types of magnetic moments would order at different temperatures, but both Ho and Er were found to order at the same transition temperature T_N. With the knowledge of the exchange interaction this is also the only possible behaviour.

The x-ray data confirmed the existence of three phases, but were insufficient to supply evidence for the structures proposed from the neutron scattering experiment.

Also reported in the paper is an anomalous energy and polarization dependence in the resonant satellites. This combined with the quite complicated theory of resonance enhanced magnetic scattering made quantitative interpretations of the data difficult.

What is new in this treatment?

As described some work has already been done on the holmium–erbium alloys, but the present work include several new parts, which will be stressed here:

- Neutron scattering has been performed also on a $\mathrm{Ho_{90}Er_{10}}$ crystal.
- Not only the main magnetic satellites have been investigated. Long scans along $[1, 0, l]$ and $[0, 0, l]$ supply informations about the higher harmonics and hence important details of the structures.
- A *virtual-crystal mean-field* model has been constructed enabling calculations on the magnetic structures and excitations.

Chapter 2

The model

The alloys are interpreted through a *virtual-crystal* model based on the mean-field models for pure holmium (Jensen 1996a) and erbium (Cowley and Jensen 1992).

2.1 The localized $4f$ spin approximation

The magnetism of a solid is mainly determined by the electrons. A determination of the magnetic properties would therefore in principle require full knowledge of the electronic structure of the alloy as determined by the general Hamiltonian:

$$\mathcal{H} = \sum_i \frac{\boldsymbol{p}_i^2}{2m} + v_{\text{ext}}(\boldsymbol{r}_i) + \frac{1}{2}\sum_{ij} \frac{e^2}{|\boldsymbol{r}_i - \boldsymbol{r}_j|} + \mathcal{H}_{\text{exc}}. \tag{2.1}$$

This formidable task can however be simplified by the observation, that when combined into a solid, the rare earth atoms loose their 5d and 6s electrons to the delocalized Bloch states of the conduction band, whereas the $4f$ electrons stay well localized. As in the free atom the $4f$ electrons can be considered by *Hund's rules* giving rise to a magnetic moment J at each atom. The conduction band does not contribute directly to the magnetic properties. It is therefore possible to restrict the problem to the space spanned by the $2J+1$ eigenstates of J_z. This implies, that the Hamiltonian only depends on the $\boldsymbol{J}_i$ operators instead of the general $\boldsymbol{r}_i, \boldsymbol{p}_i, \sigma_i$.

Since he Hamiltonian is built as a functional of the $\boldsymbol{J}_i$ operators and some interactions involve $\boldsymbol{S_i}$ or $\boldsymbol{L_i}$, the *Wigner–Eckart* theorem will be used frequently.

2.2 Interactions

The *spin Hamiltonian* itself is a complicated problem, and whereas the deduction of the general Hamiltonian was straight forward, the spin Hamiltonian must

be constructed using more physical intuition regarding the kinds of interactions between the spins. The projection of the electron orbitals on to the $|J_z\rangle$ states should in principle be performed for the Hamiltonian too. This is however not possible, and the model Hamiltonian is therefore constructed by a combination of selected terms from the projection, and known spin interactions:

$$\mathcal{H} = \mathcal{H}_Z + \mathcal{H}_{\text{cf}} + \mathcal{H}_{\text{ex}} + \mathcal{H}_{\text{dipole}} + \mathcal{H}_{\text{multipole}}. \tag{2.2}$$

There are two main categories of operators in the Hamiltonian. One-ion operators which act on each ion at a time, and two-ion operators which operate on two ions at the same time. The one-ion operators represent the field that each of the ions feel. These fields lift the degeneracy of the ground state multiplet. The two-ion operators on the other hand represent the interaction between the ions and as such is responsible for the magnetic ordering. Each of the interactions in equation 2.2 will be presented in the following.

2.2.1 The Zeeman term, $\mathcal{H}_Z$

The perhaps simplest term in the spin Hamiltonian is the interaction with a static external magnetic field $\boldsymbol{H}$. Each electron spin interacts with the field through its dipole moment as $g_0\mu_B \boldsymbol{s}_i \cdot \boldsymbol{H}$, and in the *Russell–Saunders* coupling this adds up to $g_0\mu_B \boldsymbol{S} \cdot \boldsymbol{H}$. The field contribution to the orbital Hamiltonian is obtained by replacing $\boldsymbol{p}_i \to \boldsymbol{p}_i + \frac{e}{c}\boldsymbol{A}$, where the vector potential can be chosen to $\boldsymbol{A} = -\frac{1}{2}\boldsymbol{r} \times \boldsymbol{H}$. Then the kinetic energy becomes:

$$\frac{1}{2m}\sum_i (\boldsymbol{p}_i - \frac{e}{2c}\boldsymbol{r}_i \times \boldsymbol{H})^2 = \sum_i \frac{\boldsymbol{p}_i^2}{2m} + \mu_B \boldsymbol{L} \cdot \boldsymbol{H} + \frac{e^2H^2}{8mc^2}\sum_i r_{\perp i}^2, \tag{2.3}$$

where $\hbar\boldsymbol{L} = \sum_i \boldsymbol{r}_i \times \boldsymbol{p}_i$ is the orbital angular momentum. The last term is the Larmor diamagnetic susceptibility term, which even at high fields is orders of magnitudes smaller, than the second term. Combined with the spin interaction and using the *Wigner–Eckart* theorem within the considered subspace the latter can be written as the well known *Zeeman* term:

$$\mathcal{H}_Z = -g\mu_B \boldsymbol{J} \cdot \boldsymbol{H}, \tag{2.4}$$

corresponding to a magnetic dipole moment $g\mu_B \boldsymbol{J}$ in a magnetic field, where g is the *Landé factor* defined in equation 1.2.

2.2.2 Crystal field, $\mathcal{H}_{\text{cf}}$

The $4f$ electrons will be affected by the electrical field due to the charge distribution in the crystal $\rho(\boldsymbol{R})$. This crystal field which has the symmetry of the point group, can be expanded in spherical harmonics. If the surrounding charge density does not penetrate the localized $4f$ orbitals the crystal field will fulfill Laplace's equation, and the expansion becomes quite simple:

$$v_{\rm cf}(\boldsymbol{r}) = \int \frac{e\rho(\boldsymbol{R})}{|\boldsymbol{r}-\boldsymbol{R}|} d\boldsymbol{r} = \sum_{l\ m} A_m^l r^l Y_m^l(\boldsymbol{r}). \tag{2.5}$$

The crystal field Hamilton in real space is the sum over occupied electron states in the ion $\mathcal{H}_{\rm cf} = \sum_i v_{\rm cf}(\boldsymbol{r}_i)$. The basis vectors $|J_z\rangle$ of the ground state multiplet are linear combinations of Slater determinants of single electron states $|l'm_l'\rangle$. Hence the projected Hamiltonian will hold sums of terms like $\langle l'm_l'|r^l Y_m^l|l'm_l'\rangle = \langle r^l\rangle_{l'}\langle l'm_l'|Y_m^l|l'm_l'\rangle$. Where $\langle r^l\rangle_{l'} = \int_0^\infty |R_{l'}(r)|^2 r^{l+2} dr$ is the radial wave function average of r^l. Since $4f$ electrons have $l' = 3$, the matrix elements are only non vanishing for $l \leq 2l' = 6$. This can be expressed as the fact, that $4f$ electrons can only have multipole distributions less than 6.

Since we remain within the ground state multiplet specified by *Hund's rules*, the *Wigner–Eckart* theorem allows to express the matrix elements of $v_{\rm cf}(\boldsymbol{r})$ in terms of the J operators:

$$\mathcal{H}_{\rm cf}(\boldsymbol{J}) = \sum_{l\ m} A_l^m \langle r^l\rangle \alpha_l \sqrt{\frac{2l+1}{4\pi}} \tilde{O}_{lm}(\boldsymbol{J}), \tag{2.6}$$

where α_l are the Stevens factors and $\tilde{O}_{lm}(J)$ the *Racah operators* obtained by replacing (x, y, z) in the spherical harmonics by (J_x, J_y, J_z) and multiplying with $(4\pi/2l+1)^{1/2}$.

The parameters in $\mathcal{H}_{\rm cf}$ could in principle be derived from first principles. However, most electronic structure calculations are based on assumptions like the atomic sphere approximation (ASA) or methods treating the crystal symmetry as perturbations to the ASA. For this reason they are inadequate for precise calculations of the crystal field, which exactly contains the symmetry of the crystal. Therefore the parameters must be treated as experimentally determined. Once this is realized, the crystal field Hamiltonian can just as well be expressed in the computationally most convenient form, which is also the customary practice:

$$\mathcal{H}_{\rm cf}(i) = \sum_{l\ m} B_l^m O_l^m(\boldsymbol{J}_i). \tag{2.7}$$

B_l^m are called the crystal field parameters, and $O_l^m(\boldsymbol{J})$ are the *Stevens operators*. The f electrons can only have multipole distributions up to $l = 6$, but this still leaves a considerable number of parameters. Fortunately symmetry restricts the number of allowed parameters. For crystals with hexagonal point symmetry only four terms remain: B_2^0, B_4^0, B_6^0 and B_6^6. The corresponding operators are:

$$
\begin{aligned}
O_2^0 &= 3J_z^2 - J^2 \\
O_4^0 &= 35J_z^4 - (30J^2 - 25)J_z^2 + 3J^4 - 6J^2 \\
O_6^0 &= 231J_z^6 - (315J^2 - 735)J_z^4 + (105J^4 - 525J^2 + 294)J_z^2 \\
&\quad - 5J^6 + 40J^4 - 60J^2 \\
O_6^6 &= \frac{1}{2}(J_+^6 + J_-^6),
\end{aligned} \tag{2.8}
$$

where $J^2 = J(J+1)$ is the squared length of the angular momentum $\boldsymbol{J}$. The four crystal field parameters given in table 2.1 are determined from magnetization, elastic neutron scattering and spin wave experiments.

[meV]	B_2^0	B_4^0	B_6^0	B_6^6	B_6^6/B_6^0
Ho	0.024	0.0	$-0.95{\cdot}10^{-6}$	$9.4{\cdot}10^{-6}$	-9.89
Er	-0.027	$-0.3{\cdot}10^{-4}$	$1.3{\cdot}10^{-6}$	$-9.0{\cdot}10^{-6}$	-6.92
B(Ho)/B(Er)	-0.89	$-$	-0.73	-1.04	

Table 2.1: Crystal field parameters in Ho and Er.

The crystal field Hamiltonian is a one particle operator, that lifts the degeneracy of states in the ground state multiplet. The O_l^0 operators are seen to depend on J_z^2 only, and are therefore already diagonal (and symmetric in J_z). The effect on J_z can be illustrated by calculating the classical value of the crystal field energy as a function of J_z as seen in figure 2.1.

The eigenstates and corresponding eigenvalues of $\mathcal{H}_{\text{cf}}$ for Ho are shown in table 2.2. The ground state expectation value of $|J_z|$ is 3, which is also seen as the minimum for discrete values of J_z in figure 2.1.

E_n [meV]	$\|n\rangle$
0	$\frac{1}{\sqrt{2}}(\|3\rangle - \|-3\rangle)$
0.16	$\pm 0.08\|\pm 8\rangle \mp 0.73\|\pm 2\rangle \pm 0.68\|\mp 4\rangle$
0.54	$\pm 0.23\|\pm 7\rangle \mp 0.76\|\pm 1\rangle \pm 0.61\|\mp 5\rangle$
0.76	$-0.78\|0\rangle + 0.44(\|6\rangle + \|-6\rangle)$
4.24	$\frac{1}{\sqrt{2}}(\|6\rangle - \|-6\rangle)$
4.54	$-0.84\|\pm 7\rangle + 0.16\|\pm 1\rangle + 0.51\|\mp 5\rangle$
5.00	$\pm 0.94\|\pm 8\rangle \mp 0.17\|\pm 2\rangle \pm 0.30\|\mp 4\rangle$
6.25	$\frac{1}{\sqrt{2}}(\|3\rangle + \|-3\rangle)$
6.32	$\mp 0.33\|\pm 8\rangle \mp 0.67\|\pm 2\rangle \mp 0.67\|\mp 4\rangle$
6.42	$\mp 0.49\|\pm 7\rangle \mp 0.63\|\pm 1\rangle \mp 0.60\|\mp 5\rangle$
6.46	$0.62\|0\rangle + 0.55(\|6\rangle + \|-6\rangle)$

Table 2.2: Eigenvectors and values for $\mathcal{H}_{\text{cf}}$ in Ho

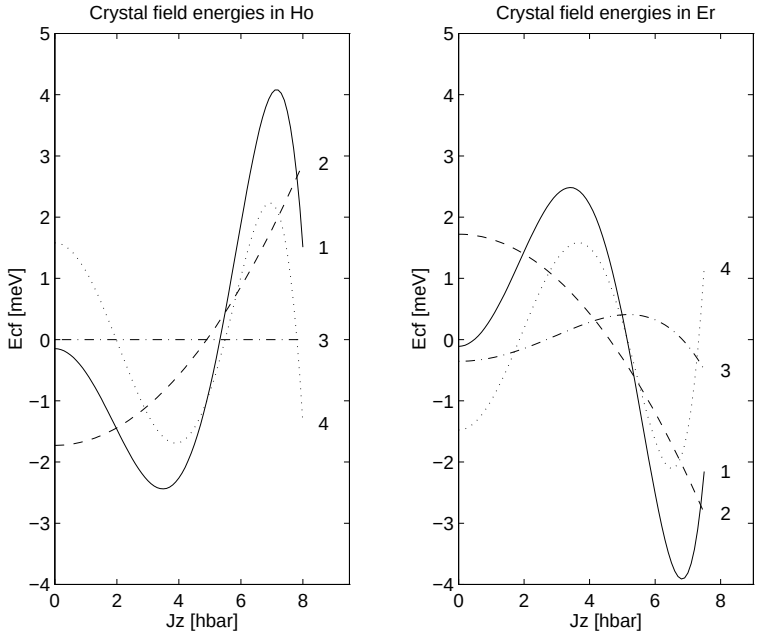

Figure 2.1: Classical crystal field energies in Ho and Er: 1) $\sum B_l^0 O_l^0$ 2) $B_2^0 O_2^0$ 3) $B_4^0 O_4^0$ 4) $B_6^0 O_6^0$

The effect of B_6^6 can again be understood classically by assuming:

$$(J_x, J_y) = J_0(\cos\phi, \sin\phi).$$

Then the operators $J_\pm$ becomes:

$$J_\pm = J_0(\cos\phi \pm i\sin\phi) = J_0 e^{\pm i\phi},$$

which leads to:

$$O_6^6(\boldsymbol{J}) = \frac{1}{2}(J_+^6 + J_-^6) = \frac{1}{2}J_0^6(e^{i6\phi} + e^{-i6\phi}) = J_0^6\cos 6\phi. \tag{2.9}$$

This function has 6 maxima at $n\pi/3$ and 6 minima at $(1+2n)\pi/6$. Depending on the sign of B_6^6 this favours either the a- or the b-axis and the corresponding axes. The maxima and the minima, called *hard* and *easy axes* respectively, define 6 regions (*hexants*) separated by the hard axes. This hexagonal term manifests itself in the eigenvectors, by the fact, that each eigenvector is a superposition of $|J_z\rangle$'s, with $J_z - J_z' = 6$. In a system, where the exchange interaction and the B_l^0's produces a helix structure, B_6^6 will modify the constant shift angle between succeeding planes by pushing the spins from the hard axis towards the

easy axis. Two spins within the same hexant will thus *bunch* as a pair around the easy axis.

The energy difference $2B_6^6 J_0^6 \simeq 2 \cdot 8^6 \cdot 9 \cdot 10^{-6}$ meV $= 4.7$ meV $= 55$ K comprises a measure of the barrier the system has to overcome in order to move a spin over a hard axis.

First principle calculations of the crystal field parameters meet with little success, but two relative results can be obtained. By considering a hexagonal lattice of point charges the ratio B_6^6/B_6^0 can be found to be $-77/8$ for an ideal ratio of $c/a = \sqrt{8/3}$.

Another interesting feature of the holmium–erbium alloy is that the Stevens factors α_l are equal in magnitude but have opposite signs for the two elements. This can be seen from two symmetry properties regarding the matrix elements $\langle lm_l|Y_{m'}^{l'}|lm_l\rangle = f(m_l)$:

$$\left.\begin{array}{l} f(m_l) = f(-m_l) \\ \sum_{m_l=-l}^{l} f(m_l) = 0 \end{array}\right\} \Longrightarrow \sum_{m_l=-l}^{-1} f(m_l) = -\sum_{m_l=-l}^{0} f(m_l). \tag{2.10}$$

From this it is seen, that $\alpha_l^{\mathrm{Er}} = -\alpha_l^{\mathrm{Ho}}$ which means, that if the mean radius $\langle r^l\rangle$ and the potential parameters A_m^l are the same, the crystal fields are of the same strength but with opposite sign.

Hence in the pure elements the bunching takes place along different axes with a phase shift of $\pi/6$. In the alloy a competition between the two directions takes place. For instance, in $\mathrm{Ho_{90}Er_{10}}$ the Er spins are dictated by the Ho spins, but the spin separation angle in a pair is larger than 30°, so that two spins in neighbouring pairs actually are closer together than the pair.

2.2.3 Dipole coupling, $\mathcal{H}_{\mathrm{dipole}}$

The two-ion interactions are generally of the form $\sum_{ij} I(\boldsymbol{J}_i, \boldsymbol{J}_j)$. If the coupling only depends on the dipole moment, the general two dipole coupling is:

$$\mathcal{H}_{dd} = -\frac{1}{2}\sum_{ij\alpha\beta} J_{i\alpha}\mathcal{J}_{\alpha\beta}(ij)J_{j\beta}. \tag{2.11}$$

One interaction of this kind is the classical dipole coupling, which is given by:

$$\mathcal{J}_{\alpha\beta}(ij) = g^2\mu_B^2 \frac{3(R_{i\alpha} - R_{j\alpha})(R_{i\beta} - R_{j\beta}) - |\boldsymbol{R}_i - \boldsymbol{R}_j|^2}{|\boldsymbol{R}_i - \boldsymbol{R}_j|^5}. \tag{2.12}$$

The coupling constants can be calculated for a hexagonal lattice with an ideal c/a ratio or summed numerically for any given c/a ratio (Jensen and Mackintosh 1991). Since holmium and erbium have very similar c/a ratios both of them have a dipole coupling as:

$$\mathcal{J}_D(q) = -4\pi(g\mu_B)^2 N/V(0.919 + 0.0816\cos(qc/2) - 0.0006\cos(qc)), \quad (2.13)$$

with the one important exception that the dipole contribution vanishes at zero wave vector $\mathcal{J}_D(0) = 0$. This discontinuity which can actually be observed by spin wave measurements (Larsen *et al.* 1987) is responsible for the preference of the *cone* phase rather than the *tilted helix* (Sherrington 1972) which will be discussed later.

The coupling strength $\mathcal{J}_{dd} = 4\pi(g\mu_B)^2 N/V$ is evaluated for Er and Ho using $V/N = \sqrt{3}a^2c/4$ and $\mu_B = 0.05368$ meVÅ^3. In holmium the polarization of the conduction electron gas has been estimated to give a correction of about 3%. The resulting coupling strengths are:

$\mathcal{J}_{dd}^{\mathrm{Ho}}$	0.0349 meV
$\mathcal{J}_{dd}^{\mathrm{Er}}$	0.0316 meV

Table 2.3: Classical dipole coupling parameters

2.2.4 Indirect exchange coupling, $\mathcal{H}_{\mathrm{ex}}$

Another type of interaction, which turns out to be dominant, is the indirect exchange interaction. This deals with the fact that two different spins individually coupled to the intermediate conduction electron gas influence each other through the latter. This indirect interaction can be calculated by first finding the response of the conduction electrons to moment $\boldsymbol{S}_j$ and then the effect of that conduction electron moment on the $4f$ moment $\boldsymbol{S}_i$.

The coupling of a $4f$ moment to the electron gas, with spin density $\boldsymbol{\sigma}(\boldsymbol{r})$ is of the Heisenberg form:

$$\mathcal{H} = -\frac{2}{N}\int I(\boldsymbol{r} - \boldsymbol{R}_i)\boldsymbol{S}_i \cdot \boldsymbol{\sigma}(\boldsymbol{r})d\boldsymbol{r} = -\int \boldsymbol{H}_i(\boldsymbol{r}) \cdot \boldsymbol{\mu}(\boldsymbol{r})dr. \quad (2.14)$$

$I(r)$ is the exchange integral of the electron charge clouds, and the last equality is defined by viewing the effect on the conduction electron moment density $\boldsymbol{\mu}(\boldsymbol{r}) = \mu_B\boldsymbol{\sigma}(\boldsymbol{r})$ as arising from an inhomogeneous magnetic field

$$\boldsymbol{H}_i(\boldsymbol{r}) = I(\boldsymbol{r} - \boldsymbol{R}_i)\boldsymbol{S}_i/N\mu_B. \quad (2.15)$$

The response at position $\boldsymbol{r}$ to a spin at position $\boldsymbol{R}_j$ is thus:

$$\boldsymbol{\mu}_j(\boldsymbol{r}) = \frac{1}{V}\int \boldsymbol{\chi}(\boldsymbol{r} - \boldsymbol{r}')\boldsymbol{H}_j(\boldsymbol{r}')d\boldsymbol{r}', \quad (2.16)$$

where the matrix $\boldsymbol{\chi}$ is the 3×3 dimensional susceptibility for the conduction electrons. Thus by using equation 2.14 twice the coupling is found to be:

$$\mathcal{H} = -\frac{1}{V} \iint H_i(\boldsymbol{r}) \boldsymbol{\chi}(\boldsymbol{r} - \boldsymbol{r}') \boldsymbol{H}_j(\boldsymbol{r}') d\boldsymbol{r} d\boldsymbol{r}'. \tag{2.17}$$

Summing over i and j, using $\boldsymbol{S} = (g-1)\boldsymbol{J}$ within the multiplet and exploiting the decoupling power of Fourier transformation the indirect exchange interaction may be written as:

$$\mathcal{H}_{\text{ex}} = -\frac{1}{2} \sum_{ij} \boldsymbol{J}_i \boldsymbol{\mathcal{J}}(ij) \boldsymbol{J}_j, \tag{2.18}$$

where the 3×3 dimensional matrix $\boldsymbol{\mathcal{J}}$ is given by:

$$\begin{aligned} \boldsymbol{\mathcal{J}}(ij) &= \frac{1}{N} \sum_{\boldsymbol{q}} e^{i\boldsymbol{q}\cdot(\boldsymbol{R}_i - \boldsymbol{R}_j)} \boldsymbol{\mathcal{J}}(\boldsymbol{q}) \\ \boldsymbol{\mathcal{J}}(\boldsymbol{q}) &= \frac{(g-1)^2 V}{N^2 \mu_B^2} |I(\boldsymbol{q})|^2 \boldsymbol{\chi}(\boldsymbol{q}), \end{aligned} \tag{2.19}$$

This includes the self energy of the ith moment, which is just a constant term in the total energy. This can be avoided by subtracting $\sum_{\boldsymbol{q}'} \boldsymbol{\mathcal{J}}(\boldsymbol{q}')/N$ from $\boldsymbol{\mathcal{J}}(\boldsymbol{q})$.

If spin orbit coupling of the conduction electrons and magnetization effects are neglected, the susceptibility becomes scalar, and hence $\boldsymbol{J}_i \boldsymbol{\mathcal{J}}(ij) \boldsymbol{J}_j = \mathcal{J}(ij) \boldsymbol{J}_i \cdot \boldsymbol{J}_j$. In this case the indirect exchange coupling is isotropic.

The susceptibility can be derived as:

$$\chi(\boldsymbol{q}) = \frac{-2\mu_B^2}{V} \sum_{nn'\boldsymbol{k}} \frac{f_{n,\boldsymbol{k}+\boldsymbol{q}} - f_{n',\boldsymbol{k}}}{\varepsilon_n(\boldsymbol{k}+\boldsymbol{q}) - \varepsilon_{n'}(\boldsymbol{k})}, \tag{2.20}$$

and straight forwardly deduced from energy band calculations. The numerator requires, that exactly one of the wave vectors $\boldsymbol{k}$ and $\boldsymbol{k} - \boldsymbol{q}$ lie within the *Fermi surface*, whereas the denominator favours small energy differences. Since they are on different sides of the Fermi surface, both energies must be very close to the *Fermi energy*. The $\boldsymbol{k}$ summation may therefore as a crude approximation be restricted to the Fermi surface.

For a given $\boldsymbol{q}$ the denominator in the $\boldsymbol{k}$ summation will cause contributions whenever $\boldsymbol{k} + \boldsymbol{q}$ coincides with the Fermi surface. The summation may thus be seen as the area overlap of two Fermi surfaces separated by $\boldsymbol{q}$. Parallel regions of the Fermi surface will thus cause maxima in the susceptibility for $\boldsymbol{q}$ equal the translation vector $\boldsymbol{Q}$ between the parallel regions as illustrated in figure 1.6.

The effect of this maximum for nonzero $\boldsymbol{Q}$ can be illustrated by Fourier transforming the Hamiltonian:

$$\mathcal{H}_{ex} = -\frac{N}{2}\sum_{\boldsymbol{q}} \mathcal{J}(\boldsymbol{q}) J(\boldsymbol{q}) \cdot J(-\boldsymbol{q}) \quad , \quad J(\boldsymbol{q}) = \frac{1}{N}\sum_{i} \boldsymbol{J}_i e^{-i\boldsymbol{q}\cdot\boldsymbol{R}_i}. \tag{2.21}$$

Thus the exchange interaction favours structures with nonzero Fourier components for $\boldsymbol{q} = \boldsymbol{Q}$. This is the reason for all the interesting periodic structures observed in the rare earths. Figure 1.7 reflects a width of the toes around 0.2, which does not agree perfectly with the observed starting periodicity $Q(T_N) \simeq 0.28$. The reason for this discrepancy is to be found in the other $\boldsymbol{q}$ dependent component in $\mathcal{J}(\boldsymbol{q})$.

The exchange integral $I(\boldsymbol{q})$ on the contrary is very difficult to determine, since it requires full knowledge of the electron orbitals and the screening effects. First principles calculations have been performed on for instance Gd($4f^7$) (Lindgård *et al.* 1975). With the half filled $4f$ shell the largest $S = 3\frac{1}{2}$ and lowest $L = 0$ in the the rare earth series is obtained from *Hund's rules*. The maximum S provides a large isotropic Heisenberg exchange interaction, whereas the lack of orbital momenta ensures that the anisotropic crystal fields are orders of magnitude smaller.

By using energy-band structure and wave functions obtained from nonrelativistic augmented-plane-wave (APW) calculations the exchange integral was calculated from the formal expression:

$$I_{nn'}(\boldsymbol{k},\boldsymbol{k}') = \frac{1}{2l+1}\sum_{m_l=-3}^{3} \iint \frac{d^3\boldsymbol{r} d^3\boldsymbol{r}'}{|\boldsymbol{r}-\boldsymbol{r}'|} \psi^*_{\boldsymbol{k},n}(\boldsymbol{r}) \phi^*_{4f,m_l}(\boldsymbol{r}') \phi_{4f,m_l}(\boldsymbol{r}) \psi_{\boldsymbol{k}',n'}(\boldsymbol{r}'). \tag{2.22}$$

In comparison with inelastic neutron scattering measurements of the magnon dispersion relation, the overall $\boldsymbol{q}$ dependency is obtained, but the absolute values differ by a factor of 4. Furthermore the precise form and position of the maximum in $\mathcal{J}(\boldsymbol{q})$ is not found. However, the calculations revealed that the maximum is not solely determined by the nesting of parallel regions of the Fermi surface.

The actual determination of the exchange coupling is therefore not possible from first principles. Instead, the fact that $\mathcal{J}(\boldsymbol{q}) - \mathcal{J}(\boldsymbol{0})$ is very closely related to the spin wave dispersion relation, is used to determine the coupling parameters.

As seen in table 2.4 the indirect exchange interaction is extended to the sixth nearest neighbour. For Ho the parameters have been determined for several temperatures between which linear interpolation is used, except between the two lowest temperatures, where quadratic interpolation is used. In contrast only one set of parameters is known for Er, which of course presents a limitation in the success of exact description of the temperature dependencies of the alloys.

The temperature dependence of $\mathcal{J}(\boldsymbol{q})$ is a consequence of a self consistent modification of the electronic structure due to the magnetic ordering. The formation of periodic magnetic structures polarizes the conduction electrons and

T [K]	$\mathcal{J}_0$	$\mathcal{J}_1$	$\mathcal{J}_2$	$\mathcal{J}_3$	$\mathcal{J}_4$	$\mathcal{J}_5$	$\mathcal{J}_6$
Ho 0	0.300	0.09	0.006	-0.0140	-0.006	-0.002	0.0
50	0.290	0.10	0.010	-0.0290	-0.005	0.008	-0.004
72	0.267	0.11	0.010	-0.0377	-0.001	0.004	-0.003
96	0.245	0.11	0.010	-0.0463	0.006	0.0	0.0
125	0.210	0.11	0.010	-0.0640	0.006	0.0	0.0
Er 4.5	0.165	0.073	-0.025	-0.006	-0.018	-0.003	0.0

Table 2.4: The inter-planar exchange coupling parameters in meV

causes gaps in the energy bands. This influences the electronic susceptibility and as a result the maximum value $\mathcal{J}(\boldsymbol{Q}_{\mathcal{J}})$ and position $\boldsymbol{Q}_{\mathcal{J}}$ both decrease as the temperature decreases. This effect has been investigated with reasonable agreement by Elliot and Wedgwood (1964) assuming a spherical *Fermi surface*. The energy gaps were treated in a super-zone boundary notation giving a reasonable description on the temperature dependence in Ho, Er and Tm. Also the low temperature composition dependency in Y-Tb alloys was satisfactory explained in terms of an averaged effective size of the magnetic moment.

2.2.5 Multipolar coupling, $\mathcal{H}_{\text{multipole}}$

The indirect exchange and the dipole couplings covered so far are only two special and simple cases of possible two-ion interactions. A general form of a two-ion interaction is:

$$\mathcal{H}_{\text{two-ion}} = -\tfrac{1}{2}\sum_{ij}\mathcal{K}_{ll'}^{mm'}(ij)[O_l^m(\boldsymbol{J}_i)O_{l'}^{m'}(\boldsymbol{J}_j) + (-1)^{m+m'}O_l^{-m}(\boldsymbol{J}_i)O_{l'}^{-m'}(\boldsymbol{J}_j)]. \tag{2.23}$$

The possible terms are restricted by symmetry, but still comprise a large number of parameters, which can only be decoupled and determined by physical intuition. Instead of treating the expression as an expansion with the $\mathcal{K}$'s either to be determined from the first principles projection onto the ground state multiplet or as parameters to be fitted from experiment, each possible cause of interaction should be considered in order to restrict the number of parameters (Jensen 1974).

Some of the symmetry restrictions for an *hcp* lattice are that $l + l'$ should be even and $(m + m')/3 = p$ must be an integer. The exchange interaction and the axial crystal field are $p = 0$ terms, whereas the hexagonal crystal field corresponds to $p = 2$. But even the $p = 0$ interactions are not exhausted by the Hamiltonian so far, and other of these may be necessary to obtain a good model.

For instance, spin wave measurements on Er revealed other two-ion anisotropy effects other than the classical dipole coupling were required to fit the

results using MF-RPA calculations (Cowley and Jensen 1992). The spin wave dispersion relation at 4.5 K could not be described by the isotropic exchange coupling alone. Among the different choices of anisotropic two-ion interactions the one accounting most readily for the spin wave dispersions was:

$$\mathcal{H} = -\frac{1}{2}\sum_{ij} \mathcal{K}_{33}^{2-2}(ij)[O_3^2(\boldsymbol{J}_i)O_3^2(\boldsymbol{J}_j) + O_3^{-2}(\boldsymbol{J}_i)O_3^{-2}(\boldsymbol{J}_j)]. \tag{2.24}$$

The coupling parameters were found to be:

n	0	1	2	3	4	5
$\mathcal{K}_{33}^{2-2}$	0	-8	-7	-10	0	-3

Table 2.5: Inter-planar anisotropic coupling parameters in Er [meV/10^6]

2.2.6 Trigonal coupling, $\mathcal{H}_3$

Furthermore detailed neutron scattering on the higher harmonics of the *cycloidal* phase in Er revealed, that another anisotropic interaction was needed. The Hamiltonian so far does not reflect the different orientations of the two hexagonal sub-lattices. A distinction between the two sub lattices will effectively double the unit cell in real space and hence introduce twice as many magnetic peaks along c^* in reciprocal space. The detailed neutron scattering experiments showed exactly such peaks. Therefore a coupling with trigonal symmetry was introduced (Jensen 1996b). Such a distinction between the two lattices correspond to p odd, and the lowest order terms must then have $m + m' = 3$ and $l + l' = 4$. There exist three possibilities $\mathcal{K}_{22}^{21}$, $\mathcal{K}_{31}^{30}$ and $\mathcal{K}_{31}^{21}$. The trigonal interaction is chosen as the latter and becomes:

$$\mathcal{H}_3 = \sum_{ij} \mathcal{K}_{31}^{21}(ij)[O_3^2(\boldsymbol{J}_i)J_{yj} + O_3^{-2}(\boldsymbol{J}_i)J_{xj}]. \tag{2.25}$$

Recently a similar examination has been performed for holmium (Simpson *et al.* 1995). Though roughly an order of magnitude weaker, evidence of the trigonal coupling was found. The numerical determination of the coupling parameters provide a nice example of the difficulties due to the non-orthogonality of the different interactions. The same data have been reinvestigated paying attention to the effect of the trigonal interaction on various commensurate structures by Jensen (1996a). His values for the trigonal interaction in holmium and erbium given in table 2.6 are roughly a factor of 5 weaker.

Although very faint the present measurements on both alloys show evidence for the trigonal coupling. The distortion of the structures by the trigonal interaction is most pronounced in the c-component of the moments, and hence is

n	0	1.2	3.	
$\mathcal{K}_{31}^{21}$(Ho)	0	0.07	0.04	0.02
$\mathcal{K}_{31}^{21}$(Er)	0	0.6	-0.25	-0.05

Table 2.6: Inter-planar trigonal coupling parameters [meV/10^3]

to be found in the $[1,0,l]$ scans. Figure 2.2 shows the $[1,0,l]$ scan at 10 K on $Ho_{90}Er_{10}$ fitted with a 7/36 structure with and without the trigonal interaction included in the Hamiltonian. It is clearly seen, that the peak at $l = 21/36$ and the bump at $l = 15/36$ are only present in the calculations when the trigonal coupling is introduced.

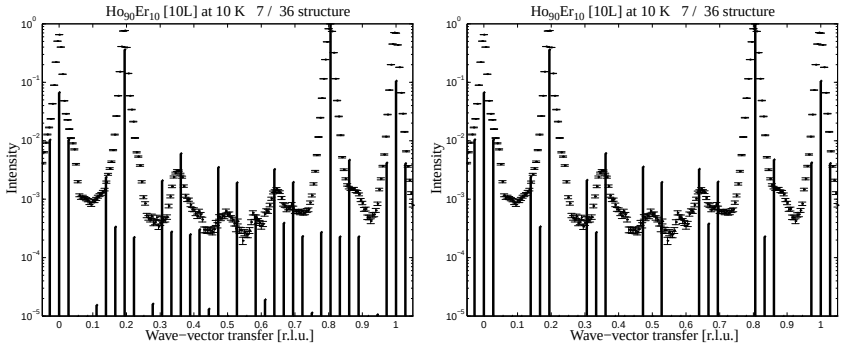

Figure 2.2: $[1,0,l]$ scan from $Ho_{90}Er_{10}$ at 10 K fitted with 7/36 structure with and without the trigonal interaction.

The two structures of figure 2.2 are shown in figure 2.3. It is seen how the trigonal interaction induces a 15/36 c-axis modulation in addition to the 12/36. The c-axis modulation mainly affects the $[1,0,l]$ scattering.

2.3 Mean-field approximation

The spin Hamiltonian as discussed so far is still a coupled many-particle operator. Therefore the mean-field (MF) approximation is introduced by writing the angular momentum operator as the thermal expectation value and the fluctuation $\boldsymbol{J} = \langle \boldsymbol{J} \rangle + (\boldsymbol{J} - \langle \boldsymbol{J} \rangle)$:

$$\boldsymbol{J}_i \boldsymbol{J}_j = \underbrace{\boldsymbol{J}_i \langle \boldsymbol{J}_j \rangle + \langle \boldsymbol{J}_i \rangle \boldsymbol{J}_j}_{\text{1-ion operators}} - \underbrace{\langle \boldsymbol{J}_i \rangle \langle \boldsymbol{J}_j \rangle}_{\text{constant}} + \underbrace{(\boldsymbol{J}_i - \langle \boldsymbol{J}_i \rangle)(\boldsymbol{J}_j - \langle \boldsymbol{J}_j \rangle)}_{\text{2-ion fluctuations}}. \tag{2.26}$$

Neglecting the 2-ion fluctuations, the exchange Hamiltonian for each moment can be written in terms of a mean field $h_i = \sum_j \mathcal{J}(ij) \langle \boldsymbol{J}_j \rangle$:

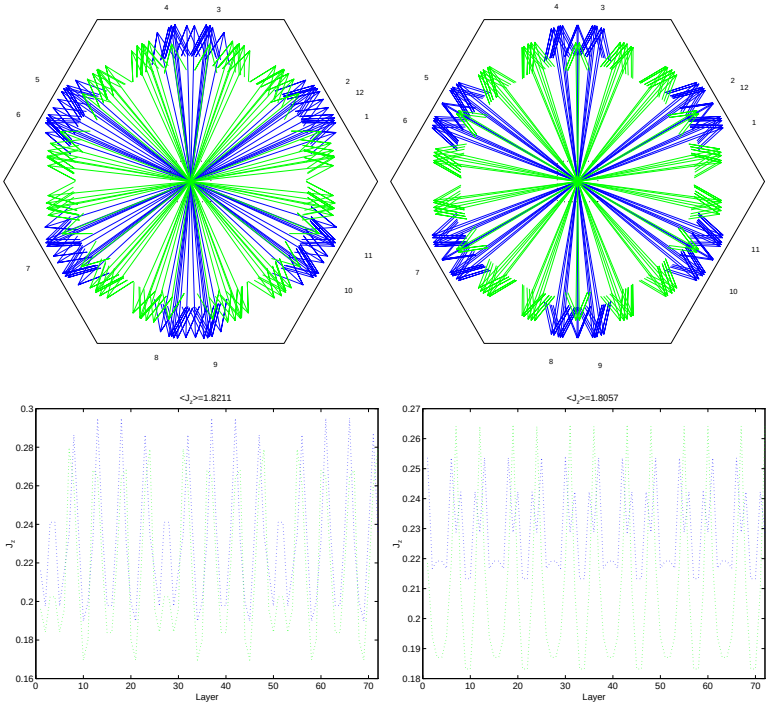

Figure 2.3: 7/36 structure with and without trigonal coupling. Ho moments are blue, Er moments are green.

$$\mathcal{H}_{\text{ex}} = -\frac{1}{2}\sum_{ij} \boldsymbol{J}_i \boldsymbol{\mathcal{J}}(ij) \boldsymbol{J}_j \simeq -\sum_i (\boldsymbol{J}_i - \frac{1}{2}\langle \boldsymbol{J}_i \rangle)\boldsymbol{h}_i^{\text{MF}}. \tag{2.27}$$

This decoupled Hamiltonian can be solved for each ion one by one. However, the mean field is dependent on the solution, and the calculation must therefore be iterated to obtained self consistency.

Other two-ion operators will have the form $O(\boldsymbol{J}_i)O'(\boldsymbol{J}_j)$ and a similar mean-field approximation can be made by considering $O(\boldsymbol{J}) = \langle O(\boldsymbol{J})\rangle + (O(\boldsymbol{J}) - \langle O(\boldsymbol{J})\rangle$:

$$O(\boldsymbol{J})O'(\boldsymbol{J}') \simeq (O(\boldsymbol{J}) - \frac{1}{2}\langle O(\boldsymbol{J})\rangle)\langle O'(\boldsymbol{J}')\rangle + (O'(\boldsymbol{J}') - \frac{1}{2}\langle O'(\boldsymbol{J}')\rangle)\langle O(\boldsymbol{J})\rangle. \tag{2.28}$$

For the trigonal coupling, the resulting mean-field approximated Hamiltonian becomes:

$$\begin{aligned}\mathcal{H}_3(i \in p\text{'th plane}) = (-1)^p \sum_{n\leq 1} \mathcal{K}_{31}^{21}(n) \\ \times \Big[\{O_3^2(i) - \frac{1}{2}\langle O_3^2(i)\rangle\}\langle J_y(p+n) - J_y(p-n)\rangle \\ + \{O_3^{-2}(i) - \frac{1}{2}\langle O_3^{-2}(i)\rangle\}\langle J_x(p+n) - J_x(p-n)\rangle \\ - (-1)^n\{J_y(i) - \frac{1}{2}\langle J_y(i)\rangle\}\langle O_3^2(p+n) - O_3^2(p-n)\rangle \\ - (-1)^n\{J_x(i) - \frac{1}{2}\langle J_x(i)\rangle\}\langle O_3^{-2}(p+n) - O_3^{-2}(p-n)\rangle \Big].\end{aligned} \tag{2.29}$$

The alternating sign can be written as $(-1)^p = \sum_{\boldsymbol{\tau}} e^{i\boldsymbol{\tau}\cdot\boldsymbol{R}_p}$. From this the trigonal coupling is seen to produce harmonic modulations located around $(0, 0, l)$ points with both even and odd l.

2.4 Analytical approaches to the Hamiltonian

Even the mean-field approximated Hamiltonian comprises a complexity, which cannot be solved analytically. But the iteratively converged self consistent solutions can be hard to interpret in terms of the initial interaction parameters. It is therefore useful to consider approximative and perturbative approaches in certain limits.

2.4.1 The static susceptibility χ

The mean field concept can straight forwardly be used to derive the classical magnetic susceptibility defined by $M = \chi H$ or $\chi = -\partial^2 F/\partial H^2$ in the presence of a magnetic field H. Neglecting the crystal field anisotropy and assuming the effective field to be small the *magnetization* becomes:

$$\begin{aligned} M &= \frac{g^2\mu_B^2 J(J+1)}{3k_B T}\frac{N}{V}(H + H_{\mathrm{MF}}) \\ H_{\mathrm{MF}} &= \frac{1}{g^2\mu_B^2}\frac{V}{N}\sum_j \mathcal{J}(ij)M = \frac{\mathcal{J}(\mathbf{0})}{g^2\mu_B^2}\frac{V}{N}M. \end{aligned} \tag{2.30}$$

The expression is thus only valid above the spontaneous ordering temperature T_N. Within these assumptions the static susceptibility follows the Curie–Weiss law:

$$\chi_{\mathrm{MF}} = \frac{g^2\mu_B^2 J(J+1)}{3k_B T}\frac{N}{V}\left(1 - \frac{\mathcal{J}(\mathbf{0})J(J+1)}{3k_B T}\right)^{-1} \equiv \frac{C}{T-\theta}. \tag{2.31}$$

where $\theta = \frac{\mathcal{J}(\mathbf{0})J(J+1)}{3k_B}$ is the Curie temperature for magnetic ordering within the model. Since $\mathcal{J}$ scales with $(g-1)^2$, the ordering temperatures should be expected to scale with the *de Gennes factor* $(g-1)^2J(J+1)$. For Ho and Er the de-scaled ordering temperatures are seen in table 2.7:

	$(g-1)^2J(J+1)$	T_N	$T_N/(g-1)^2J(J+1)$
Ho	15/4	133 K	35.5 K
Er	21/10	85 K	40.5 K

Table 2.7: Observed and de-scaled ordering temperatures in Ho and Er.

Although the agreement is not perfect the scaling concept generally holds throughout the entire rare earth series.

The classical susceptibility can be generalized from the spin Hamiltonian through the *Zeeman* term $\mathcal{H}_Z = -\sum_i \boldsymbol{\mu}_i \cdot \boldsymbol{H}_i \equiv -\sum_i \boldsymbol{J}_i \cdot \boldsymbol{h}_i$. For convenience the non local static susceptibility is defined through the last equation:

$$\chi_{\alpha\beta}(ij) = -\frac{\partial^2 F}{\partial h_{i\alpha}\partial h_{j\beta}}. \tag{2.32}$$

In terms of the Fourier transforms, the defining equation can be brought to a form similar to the classical macroscopic equation:

$$\delta\langle \boldsymbol{J}(\boldsymbol{q})\rangle = \boldsymbol{\chi}(\boldsymbol{q})\delta\boldsymbol{h}(\boldsymbol{q}). \tag{2.33}$$

2.4.2 High temperature expansion

The high temperature expansion $\exp(-\beta\mathcal{H}) \simeq 1-\beta\mathcal{H}+\frac{1}{2}\beta^2\mathcal{H}^2+\cdots$ can be used to approximate the inverse of the $\boldsymbol{q}$-dependent susceptibility:

$$\chi^{-1}_{\alpha\alpha}(\boldsymbol{q}) = \frac{3k_BT}{J(J+1)} + (3\delta_{\alpha\varsigma}-1)\frac{6(J-\frac{1}{2})(J+\frac{3}{2})}{5J(J+1)}B_2^0 - \mathcal{J}(\boldsymbol{q}) + \mathcal{O}(T^{-1}). \tag{2.34}$$

From which it is seen, that the *crystal field* parameter B_2^0 can be derived from magnetization measurements as the difference between $\chi_{\parallel}^{-1}(\mathbf{0})$ and $\chi_{\perp}^{-1}(\mathbf{0})$ with respect to the c-axis. Equation 2.34 can be derived without the MF approximation, which demonstrates, that the MF approximation is valid for high temperatures. The fluctuations are not necessarily small at high temperatures, but they are sufficiently uncorrelated to ensure the validity of the MF approximation.

Neglecting the crystal field term the previous Curie–Weiss behaviour is obtained with $\mathcal{J}(\boldsymbol{q})$ instead of $\mathcal{J}(\mathbf{0})$. Spontaneous ordering will occur for the maximum $\mathcal{J}(\boldsymbol{Q})$ at which $\chi = \frac{C}{T-T_N}$ with $T_N \simeq \frac{\mathcal{J}(\boldsymbol{Q})J(J+1)}{3k_B}$. Hence the exchange parameters can be chosen to fit the right ordering temperature.

The lowest order crystal field correction is different for basal plane ξ, η and c-axis ζ ordering:

$$T_{N,\alpha} = \frac{\mathcal{J}(\boldsymbol{Q})J(J+1)}{3k_B}\left[1 - \frac{2(3\delta_{\alpha\zeta}-1)}{5}(J-\frac{1}{2})(J+\frac{3}{2})B_2^0/T_N\right]. \quad (2.35)$$

2.4.3 Landau expansion

Just below the ordering temperature T_N the small magnitudes of the ordered moments $\langle \boldsymbol{J}_i \rangle$ can be used as order parameters, and the free energy may be expanded in powers of them. Due to time reversal symmetry the effective exchange field term is the only odd component in the Landau expansion:

$$F \simeq F_0 - \frac{1}{2}\sum_{ij}\mathcal{J}(ij)\langle \boldsymbol{J}_i\rangle \cdot \langle \boldsymbol{J}_j\rangle + \sum_i \left\{ \sum_\alpha A_\alpha \langle J_{i\alpha}\rangle^2 + \sum_{\alpha\beta} B_{\alpha\beta}\langle J_{i\alpha}\rangle^2\langle J_{i\beta}\rangle^2 + \cdots \right\}. \quad (2.36)$$

Assuming simple sinusoidal ordering $\langle \boldsymbol{J}_{i\alpha}\rangle = J\sigma_\alpha \cos(\boldsymbol{q}\cdot\boldsymbol{R}_i + \phi_\alpha)$, where the order parameters σ run from 0 in the not ordered phase to 1 in the totally ordered phase, the Landau free energy can be written as:

$$\frac{F-F_0}{N} = \frac{1}{4}J^2\sum_\alpha(2A_\alpha - \mathcal{J}(\boldsymbol{q}))\sigma_\alpha^2 + \frac{1}{8}J^4\sum_{\alpha\beta}B_{\alpha\beta}(2+\cos 2(\phi_\alpha-\phi_\beta))\sigma_\alpha^2\sigma_\beta^2, \quad (2.37)$$

if $\boldsymbol{q}$ is not commensurate with the lattice. The coefficients are found to be:

$$2A_\alpha - \mathcal{J}(\boldsymbol{q}) = \chi^{-1}_{\alpha\alpha}(\boldsymbol{q})\big|_{\sigma=0}$$
$$B_{\alpha\beta} = B \simeq \frac{9}{20}\frac{J^2+J-\frac{1}{2}}{J^3(J+1)^3}k_BT. \quad (2.38)$$

In Landau theory the ordering is determined by the development of the parabolic second order term and the positive fourth order term. As long as the second order coefficient is positive the minimum is obtained for $\sigma = 0$, but below the temperature $T_{N,\alpha}$ the parabola curves downwards, and the free energy obtains two minima $\pm\sigma$ for nonzero ordering parameters.

Depending on the sign of B_2^0 two different types of order appear. If $B_2^0 > 0$ as in Ho, it is the basal plane components of the susceptibility that diverges first, and hence the moments order transversely at the temperature:

$$T_N = \frac{\mathcal{J}(\boldsymbol{Q})J(J+1)}{3k_B}\left[1 + \frac{2}{5}(J-\frac{1}{2})(J+\frac{3}{2})B_2^0/T_N\right]. \quad (2.39)$$

The minimum free energy is obtained for $\sigma_\zeta = 0$,

$$\sigma_\xi = \sigma\eta = \sqrt{\frac{\chi_{\xi\xi}^{-1}(\boldsymbol{q})}{8J^2B}}, \tag{2.40}$$

and a phase difference $\phi_\xi - \phi_\eta = \pm\pi/2$. The stable structure thus corresponds to the helix.

In Er where $B_2^0 < 0$ the moments will order in a c-axis modulated structure at the transition temperature:

$$T_N = \frac{\mathcal{J}(\boldsymbol{Q})J(J+1)}{3k_B}\left[1 - \frac{4}{5}(J-\frac{1}{2})(J+\frac{3}{2})B_2^0/T_N)\right], \tag{2.41}$$

with

$$\sigma_\zeta = \sqrt{\frac{\chi_{\zeta\zeta}^{-1}(\boldsymbol{q})}{6J^2B}} \tag{2.42}$$

as the main Fourier component. When the temperature decreases, higher odd harmonics can give contributions to the free energy, and hence the initially pure sinusoidally modulated structure approaches a square wave.

In contrast to the transversely ordered systems, the longitudinal phases are stressed by the two competing requirements, that the moments should order periodically, but with small variations in the magnitude of the moments. As a result the transverse susceptibility can induce a second phase transition, where the moments gain a basal plane component with a phase shift of $\pi/2$ to the c-axis modulation as in an elliptical *cycloidal* structure. Assuming the Landau expansion still to be valid, the transition temperature can be estimated to be:

$$T_N' = \frac{\mathcal{J}(\boldsymbol{Q})J(J+1)}{3k_B}\left[1 + \frac{2}{5}(J-\frac{1}{2})(J+\frac{3}{2})B_2^0/T_N' - \frac{3}{20}(1+\frac{1}{2}(J+1)^{-2})\sigma^2\right]. \tag{2.43}$$

2.4.4 Hexagonal anisotropy — higher harmonics

The sixth order Landau expansion will contain the hexagonal anisotropy B_6^6. This effect is easier illustrated through the free energy expression:

$$F \simeq F_1 - \frac{1}{2}\sum_{ij}\mathcal{J}(ij)\langle\boldsymbol{J}_i\rangle\cdot\langle\boldsymbol{J}_j\rangle + \sum_i B_6^6\langle O_6^6(\boldsymbol{J}_i)\rangle. \tag{2.44}$$

This can be minimized using an assumed structure of the form $\langle\boldsymbol{J}_i\rangle = J\sigma(\cos\phi_i, \sin\phi_i)$ where the angles due to hexagonal symmetry can be expanded from the pure helix in the form: $\phi_i \simeq u_i + \gamma\sin 6u_i + \cdots$, $u_i = \boldsymbol{Q}\cdot\boldsymbol{R}_i$. Further

the expansion $\exp(i(u+\gamma\sin 6u)) \simeq e^{iu} + \frac{\gamma}{2}(e^{i7u} - e^{-i5u}) + \cdots$ allows for a minimization in terms of the expansion parameter:

$$\gamma = \frac{12\kappa_6^6}{(J\sigma)^2\{2\mathcal{J}(\boldsymbol{Q}) - \mathcal{J}(5\boldsymbol{Q}) - \mathcal{J}(7\boldsymbol{Q})\}}, \tag{2.45}$$

where the hexagonal anisotropy energy $\kappa_6^6(T)$ has been estimated in the limit of infinite J by Callen and Callen (1965). By considering the moments σ^n of the relative magnetization σ in an exchange dominated system the temperature dependence of the *Stevens operators* as well as the magnetization itself was obtained a functions of the quantity $x = \beta(\mathcal{J}(\boldsymbol{0})J^2\sigma + g\mu_B JH)$. The relative magnetization was found to be $\sigma = \coth x - \frac{1}{x} = \mathcal{L}(x)$. Hence by writing $x = \mathcal{L}^{-1}(\sigma)$ the expectation value of the Stevens operators and hence the hexagonal anisotropy energy can be expressed in terms of the relative magnetization:

$$\kappa_6^6 = B_6^6 J^{(6)} \hat{I}_{6\frac{1}{2}}[\sigma], \tag{2.46}$$

where $J^{(n)} = \prod_{m=0}^{n-1}(J - m/2)$ i.e. $8^{(6)} = 90090$, and $\hat{I}_{l+\frac{1}{2}}[\sigma] \equiv \hat{I}_{l+\frac{1}{2}}(x)$. The ratio $\hat{I}_{l+\frac{1}{2}} = I_{l+\frac{1}{2}} I_{\frac{1}{2}}$ between the modified Bessel functions can be found from recurrence relations, or estimated in the limits for σ:

$$\hat{I}_{l+\frac{1}{2}}[\sigma] = \begin{cases} \hat{I}_{l-\frac{3}{2}}(x) - \frac{2l-1}{x}\hat{I}_{l-\frac{1}{2}}(x) & x = \mathcal{L}^{-1}(\sigma) \\ \sigma^{l(l+1)/2} & |1-\sigma| \ll 1 \\ \frac{3^l\sigma^l}{(2l+1)!!} & \sigma \ll 1 \end{cases} \tag{2.47}$$

The low temperature limit agrees with a classical consideration of random walk on a sphere (Zener 1951, 1954). For κ_6^6 the σ^{21} dependency is responsible for the rapid decay of the higher harmonics. It should be noted, that from this free energy minimization, it follows that the hexagonal anisotropy distorts the pure helix of periodicity $\boldsymbol{Q}$ with higher harmonics of order $6\boldsymbol{Q} \pm \boldsymbol{Q}$. Both expansions used would, upon inclusion of higher order term, result in $12\boldsymbol{Q} \pm \boldsymbol{Q}$ harmonics. The distortion of the helix will result in additional peaks in the scattering cross-section and the relative amplitude of the 5'th harmonic will be $\gamma^2/4$, which will be discussed in section 5.1.4.

As an example γ can be estimated for Ho in the limit of zero temperature using $B_6^6 = 9.4 \times 10^{-6}$ meV, $\sigma = 1$ and $2\mathcal{J}(\boldsymbol{Q}) - \mathcal{J}(5\boldsymbol{Q}) - \mathcal{J}(7\boldsymbol{Q}) = 0.6374$ meV to $\gamma = 0.25$. This gives a *bunching angle* of $\theta = \pi/12 - \gamma = 0.9°$, which is in poor agreement with the 5.8° that is measured in pure Ho. Hence the expansion is only useful as a qualitative description of the behaviour. But with such a large γ it should be expected that the low order expansion breaks down. The B_6^6 is actually chosen to produce the right bunching angle out of the full mean-field calculations.

2.5 The virtual-crystal model

So far the standard model for a rare earth element has been presented. This chapter describes the generalization of the model to an alloy of two different elements in terms of a *virtual-crystal* (VC) model.

The entire idea of studying a holmium–erbium alloy is based on the very similar chemical properties of the constituents, enabling the formation of a random alloy with a non-distorted uniform *hcp* lattice where each site has a probability n_{Ho} of hosting a Ho atom and $n_{\mathrm{Er}} = 1 - n_{\mathrm{Ho}}$ of hosting an Er atom.

There are basically two main effects on the spin Hamiltonian upon alloying:

- Each lattice point contains either a Ho spin or an Er spin.
- The strength (and types) of the interactions will change.

Each of these effects will be dealt with in the following. If the detailed distribution of the two elements is described by $n_i = 1$ for a Ho atom and $n_i = 0$ for an Er atom, the spin system would be described by the moments $\boldsymbol{J}_i^{\mathrm{VC}} = n_i \boldsymbol{J}_i^{\mathrm{Ho}} \oplus (1 - n_i)\boldsymbol{J}_i^{\mathrm{Er}}$. For notational reasons the moment $\boldsymbol{J}^{n_i}$ is defined to be $\boldsymbol{J}^{\mathrm{Ho}}$ for $n_i = 1$ and $\boldsymbol{J}^{\mathrm{Er}}$ for $n_i = 0$. Since $n_i^2 = n_i$ any functional $\mathcal{O}$ of the moments will give: $\mathcal{O}(\boldsymbol{J}_i^{\mathrm{VC}}) = \mathcal{O}(\boldsymbol{J}_i^{n_i})$.

The Hamiltonian of the system can be written as:

$$\mathcal{H} = \sum_i \mathcal{H}^{n_i}_{\mathrm{one-ion}}(\boldsymbol{J}_i^{\mathrm{VC}}) + \sum_{ij} \mathcal{H}^{n_i,n_j}_{\mathrm{two-ion}}(\boldsymbol{J}_i^{\mathrm{VC}}, \boldsymbol{J}_j^{\mathrm{VC}}), \tag{2.48}$$

where the distinction $\mathcal{H}^{n_i}$ is introduced in order to allow for different interaction parameters depending on the types of spins involved.

The problem of decoupling the Hamiltonian is now to generalize the mean-field approximation on the two-ion term. A general two-ion term can be written in the form:

$$\mathcal{H}^{\mathrm{VC}} = \sum_{ij} \mathcal{K}^{n_i,n_j}(ij)\mathcal{O}(\boldsymbol{J}_i^{\mathrm{VC}})\mathcal{O}'(\boldsymbol{J}_j^{\mathrm{VC}}) = \sum_{ij} \mathcal{K}^{n_i,n_j}(ij)\mathcal{O}(\boldsymbol{J}_i^{n_i})\mathcal{O}'(\boldsymbol{J}_j^{n_j}). \tag{2.49}$$

If the mean-field approximation 2.28 is introduced, the two-ion operator becomes (with a change of summation indices in the last term):

$$\begin{aligned}\mathcal{H}^{\mathrm{VC}}_{\mathrm{MF}} = &\sum_i (\mathcal{O}(\boldsymbol{J}_i^{n_i}) - \frac{1}{2}\langle\mathcal{O}(\boldsymbol{J}_i^{n_i})\rangle) \sum_j \mathcal{K}^{n_i,n_j}(ij)\langle\mathcal{O}'(\boldsymbol{J}_j^{n_j})\rangle \\ &+ \sum_i (\mathcal{O}'(\boldsymbol{J}_i^{n_i}) - \frac{1}{2}\langle\mathcal{O}'(\boldsymbol{J}_i^{n_i})\rangle) \sum_j \mathcal{K}^{n_j,n_i}(ij)\langle\mathcal{O}(\boldsymbol{J}_j^{n_j})\rangle.\end{aligned} \tag{2.50}$$

The evaluation of the mean field:

$$h_i^{n_i} = \sum_j \mathcal{K}^{n_j,n_i}(ij)\langle\mathcal{O}(\boldsymbol{J}_j^{n_j})\rangle \tag{2.51}$$
$$= \sum_j n_j\mathcal{K}^{n_j,n_i}(ij)\langle\mathcal{O}(\boldsymbol{J}_j^{\mathrm{Ho}})\rangle + \sum_j (1-n_j)\mathcal{K}^{n_j,n_i}(ij)\langle\mathcal{O}(\boldsymbol{J}_j^{\mathrm{Er}})\rangle$$

is accomplished by the approximation $n_j \simeq n_{\mathrm{Ho}}$. Hence the mean field is calculated as the mean field in a Ho crystal times n_{Ho} plus $1 - n_{\mathrm{Ho}}$ times the mean field in an Er crystal.

The idea behind the virtual-crystal model can be viewed as the approximation $n_i \simeq n_{\mathrm{Ho}}$ which corresponds to placing a composite moment on each lattice site. The problem in this approximation is that $n_i^2 = n_i$ whereas $n_{\mathrm{Ho}}^2 \neq n_{\mathrm{Ho}}$. That is whenever a product J_iJ_j appears an error will build up. Therefore the approximation is only inserted where necessary.

The Hamiltonian is now brought on a decoupled form $\mathcal{H} = \sum_i \mathcal{H}(i)$, and can be solved for each i at a time. However, since the mean field is to be calculated with both a holmium and an erbium atom at site i, the Hamiltonian has to be solved for both $n_i = 1$ and $n_i = 0$.

It now remains to consider the effect of alloying upon the strength of the interactions:

- The *Zeeman* term due to an external field must be the same as in the pure elements.
- The crystal field due to the charge distribution in the crystal will of course be affected, but the change is assumed small and is neglected. Each erbium nuclei will have one more unit charge, but on the other side will there be one more $4f$ electron to shield it. For each type of ion, the parameters for the corresponding pure elements are therefore used without any modification.
- The exchange interaction must deal with 3 cases namely Ho-Ho, Ho-Er and Er-Er interactions. The mediating conduction electron gas will change.

  This change is assumed to be a weighted average. But since the exchange interaction actually operates on the spins $\boldsymbol{S} = (g-1)\boldsymbol{J}$ the scaling is performed before the transition to the $\boldsymbol{J}$ operators:

$$\mathcal{J}^0 = n_{\mathrm{Ho}}\mathcal{J}^{\mathrm{Ho}}/(g_{\mathrm{Ho}}-1)^2 + n_{\mathrm{Er}}\mathcal{J}^{\mathrm{Er}}/(g_{\mathrm{Er}}-1)^2. \tag{2.52}$$

  The parameters are then scaled with $(g-1)$:

$$\begin{aligned}\mathcal{J}^{\mathrm{Ho-Ho}} &= \mathcal{J}^0(g_{\mathrm{Ho}}-1)^2\\ \mathcal{J}^{\mathrm{Ho-Er}} &= \mathcal{J}^0(g_{\mathrm{Ho}}-1)(g_{\mathrm{Er}}-1)\\ \mathcal{J}^{\mathrm{Er-Er}} &= \mathcal{J}^0(g_{\mathrm{Er}}-1)^2.\end{aligned} \tag{2.53}$$

- The classical dipole interaction is proportional to $\mathcal{J}_{dd} = N/V(g\mu_B)^2$. Since the alloy is assumed to form a uniform lattice $V/N = \sqrt{3}a^2c/4$ must be given by the averaged crystal parameters $a = n_{\mathrm{Ho}}a_{\mathrm{Ho}} + n_{\mathrm{Er}}a_{\mathrm{Er}}$. The three types of coupling are then scaled with g_{Ho}^2, $g_{\mathrm{Ho}}g_{\mathrm{Er}}$, g_{Er}^2 respectively. For consistency with the pure holmium model all of the parameters are added the 3% conduction electron polarization correction found in holmium.

- The higher order anisotropic interactions are so much weaker than the exchange interaction, that their Ho-Er part is neglected. That is they are calculated only for the Ho-Ho and the Er-Er interactions.

The virtual-crystal model as presented thus contains no free parameters, since the parameters are determined from the pure Ho and Er models.

2.6 Calculations

Based on the presented mean-field Hamiltonian a computer program has been developed, which enables iterative determination of the equilibrium structures for the system.

$\mathcal{J}(\boldsymbol{q})$ has maximum in the c-direction, and hence each ab-plane orders ferromagnetically. Therefore the calculations can be simplified to a 1D structure in the c-direction. The two-ion interactions are then averaged over each layer.

In the actual calculations only a finite number of layers can be treated. This enforces a certain periodicity $\boldsymbol{Q} = \boldsymbol{c}^* m/N$ given by the number of repetitions m during the number of double layers N.

The calculation is initiated with a guess of the arrangement of the $2N$ single layers. Then using periodic boundary conditions, the mean-field for the i'th layer is calculated, and the corresponding Hamiltonian $\mathcal{H}_i$ constructed and diagonalized. From the eigenvectors and eigenvalues, new thermal expectation values $\langle \boldsymbol{J}_i \rangle$ and $\langle O_3^{\pm 2} \rangle$ are calculated. This procedure is cyclically iterated until convergence.

For most of the structures investigated, convergence was reached within reasonable time, except in the vicinity of a second order phase transition, where the convergence times increased substantially. However, the investigation of the disordered 7/36 structures, where an increasing number of blocks of respective 5 and 7 layers were mixed at random, the calculations became a comprehensive computational task.

Once satisfactory convergence is achieved, any physical observable can be calculated from the $2N$ set of eigenvectors and eigenvalues. The quantities of primary interest are of course $\langle \boldsymbol{J}_i \rangle$ and the total free energy $\sum_{ni} n_{ni}\varepsilon_{ni}$.

In principle the combination m, N, resulting in least free energy after convergence of the mean-field iterations, should be the most stable structure. The success of such a free energy minimization is however very limited. Thus the periodicity Q is a free parameter, that has to be chosen to fit the structures observed in experiments.

Chapter 3

Magnetic structures — classification

The maximum exchange interaction for non zero $\boldsymbol{q} \parallel \boldsymbol{c}^*$ produces periodic structures in the c-direction while the ab-planes order ferro-magnetically. The anisotropic fields and interactions determine the actual form of these structures.

In order to understand and discuss the details of the structures, it is necessary to describe them and to introduce some kind of classification.

The periodicity $\boldsymbol{Q}$ is generally incommensurate with the *reciprocal lattice* $\boldsymbol{\tau}$, but the anisotropic crystal field couples the energy of the magnetic periodicity to the lattice, and hence lock-in to commensurate structures are seen in both erbium (Cowley and Jensen 1992) and holmium (Jensen 1996a).

3.1 Basic structures

Throughout the entire series of rare earth magnetic ordering there are some basic structures, which are seen in many different cases. In figure 3.1 they are drawn with the origin of the moments condensed in the same point.

The *helix* is described by:

$$\langle \boldsymbol{J}_i \rangle = J\sigma(\cos\phi, \sin\phi, 0), \tag{3.1}$$

where $\phi = \boldsymbol{Q} \cdot \boldsymbol{R}_i + \phi_0$. It can be visualized as a spiral staircase, where the moments rotate at a constant angle $\Delta\phi = \boldsymbol{Q} \cdot \boldsymbol{c}/2$ between succeeding planes. In its pure form the helix is described by the order parameter σ and the periodicity $\boldsymbol{Q}$.

A variant of the flat basal plane helix is the *cone* structure:

$$\langle \boldsymbol{J}_i \rangle = J\sigma(\cos\theta\cos\phi, \cos\theta\sin\phi, \sin\theta), \tag{3.2}$$

where a ferromagnetic component is added to the helix in the c-direction. The cone phase is characterized with the cone angle θ_{Cone} defined as the angle from

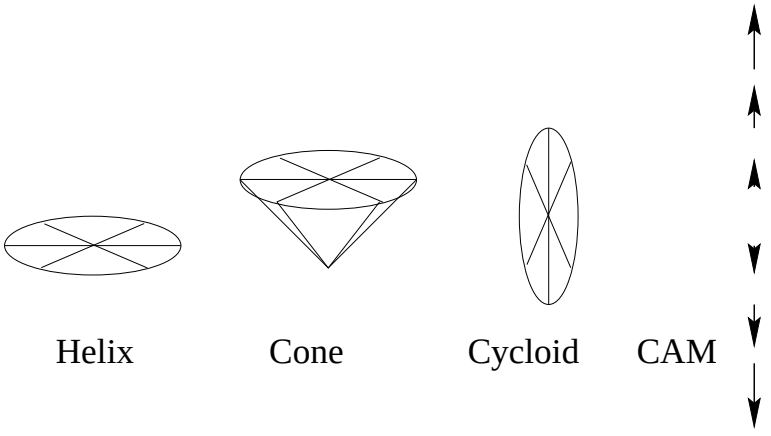

Figure 3.1: Four basic magnetic structures

the cone to the basal plane. The cone angle is sometimes defined as the opening angle or half the opening angle of the cone, but the chosen definition has the nice property, that it is zero for the basal plane helix.

Another variant of the helix is the *tilted helix* which is a helix with a modulated c-axis component of the same periodicity as the helix.

The tilted helix was predicted in Ho by Sherrington (1972). Within the model Hamiltonian:

$$\mathcal{H} = -\sum_{ij} \mathcal{J}(ij)\boldsymbol{S}_i \cdot \boldsymbol{S}_j + \sum \mathcal{K}_2 S_{zi}^2 + \sum \mathcal{K}_4 S_{zi}^4, \tag{3.3}$$

where the effective anisotropy $|\mathcal{K}_2|$ is assumed to increase as the temperature is lowered, the static semi-classical energy minimization separates the helix and the cone phase by the condition $\mathcal{K}_2 \gtrless \mathcal{J}(\mathbf{0}) - \mathcal{J}(\boldsymbol{Q})$. But by transforming the elementary excitations into Holstein–Primakoff boson operators the requirements for both of the phases are seen to become more stringent: respective $\mathcal{K}_2 > 0$ and $\mathcal{K}_2 < \frac{2}{3}(\mathcal{J}(\mathbf{0}) - \mathcal{J}(\boldsymbol{Q}))$, hence leaving an intermediate region, where the tilted helix should be prefered. The following phase transitions were proposed:

$$\text{Helix} \overset{\text{2. order}}{\longrightarrow} \text{ tilted helix} \overset{\text{1. order}}{\longrightarrow} \text{ cone.}$$

Mean-field calculations do not give the same picture, although calculations on the cone and the tilted helix in holmium predict that they are very close in energy. The energy difference is as small as -16.791 meV compared to -16.782 meV in the zero temperature limit of holmium.

The tilted helix has not yet been observed in any of the rare earths. As discussed in section 5.2.3, some early data from the $Ho_{90}Er_{10}$ crystal indicated a tilted helix, but the data could not be reproduced.

There exist other structures with a varying c-axis component, two of which appear in erbium. Below the Néel temperature erbium forms a c-axis modulated (CAM) structure where $\langle J_z \rangle = J\sigma \cos\phi$ while the basal plane components are zero. Below a second transition temperature an a-axis component with the same periodicity develops (the a-axis is an *easy axis* in Er). This elliptical structure is called a *cycloid*.

Other forms of structures have been observed in the rare earths, but the above are the ones of interest in this context.

3.2 Spin slips

One of the sources for distortion of the pure structures is the hexagonal anisotropy which becomes important at low temperatures. As mentioned in section 2.2.2 the hexagonal anisotropy pushes the spins in a helix towards the nearest easy axis. Thus two succeeding spins in the same *hexant* will "*bunch*" in a pair. A single spin in a hexant will align in the middle easy direction and is called a singlet or a *spin slip*, since one spin in a pair is missing. These effects can be included in the classification of the structure by introducing the *bunching angle* θ_{Bunch} from one spin in a pair to the easy axis, and a scheme for where the spin slips appear. The detailed scattering from holmium was explained by Cowley

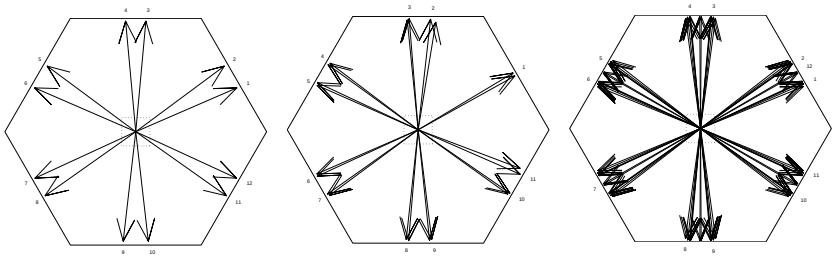

(a) Ho 1/6 (b) Ho 2/11 (c) $Ho_{90}Er_{10}$ 7/36

Figure 3.2: Basal plane spin arrangements in Ho 1/6, 2/11 and $Ho_{90}Er_{10}$ 7/36

and Bates (1988) in terms of an average distance b between spin slip, a Gaussian distance distribution σ and a bunching angle α. Later the commensurable structures in both holmium and erbium have been interpreted in terms of spin slip structures with a fixed repetition scheme for the spin slips. For instance, the low temperature structure in holmium has $Q = 1/6$ corresponding to a full turn in 12 layers. Hence there will be two spins in each hexant and no spin slips (see figure 3.2(a)). But at higher temperatures the periodicity increases and passes $Q = 2/11$ which corresponds to a spin slip after five pairs (figure 3.2(b)). This structure will be denoted (222221). The structure believed to exist in $Ho_{90}Er_{10}$ below 25 K has $Q = 7/36$ and makes 7 complete turns in 72

layers (figure 3.2(c)). The simple spin slip structure for this periodicity is (2221 221) which can also be expressed as {43}. The latter notation expresses the fact that there are 4 and then 3 hexants between the spin slips (the hexant with the spin slip is included). Following Cowley and Bates (1988), such a composite spin slip structure can be described by a set (b_n) describing the number of layers between the spin slips. The periodicity of a spin slip structure (b_n) is given by $Q = \sum(b_n + 1)/6 \sum b_n$ or in terms of an average length $b = \sum b_n$ between each spin slip $Q = 1/6 + 1/6b$. In this notation the $Q = 7/36 = (8 + 6)/6(7 + 5)$ structure is given by (7 5), hence alternating 7 and 5 layers between each spin slip.

When performing calculations of free energy or the scattering cross-section it is useful to have an analytic expression for $\langle \boldsymbol{J}_n \rangle$ instead of a spin slip notation like (2221 221). A simple expansion on the basis of the simple helix is

$$\phi_n = u_n + \gamma \sin 6u_n, \quad \text{where} \quad u_n = \boldsymbol{Q} \cdot \boldsymbol{R}_n. \tag{3.4}$$

For the 1/6 no-spin-slip structure in Ho $\boldsymbol{Q} \cdot \Delta\boldsymbol{R} = \pi/6$ and $u_n = n\pi/6 + u_0$, so $\Delta\phi = \pi/6 \pm 2\gamma$ and hence the bunching angle $\theta = \pi - \gamma$ can be determined. The spin slip structures are only partly described by 3.4. As seen in figure 3.3

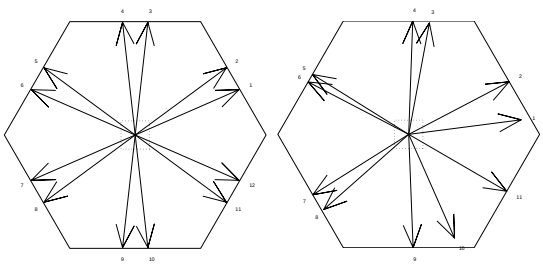

(a) 1/6 (b) 2/11

Figure 3.3: Basal plane spin arrangement as given by $\phi = u + \gamma \sin u$.

the bunching angles do not correspond to the real behaviour of the system in figure 3.2.

Chapter 4

The experiment

Different magnetic phases of the rare earths were originally indicated by anomalies in quantities like the specific heat. The periodic magnetic structures were somewhat implied by *magnetization* measurements, but not until the application of neutron scattering experiments were the structures determined.

The utility of the neutron as a probe for magnetic properties can be summarized

- Through its spin it interacts with magnetic moments in the material.
- The neutral charge allows it to penetrate the crystal thus probing the bulk properties.
- Thermal neutrons have energies of $5 - 25$ meV and $\lambda \sim 4 - 2$Å, which is comparable with both lattice and spin wave quantities.

Scattering experiments are characterized by a scattering cross-section describing the scattered intensity as a function of energy and wave vector transfers. The magnetic scattering cross-section contains enough information to almost uniquely determine the magnetic structure of a system.

Some of the draw backs of neutron scattering are the relatively low intensities and resolutions in comparison to for instance *x-ray* scattering. Nevertheless, as long as the system is properly ordered and not too complex, neutron scattering seems to be the perfect tool for this investigation.

Neutron scattering experiments were performed with the TAS1 triple axis spectrometer at the DR3 reactor, Risø.

4.1 Neutron scattering

In a scattering experiment an incoming beam of neutrons in initial state $|\boldsymbol{k}, \sigma\rangle$ interact with a target and makes a transition to a final state $\left|\boldsymbol{k}', \sigma'\right\rangle$. At the same time the target goes from state $|i\rangle$ to state $|f\rangle$. The monochromatic and collimated beam of neutrons which is used in scattering experiments can

be treated as a plane wave state $|\boldsymbol{k},\sigma\rangle = \frac{1}{\sqrt{V}}e^{i\boldsymbol{k}\cdot\boldsymbol{r}}|\sigma\rangle$. The probability for a transition is to first approximation given by *Fermi's golden rule* applied to the interaction Hamiltonian:

$$W(\boldsymbol{k},\sigma;\boldsymbol{k}',\sigma') = \frac{2\pi}{\hbar}\sum_{if} P_i \left|\langle \boldsymbol{k},\sigma;i|\,\mathcal{H}_{\text{int}}\left|\boldsymbol{k}'\sigma';f\right\rangle\right|^2 \delta(\hbar\omega - E_f + E_i), \tag{4.1}$$

where P_i is the relative occurrence of the initial state $|i\rangle$ and $\hbar\omega = \hbar^2 k'^2/2m - \hbar^2 k^2/2m$ is the energy transfer.

Using the plane wave states $\langle \boldsymbol{k}|\,\mathcal{H}_{\text{int}}\left|\boldsymbol{k}'\right\rangle = 1/V\int \mathcal{H}_{\text{int}} e^{i(\boldsymbol{k}'-\boldsymbol{k})\cdot\boldsymbol{r}}$ which is nothing but the Fourier transform $\mathcal{H}_{\text{int}}(\boldsymbol{\kappa})$ where $\boldsymbol{\kappa} = \boldsymbol{k}' - \boldsymbol{k}$ is the wave vector transfer. The incoming flux in a state with wave vector $\boldsymbol{k}$ is $\hbar k/VM$ and the number of neutrons in a small energy interval dE around $\hbar^2k^2/2M$ is given by $\delta N = V/8\pi^3(Mk'/\hbar^2)dEd\Omega$. Together this gives a scattering cross-section:

$$\frac{d^2\sigma}{dEd\Omega} = \frac{k'}{k}\frac{M^2}{8\pi^3\hbar^3}W(\boldsymbol{k},\sigma;\boldsymbol{k}',\sigma'). \tag{4.2}$$

There are two means of scattering of an incoming neutron. Firstly the nuclei interacts with the neutron. Secondly the neutron spin interacts with the charged electrons in the target.

4.1.1 Nuclear scattering

Since the wavelength of the neutron is about 5 orders of magnitude larger than the nuclear force range, the scattered waves from a single fixed nuclei will be spherical symmetric of the form $\psi = -\frac{b}{r}e^{i\boldsymbol{k}\cdot\boldsymbol{r}}$. The scattering length b expresses the strength of the interaction, has to be determined experimentally. The corresponding cross-section is found to be $\frac{d\sigma}{d\Omega} = b^2$, which can also be obtained from equation 4.2 by introducing the *Fermi pseudo-potential*:

$$\begin{aligned} V(\boldsymbol{r}) =& \frac{2\pi\hbar^2}{m}b\delta(\boldsymbol{r}) \\ V(\boldsymbol{\kappa}) =& \int V(\boldsymbol{r})e^{i\boldsymbol{\kappa}\cdot\boldsymbol{r}}d\boldsymbol{r} = \frac{2\pi\hbar^2}{m}b. \end{aligned} \tag{4.3}$$

Assuming the pseudo-potential also to be valid in a solid, the interaction with a crystal is given by the sum $V = \sum_j V_j(\boldsymbol{r} - \boldsymbol{R}_j)$ over all nuclei. The resulting scattering cross-section is given by:

$$\frac{d^2\sigma}{d\Omega dE} = \frac{k'}{k}\sum_{if} P_i \left|\sum_j b_j\langle i|e^{i\boldsymbol{\kappa}\cdot\boldsymbol{R}_j}|f\rangle\right|^2 \delta(\hbar\omega - E_f + E_i). \tag{4.4}$$

The expression can be rewritten using five important ingredients:

- The integral representation of the energy δ-function:

$$\delta(\hbar\omega - E_f + E_i) = \frac{1}{2\pi\hbar}\int e^{-i(\hbar\omega - E_f + E_i)t/\hbar}dt \tag{4.5}$$

- The simple norm equality: $|ab| = ab^*$
- The completeness relation: $1 = \sum_f |f\rangle\langle f|$
- The thermal expectation value: $\langle A\rangle = \sum_i P_i\langle i|A|i\rangle$
- The time dependent Heisenberg operators $A(t) \equiv e^{i\mathcal{H}t/\hbar}Ae^{-i\mathcal{H}t/\hbar}$

which straightforwardly gives:

$$\frac{d^2\sigma}{d\Omega dE} = \frac{k'}{k}\frac{1}{2\pi\hbar^2}\sum_{jj'} b_j b_{j'}\int\langle e^{i\boldsymbol{\kappa}\cdot\boldsymbol{R}_j(0)}e^{-i\boldsymbol{\kappa}\cdot\boldsymbol{R}_{j'}(t)}\rangle e^{-i\omega t}dt. \tag{4.6}$$

As a first approach, the time dependence can be treated in the harmonic crystal approximation, where $\boldsymbol{R}_j(t) = \boldsymbol{R}_j + \boldsymbol{u}_i(t)$. Neglecting all phonon processes, the thermal expectation value in equilibrium is given by:

$$\langle e^{i\boldsymbol{\kappa}\cdot(\boldsymbol{R}_j(0) - \boldsymbol{R}_{j'}(t))}\rangle \simeq e^{-W_j(\kappa) - W_{j'}(\kappa)}e^{i\boldsymbol{\kappa}\cdot(\boldsymbol{R}_j - \boldsymbol{R}_{j'})}, \tag{4.7}$$

where $W(\kappa) \sim \kappa^2\langle u_j^2\rangle/6$ is the *Debye–Waller factor*. Reintroducing the energy δ-function and integrating over energy, the elastic scattering cross-section becomes:

$$\left(\frac{d^2\sigma}{d\Omega}\right)_{\text{el}} = \left|\sum_j b_j e^{-W_j(\kappa)}e^{i\boldsymbol{\kappa}\cdot\boldsymbol{R}_j}\right|^2. \tag{4.8}$$

By writing the position of the $\boldsymbol{d}$'th atom in the $\boldsymbol{l}$'th unit cell of a *non-Bravais lattice* as $\boldsymbol{R}_{\boldsymbol{ld}} = \boldsymbol{l} + \boldsymbol{d} + \boldsymbol{u}_{\boldsymbol{ld}}$, the sum can be split according to:

$$\begin{aligned}
\left(\frac{d^2\sigma}{d\Omega}\right)_{\text{el}} &= \left|\sum_{\boldsymbol{l}} e^{i\boldsymbol{\kappa}\cdot\boldsymbol{l}}\sum_{\boldsymbol{d}} b_{\boldsymbol{d}}e^{-W_{\boldsymbol{d}}(\kappa)}e^{i\boldsymbol{\kappa}\cdot\boldsymbol{R}_{\boldsymbol{d}}}\right|^2 \\
&= N\sum_{\boldsymbol{l}} e^{i\boldsymbol{\kappa}\cdot\boldsymbol{l}}\left|\sum_{\boldsymbol{d}} b_{\boldsymbol{d}}e^{-W_{\boldsymbol{d}}(\kappa)}e^{i\boldsymbol{\kappa}\cdot\boldsymbol{R}_{\boldsymbol{d}}}\right|^2 \\
&= N\frac{8\pi^3}{v_0}\sum_{\boldsymbol{\tau}}\delta(\boldsymbol{\kappa} - \boldsymbol{\tau})\left|\sum_{\boldsymbol{d}} e^{-2W_{\boldsymbol{d}}(\kappa)}b_{\boldsymbol{d}}e^{i\boldsymbol{\kappa}\cdot\boldsymbol{R}_{\boldsymbol{d}}}\right|^2 \\
&= N\frac{8\pi^3}{v_0}\sum_{\boldsymbol{\tau}}\delta(\boldsymbol{\kappa} - \boldsymbol{\tau})|F_N(\boldsymbol{\kappa})|^2,
\end{aligned} \tag{4.9}$$

where the translational symmetry of $\boldsymbol{l}$ and the definition of the *reciprocal lattice* points $\boldsymbol{\tau}$ has been exploited. $F_N(\boldsymbol{\kappa}) = \sum_{\boldsymbol{d}} b_{\boldsymbol{d}} e^{-W_{\boldsymbol{d}}(\kappa)} e^{i\boldsymbol{\kappa}\cdot\boldsymbol{d}}$ is the *nuclear structure factor*. If the *Debye–Waller factor* $W_{\boldsymbol{d}}$ and the scattering length $b_{\boldsymbol{d}}$ are site independent, they can be extracted from the summation, which then reduces to the *geometric structure factor*: $F_G(\boldsymbol{\kappa}) = \sum_{\boldsymbol{d}} e^{i\boldsymbol{\kappa}\cdot\boldsymbol{d}}$. The δ-function will cause Bragg peaks at each reciprocal lattice point $\boldsymbol{\tau}$, weighted by the structure factor, which determines the phase and possible extinction of the Bragg peaks (see figure 4.1). In the *hcp* lattice there are two ions per unit cell. For a wave vector transfer $\boldsymbol{\kappa} = (h, k, l)$ this gives a structure factor of:

$$F_G(\boldsymbol{\kappa}) = e^{i\boldsymbol{\kappa}\cdot\boldsymbol{d}_0} + e^{i\boldsymbol{\kappa}\cdot\boldsymbol{d}_1} = 1 + e^{2\pi i(2h/3+k/3+l/2)}. \tag{4.10}$$

It should be noticed, that $(0, 0, 1)$ is extinct by the structure factor $F_N(0, 0, 1) = 0$. This is a reminiscence of the fact, that c is twice the distance between succeeding basal planes. Such extinct points are called forbidden reflections.

The presence of different isotopes or nuclear spins would result in different scattering lengths b^ξ with relative occurrence c_ξ. If the variation is assumed to be uncorrelated, then:

$$b_j^\xi b_{j'}^{\xi'} \simeq \overline{b_j b_{j'}} = \left\{ \begin{array}{ccc} \overline{b}_j \overline{b}_{j'} & \text{for} & j \neq j' \\ \overline{b_j^2} & \text{for} & j = j' \end{array} \right\} = \overline{b}_j \overline{b}_{j'} + \delta_{jj'}(\overline{b_j^2} - \overline{b}_j^2), \tag{4.11}$$

where e.g. $\overline{b} = \sum_\xi c_\xi b^\xi$ is the compositional average. This splits the cross-section into a coherent and an incoherent part. The incoherent part deals with the same nuclei at different times, and is therefore not interesting in elastic experiments. The coherent scattering length $\overline{b}$ can be substituted into the expressions for the scattering cross-section derived above.

4.1.2 Magnetic scattering

The interaction between a neutron with magnetic dipole moment $\boldsymbol{\mu}_n = -g_n \mu_N \boldsymbol{s}_n$ at position $\boldsymbol{r}_n$ with an electron of charge e, spin $\boldsymbol{s}$ with momentum $\boldsymbol{p}$ at position $\boldsymbol{r}_e$ can be calculated by inspecting the electron energy with and without the neutron present. The neutron gives rise to a vector potential $\boldsymbol{A}_n = \boldsymbol{\mu}_n \times \boldsymbol{r}/r^3$ and for generality an external vector potential $\boldsymbol{A}_e$ is assumed. The interaction Hamiltonian is then to first order in μ_N given by:

$$\begin{aligned} \mathcal{H}_{\text{int}} &= \frac{1}{2m}(\boldsymbol{p} + \frac{e}{c}(\boldsymbol{A}_n + \boldsymbol{A}_e))^2 + 2\mu_B \boldsymbol{s}\cdot\boldsymbol{B}_n - \frac{1}{2m}(\boldsymbol{p} + \frac{e}{c}\boldsymbol{A}_e)^2 \\ &= 2\mu_B(\frac{1}{\hbar}\boldsymbol{A}_n \cdot \boldsymbol{p}' + \boldsymbol{s}\cdot(\nabla \times \boldsymbol{A}_n)), \end{aligned} \tag{4.12}$$

where $\boldsymbol{p}' = \boldsymbol{p} + \frac{e}{c}\boldsymbol{A}_e$. This is Fourier transformed into:

$$\mathcal{H}_{\text{int}}(\boldsymbol{\kappa}) = 8\pi\mu_B \boldsymbol{\mu}_n \cdot (\frac{i}{\hbar\kappa}\hat{\boldsymbol{\kappa}} \times \boldsymbol{p}' + \hat{\boldsymbol{\kappa}} \times \boldsymbol{s} \times \hat{\boldsymbol{\kappa}}) e^{-i\boldsymbol{\kappa}\cdot\boldsymbol{r}_e}. \tag{4.13}$$

The expression consists of an orbital part and a spin part. The orbital motion is dealt with by splitting $\boldsymbol{r}_e = \boldsymbol{R}_j + \boldsymbol{r}$ into the position of the j'th atom and the motion around the atom. Under certain assumptions, the orbital and the spin part can be joined using the Bessel-function expansion of the exponential $e^{-i\boldsymbol{\kappa}\cdot\boldsymbol{r}}$:

$$\mathcal{H}_{\rm int}(\boldsymbol{\kappa}) = 8\pi\mu_B \sum_j \{\tfrac{1}{2} g F(\boldsymbol{\kappa})\}_j e^{-i\boldsymbol{\kappa}\cdot\boldsymbol{R}_j} \boldsymbol{\mu}_n \cdot (\hat{\boldsymbol{\kappa}} \times \boldsymbol{J}_j \times \hat{\boldsymbol{\kappa}}), \tag{4.14}$$

where the summation runs over all atoms in the target. $F(\boldsymbol{\kappa}) = < j_0 > + (\frac{2}{g} - 1) < j_2 >$ is called the *magnetic form factor* and expresses the coupling of the orbital and the spin part. To lowest order in the expansion, $F(\boldsymbol{\kappa})$ is independent of the direction of $\boldsymbol{\kappa}$, and is determined by the radial average of the Bessel functions: $< j_n >= \int_0^\infty r^2 R^2(r) j_n(\kappa r) dr$. In the data analysis the magnetic form factor is calculated using the analytic approximation produced by Jane Brown (ILL): $< j_n >= \sum_m j^{\rm amp}_{n,m} e^{-j^{\rm arg}_{n,m}(\kappa/4\pi)^2}$ with the parameters given in table 4.1.

	m	0	1	2	3
Ho	$j^{\rm amp}_{0,m}$	-0.0248	0.0566	0.3365	0.6317
	$j^{\rm arg}_{0,m}$	0.0	18.318	7.688	2.943
	$j^{\rm amp}_{2,m}$	0.0268	0.2188	1.024	0.9251
	$j^{\rm arg}_{2,m}$	0.0	18.516	6.707	2.161
Er	$j^{\rm amp}_{0,m}$	-0.0251	0.0586	0.3540	0.6126
	$j^{\rm arg}_{0,m}$	0.0	17.980	7.096	2.748
	$j^{\rm amp}_{2,m}$	0.0278	0.1710	0.9879	0.9044
	$j^{\rm arg}_{2,m}$	0.0	18.534	6.625	2.100

Table 4.1: Parameters for the form factor in Ho and Er.

The neutron spin matrix elements can be evaluated assuming unpolarized neutrons. The squared matrix element is treated as:

$$|\langle\sigma|\,\mathcal{H}\,|\sigma'\rangle|^2 = \langle\sigma|\,\mathcal{H}\,|\sigma'\rangle\,\langle\sigma'|\,\mathcal{H}\,|\sigma\rangle\,, \tag{4.15}$$

and the summation over outgoing spin σ' is seen as the identity. The remaining expectation value can be evaluated using the Pauli representation and expressing $\boldsymbol{J}$ in cartesian components labeled α, β. Combining the numeric factors using the neutron gyro magnetic ratio $\gamma = \frac{g_n}{2\hbar}$, the classical electron radius $\frac{e^2}{mc^2}$ and the vector relation $(\hat{\boldsymbol{\kappa}}\times\boldsymbol{J}_j\times\hat{\boldsymbol{\kappa}})\cdot(\hat{\boldsymbol{\kappa}}\times\boldsymbol{J}_j\times\hat{\boldsymbol{\kappa}}) = \sum_{\alpha\beta}(\delta_{\alpha\beta} - \hat{\kappa}_\alpha\hat{\kappa}_\beta)$, the differential cross-section becomes:

$$\frac{d^2\sigma}{dEd\Omega} = \frac{k'}{k}\left(\frac{\hbar\gamma e^2}{mc^2}\right)^2 \sum_{\alpha\beta}(\delta_{\alpha\beta} - \hat{\kappa}_\alpha\hat{\kappa}_\beta)\sum_{jj'}\{\tfrac{1}{2}gF(\boldsymbol{\kappa})\}_j\{\tfrac{1}{2}gF(\boldsymbol{\kappa})\}_{j'} \times \sum_{if} P_i\langle i|J_{j\alpha}e^{-i\boldsymbol{\kappa}\cdot\boldsymbol{R}_j}|f\rangle\langle f|J_{j'\beta}e^{-i\boldsymbol{\kappa}\cdot\boldsymbol{R}'_j}|i\rangle\delta(\hbar\omega - E_f + E_i). \quad (4.16)$$

Using the integral representation of $\delta(\hbar\omega - E_f + E_i)$ and subsequently exploiting the eigenvalue nature of E_i and E_j to move them inside the first matrix element the f summation can be seen as the identity and hence removed. Defining the time dependent operators $J(t) = e^{i\mathcal{H}t/\hbar}Je^{-i\mathcal{H}t/\hbar}$ in the Heisenberg picture and viewing the i sum as the thermal average, the *Debye-Waller factor* can be introduced. Then the cross-section becomes:

$$\frac{d^2\sigma}{dEd\Omega} = \frac{k'}{k}\left(\frac{\hbar\gamma e^2}{mc^2}\right)^2 \sum_{\alpha\beta}(\delta_{\alpha\beta} - \boldsymbol{\kappa}_\alpha\boldsymbol{\kappa}_\beta)\sum_{jj'}\{\tfrac{1}{2}gF(\boldsymbol{\kappa})\}_j\{\tfrac{1}{2}gF(\boldsymbol{\kappa})\}_{j'} \times \frac{1}{2\pi\hbar}\int dt e^{i\omega t}e^{-i\boldsymbol{\kappa}(\boldsymbol{R}_j - \boldsymbol{R}_{j'})}\langle J_{j\alpha}(t)J_{j'\beta}(0)\rangle. \quad (4.17)$$

If the magnetic form factor is site independent (one element with identical sites) the cross-section can be expressed in terms of the Van Hove scattering function

$$S^{\alpha\beta}(\boldsymbol{\kappa},\omega) = \frac{1}{2\pi\hbar}\int dt e^{i\omega t}\frac{1}{N}\sum_{jj'}e^{-i\boldsymbol{\kappa}(\boldsymbol{R}_j - \boldsymbol{R}_{j'})}\langle J_{j\alpha}(t)J_{j'\beta}(0)\rangle, \quad (4.18)$$

which in hand can be separated $S^{\alpha\beta}(\boldsymbol{\kappa},\omega) = \delta(\hbar\omega)S^{\alpha\beta}_{\mathrm{el}}(\boldsymbol{\kappa}) + S^{\alpha\beta}_{\mathrm{d}}(\boldsymbol{\kappa},\omega)$ into an elastic part

$$S^{\alpha\beta}_{\mathrm{el}}(\boldsymbol{\kappa}) = \frac{1}{N}\sum_{jj'}e^{-i\boldsymbol{\kappa}(\boldsymbol{R}_j - \boldsymbol{R}_{j'})}\langle J_{j\alpha}\rangle\langle J_{j'\beta}\rangle, \quad (4.19)$$

and an inelastic part which through the fluctuation dissipation theorem is related to the generalized susceptibility:

$$S^{\alpha\beta}_{\mathrm{d}}(\boldsymbol{\kappa},\omega) = \frac{1}{\pi}\frac{1}{1 - e^{-\beta\hbar\omega}}\chi''_{\alpha\beta}(\boldsymbol{\kappa},\omega). \quad (4.20)$$

For an alloy in the *virtual-crystal* notation, one replaces:

$$\{\tfrac{1}{2}gF(\boldsymbol{\kappa})\}\boldsymbol{J} \to \sum_{\xi}\{\tfrac{1}{2}gF(\boldsymbol{\kappa})\}_\xi c_\xi \boldsymbol{J}_\xi, \quad (4.21)$$

and $S^{\alpha\beta}$ is replaced by $S^{\alpha\beta}_{\xi\xi'}$. $S_{\xi\xi'}$ and $\chi_{\xi\xi'}$ are defined through $\langle \boldsymbol{J}_\xi \boldsymbol{J}'_\xi \rangle$.

Since the dynamic contribution $S_d(\boldsymbol{\kappa}, \omega)$ is distributed in reciprocal space, the main contribution to the energy integrated cross-section $d\sigma/d\Omega$ will be the just derived elastic term. Therefore as opposed to elastic scattering experiments, where only neutrons with wave vector $\boldsymbol{k}'$ are detected, one can do neutron diffraction by counting all neutrons in the direction of $\boldsymbol{k}'$. The advantage of this procedure is the gain in intensity obtained by leaving out the analyser crystal, which filters the scattered neutrons by wave length. Possible limits for the approximation are near phase transitions, where critical fluctuations will cause considerable quasi elastic scattering.

4.1.3 Elastic scattering

Just as for the nuclear scattering the summation over lattice sites can be separated into two summations over unit cells and over atoms in the unit cell respectively. Several of the simple structures can be represented by a spin configuration like:

$$\langle \boldsymbol{J}_j \rangle = \Re(\langle \boldsymbol{J} \rangle \, e^{iQ\cdot \boldsymbol{R}_j}) = \frac{1}{2}(\langle \boldsymbol{J} \rangle \, e^{iQ\cdot \boldsymbol{R}_j} + \langle \boldsymbol{J} \rangle^* \, e^{-iQ\cdot \boldsymbol{R}_j}). \tag{4.22}$$

Using the symmetry in α, β and the definition of the reciprocal lattice vectors τ the elastic contribution to the cross-section for a *Bravais lattice* becomes:

$$\begin{aligned}\frac{d\sigma}{d\Omega} =& \frac{8\pi^3 N}{v_0}\left(\frac{\hbar\gamma e^2}{mc^2}\right)^2 e^{-2W(\kappa)} |\tfrac{1}{2} g F(\boldsymbol{\kappa})|^2 \sum_{\alpha\beta}(\delta_{\alpha\beta} - \kappa_\alpha\kappa_\beta)\Re(\langle J_\alpha \rangle \langle J_\beta \rangle^*) \\ &\times \sum_\tau \frac{1}{4}(1 + \delta_{\boldsymbol{Q},\boldsymbol{0}}) \left[\delta(\boldsymbol{\tau} + \boldsymbol{Q} - \boldsymbol{\kappa}) + \delta(\boldsymbol{\tau} - \boldsymbol{Q} - \boldsymbol{\kappa})\right].\end{aligned} \tag{4.23}$$

This can be interpreted as magnetic Bragg peaks located $\pm\boldsymbol{Q}$ around each reciprocal lattice vector. The location of the Bragg peaks in the reciprocal hl-plane is illustrated in figure 4.1. The large circles are the nuclear peaks and the smaller the surrounding magnetic satellites. Notice, that the $(0, 0, 1)$ and $(0, 0, 1 - Q)$ peaks are not allowed due to the geometric structure factor.

For *non-Bravais lattices* with p atoms per unit cell, the spins are given by $\langle \boldsymbol{J}_{\boldsymbol{ld}} \rangle = \Re(\langle \boldsymbol{J}_{\boldsymbol{d}} \rangle e^{i\boldsymbol{Q}\cdot\boldsymbol{R}_{\boldsymbol{ld}}})$. The summation over lattice points is split according to $\boldsymbol{R}_{\boldsymbol{ld}} = \boldsymbol{l} + \boldsymbol{d}$, where $\boldsymbol{l}$ is the position of the unit cell and $\boldsymbol{d}$ is the relative position within the unit cell. The sum over unit cells gives the previous obtained δ-functions, whereas the sum over atoms in the unit cell gives the *magnetic structure factor* $F_{M\alpha}(\boldsymbol{\tau}) = |\langle J_\alpha \rangle|^{-1} \sum_{\boldsymbol{d}} \langle J_{\boldsymbol{d}\alpha} \rangle e^{-i\boldsymbol{\tau}\cdot\boldsymbol{d}}$. If the ordering is independent of the sites in the unit cell the magnetic structure factor reduces to the geometric structure factor $F_G(\boldsymbol{\kappa}) = \sum_{\boldsymbol{d}} e^{-i\boldsymbol{\kappa}\cdot\boldsymbol{d}}$.

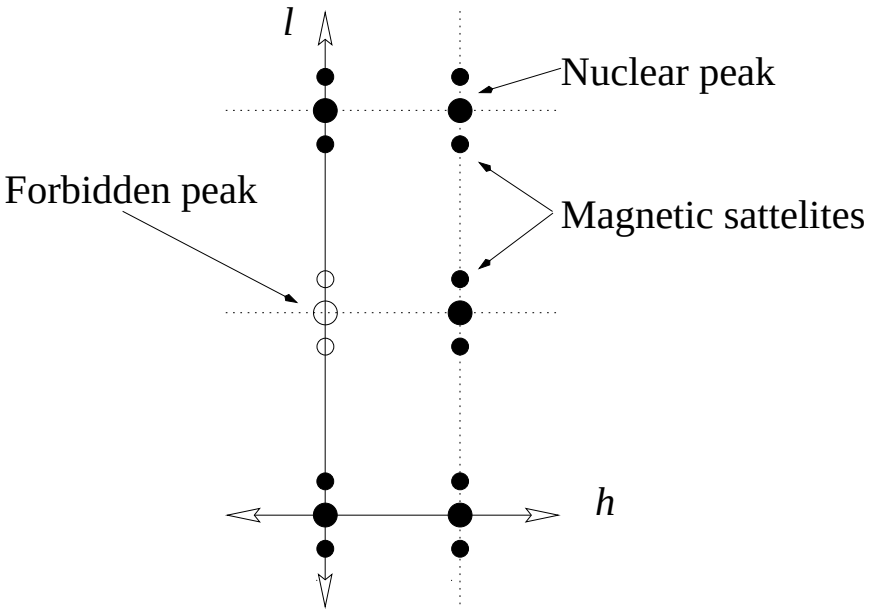

Figure 4.1: Bragg peaks in reciprocal space from a c-axis periodic structure.

$$\begin{aligned}\frac{d\sigma}{d\Omega} =& \frac{8\pi^3 N}{v_0}\left(\frac{\hbar\gamma e^2}{mc^2}\right)^2 e^{-2W(\kappa)}|\tfrac{1}{2}gF(\boldsymbol{\kappa})|^2 \\ &\times \sum_{\alpha\beta}(\delta_{\alpha\beta}-\kappa_\alpha\kappa_\beta)|\langle J_\alpha\rangle\langle J_\beta\rangle|\frac{1}{4}(1+\delta_{\boldsymbol{Q},\mathbf{0}}) \\ &\times \sum_{\boldsymbol{\tau}}\Re\{F_{M\alpha}(\boldsymbol{\tau})F^*_{M\beta}(\boldsymbol{\tau})\}(\delta(\boldsymbol{\tau}+\boldsymbol{Q}-\boldsymbol{\kappa})+\delta(\boldsymbol{\tau}-\boldsymbol{Q}-\boldsymbol{\kappa})).\end{aligned} \tag{4.24}$$

Scattering from m/N structure

In a m/N structure with periodic boundary conditions each commensurate period is denoted n and the unit cell individual unit cell within this period m', so that $j=\{n,m'\}$, $\boldsymbol{J}_j=\boldsymbol{J}_{m'}$ and $\boldsymbol{R}_j=\boldsymbol{R}_{m'}+nN\boldsymbol{R}$. Again the sum is split:

$$\sum_j e^{i\boldsymbol{\kappa}\cdot\boldsymbol{R}_j}\boldsymbol{J}_j=\sum_n e^{in\boldsymbol{\kappa}\cdot N\boldsymbol{R}}\sum_{m'}e^{i\boldsymbol{\kappa}\cdot\boldsymbol{R}_{m'}}\boldsymbol{J}_{m'}=\sum_{\boldsymbol{\tau}}\delta(\boldsymbol{\tau}-N\boldsymbol{\kappa})\sum_{m'}e^{i\boldsymbol{\kappa}\cdot\boldsymbol{R}_{m'}}\boldsymbol{J}_{m'}. \tag{4.25}$$

The first term results in N discrete peaks per reciprocal lattice unit. For each of these peaks the last term is summed to give the amplitude.

Scattering form spin slip structure

Rather than building a finite m/N structure and calculating the scattering cross-section it would be preferable to obtain an expression for the scattering from a distorted basal structure as for instance the *spin slip* structures. For such a structure characterized by just one length b between the spin slips and a *bunching angle* θ it is possible to obtain an expression for the intensity of the peaks along $[0, 0, l]$:

$$I(\boldsymbol{\kappa}) = 2J^2\sigma^2 F(\boldsymbol{\kappa})^2(1+(-1)^I)e^{-(\sigma\sin\alpha)^2}\left|1+\frac{2\sin B\alpha}{\sin\alpha}\cos((B+1)\alpha+\theta)\right|^2, \tag{4.26}$$

where $B = (b-1)/2$, $\alpha = \pi(1/6+I)/b$, σ expresses the fluctuations in b and θ. The integer $I = 6b(\kappa - Q)$ selects the Bragg peaks, $I = 0$ corresponds to the main magnetic peak, $I = -1$ is the fifth harmonic (Cowley and Bates 1988).

However, even this quite complicated expression is only valid for a single (odd) $b \neq 6n-1$. There is therefore not more insight gained in using equation 4.26 rather than the general scattering from a m/N structure.

Another very simple analytic result is obtained for the structure expansion $\phi = u + \gamma\sin u$ introduced in section 2.4.4. Using the expansion $e^{i\phi} \simeq e^{iu} + \frac{\gamma}{2}(e^{i7u} - e^{i5u})$ it is readily seen, that the relative amplitude of the fifth harmonics should be $\gamma^2/4$.

Scattering from a random alloy

The magnetic scattering from a random alloy can be treated in a similar fashion to the isotopic formulation for nuclear scattering. The magnetic scattering length is then put equal to:

$$b_i^\xi = c_i^\xi \frac{\hbar\gamma e^2}{mc^2}\tfrac{1}{2}g_\xi F_\xi(\boldsymbol{\kappa})(\boldsymbol{J}_i^\xi - \hat{\boldsymbol{\kappa}}(\boldsymbol{J}_i^\xi\cdot\hat{\boldsymbol{\kappa}})), \tag{4.27}$$

where $c_i^\xi = 1$ if site i contains an atom from the element ξ (the notation is inconsistent with respect to some literature (Squires 1978)). As for nuclear scattering the distribution c_i^ξ is approximated by the composition average c^ξ. The averaged scattering length: $\bar{b}$ determines the coherent scattering, whereas the incoherent scattering plays no interest in the experiments performed. Thus for the alloy the previous results should be modified by replacing

$$\tfrac{1}{2}gF(\boldsymbol{\kappa})\hat{\boldsymbol{\kappa}}\times\boldsymbol{J}_i\times\hat{\boldsymbol{\kappa}} = \sum_\xi c_\xi \tfrac{1}{2}g_\xi F_\xi(\boldsymbol{\kappa})\hat{\boldsymbol{\kappa}}\times\boldsymbol{J}_i^\xi\times\hat{\boldsymbol{\kappa}}. \tag{4.28}$$

In other words, the coherent magnetic scattering from a random alloy is obtained by averaging the amplitudes before squaring to get the intensities.

The structure expansion parameter γ should be calculated for each of the two elements and then averaged, before squaring to get the relative amplitude of the fifth harmonics in the alloys.

4.1.4 Inelastic scattering

The existence of an elementary excitation with energy $\hbar\omega(q)$ results in a pole in the generalized susceptibility. The absorptive part $\chi''_{\alpha\beta}$ and hence the scattering cross-section will have a peak for each pole. Thus a measurement of the inelastic scattering is a direct measurement of the dispersion relation for quasi particles such as spin waves.

In theoretical calculations the dispersion relation is calculated through the generalized susceptibility, and it is therefore possible to perform a direct comparison with experiments, not only by comparing the dispersion relation but also the amplitude or possibility for such excitations.

If the imaginary infinitesimal in the definition $\chi(\omega) = \lim_{\epsilon\to 0^+} \chi(\omega + i\epsilon)$ is kept finite, it can be interpreted as the experimental energy resolution, hence modifying the calculated scattering from a series of delta functions in $E(k)$ into a scan with finite size peaks.

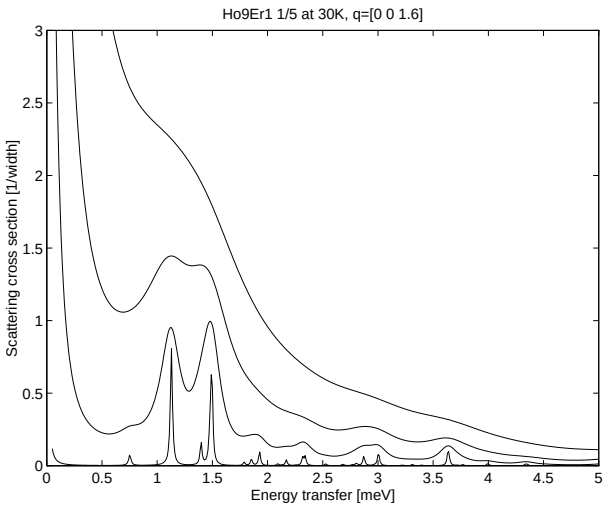

Figure 4.2: Calculated inelastic scattering from a $Ho_{90}Er_{10}$ 1/5 structure at 30 K with ϵ = 0.01 meV, 0.1 meV, 0.25 meV and 0.5 meV. For graphical reasons the scattering is scaled with ϵ.

4.2 Spectrometer

As described above an ideal scattering experiment consists of a measurement of the scattering cross-section (outgoing flux per incoming flux) at different incoming $\boldsymbol{k}$ and outgoing $\boldsymbol{k}'$ wave vectors measured relative to the sample. Except for the k'/k factor all the dependency can be expressed through the energy $\hbar\omega = \hbar^2 k'^2 - \hbar^2 k^2$ and the wave vector transfer $\boldsymbol{\kappa} = \boldsymbol{k}' - \boldsymbol{k} = (h, k, l)$.

A spectrometer is in principle a setup supplying an incoming beam with wave vector $\boldsymbol{k}$ and measuring the outgoing intensity with wave vector $\boldsymbol{k}'$. Since $\boldsymbol{k}$ and $\boldsymbol{k}'$ represent 6 degrees of freedom, a general unrestricted spectrometer should contain the same number.

The simplest way to consider the situation is to fix the sample. Then $\boldsymbol{k}$ and $\boldsymbol{k}'$ are determined by their length and two angles. If the scattering is restricted to a reciprocal plane $\boldsymbol{\tau}_\perp$ of the crystal, only one angle is needed for each $\boldsymbol{k}$ and $\boldsymbol{k}'$. In practice however it is not possible to move the source (a research reactor in this case) and hence the direction of $\boldsymbol{k}$ in real space is not a free parameter. Instead one rotates the sample around $\boldsymbol{\tau}_\perp$, the angle of this rotation is called ω (OM). The direction of $\boldsymbol{k}'$ is then measured with respect to $\boldsymbol{k}$ and is denoted 2θ (2T). The reason for the factor of 2 is, that if only the length of $\boldsymbol{\kappa}$ is to be changed the angles should be moved as $\omega = \theta$. Since two angles are defined around the axis $\boldsymbol{\tau}_\perp$ it is a kind of double axis.

The length and hence the energy of $\boldsymbol{k}$ and $\boldsymbol{k}'$ respectively are defined using Bragg reflection in a monochromator and an analyser crystal. The white beam of thermal/cold neutrons emitted from the source is imposed on a known crystal (pyrolytic graphite in this case). The sample is then placed with an angle of $2\theta_M$ with respect to the white beam. By rotating the monochromator crystal $\omega_M = \theta_M$ just like for the sample, a Bragg peak at $\boldsymbol{\tau}_M = (0, 0, 2)$ can be selected, and hence k is determined by Bragg's law to be $k = n\frac{\tau_M}{2\sin\theta_M}$.

The higher reflections can be removed by filtering. The wave length of the first Bragg peak of a Be powder corresponds to 4.9 meV, and hence neutrons with energies above that will be scattered out of the beam.

Although two angles are used for monochromating they are not independent (once the Bragg peak $\boldsymbol{\tau}_M$ is chosen) and they only determine the length of $\boldsymbol{k}$. The analyser operates in the same manner. The scattered beam is analyzed through an analyser crystal using $\boldsymbol{\tau}_A$. The detector is placed with an angle θ_A with respect to $\boldsymbol{k}'$ and the crystal is oriented by $\omega_A = \theta_A$.

The setup described is called a triple axis spectrometer (TAS). Since the sample axis is a "double" axis, the TAS allows for 4 degrees of freedom. The two missing degrees of freedom determines which reciprocal plane of the sample is to be investigated. They can be restored by a goniometer which rotates the sample around the two axes perpendicular to the sample axis $\boldsymbol{\tau}_\perp$.

Figure 4.3: Schematic illustration of a Triple Axis Spectrometer.

4.3 Data correction

The scattering theory as presented above is also known as kinematic scattering theory. It dealt with one incident neutron and just multiplied by the incident intensity.

The incident beam of neutrons will change within the crystal giving rise to what can be seen as corrections to the kinematical results. This is called dynamical scattering theory.

Instead of comparing calculated scattering directly with the real dynamic scattering it is often used to correct the data. Thus the experimental data are transformed to what they would be if the kinematic results were valid.

4.3.1 Extinction and absorption

There exist different sources of corrections. Perhaps the most readily understandable is the absorption of neutrons which then prevents them from contributing to the scattering cross-section.

But even without absorption the fact that the beam is reduced with the scattered neutrons, result in a correction to the kinetic theory. This is called

primary extinction.

If the crystal consists of domains, the primary extinction will be relieved, since the Bragg peak is now taken from different parts of the incoming beam. However, when the beam passes a domain with an orientation already encountered secondary extinction will occur.

Depending on the shape of the sample, each reflection will have a different effective propagation length through the crystal. Therefore the extinction and absorption effects will change the relative amplitudes of the Bragg peaks.

4.3.2 Resolution of a TAS in elastic scattering

Apart from the sample specific dynamical scattering corrections to the ideal delta-function Bragg peaks from kinematic scattering theory, the resolution of the spectrometer must be taken into account. For various reasons the detector will receive neutrons which have not followed the desired $\boldsymbol{k}$ to $\boldsymbol{k}'$ path. The result upon scattering from a single delta-function Bragg peak $\frac{d\sigma}{d\Omega dE} = \delta(\boldsymbol{q} - q_0)$ will be a finite peak described by the resolution function $R(\boldsymbol{q}, q_0)$. The form of the resolution function can vary as a function of the Bragg position $\boldsymbol{q}_0$. The generalized Gaussian resolution function has the form (Cooper and Nathans 1967):

$$R(\boldsymbol{Q}, \boldsymbol{Q}_0) = N(\boldsymbol{Q}_0) e^{-\frac{1}{2}\boldsymbol{\Delta Q} \boldsymbol{M} \boldsymbol{\Delta Q}}, \tag{4.29}$$

where $\boldsymbol{Q} = \{\boldsymbol{q}, \omega\}$ and $\boldsymbol{\Delta Q} = \boldsymbol{Q} - \boldsymbol{Q}_0$.

In the general space $\{\boldsymbol{q}, \omega\}$ the resolution function is described by scattering ellipsoids representing points of equal intensity. But if the scattering is constrained to elastic scattering along a single direction, it is sufficient to specify two numbers for a given point $\boldsymbol{q}_0$:

- The amplitude (or normalization factor (Chesser and Axe 1972)) $N = \frac{C}{A \sin 2\theta_S}$ affects the relative amplitudes of the peaks positioned at different $\boldsymbol{q}_0$. C is a constant, A a relatively slow varying function and $2\theta_S$ is the angle of the incoming beam $\boldsymbol{k}$ to the out going $\boldsymbol{k}'$. The main variation $1/\sin 2\theta_S$ is called the *Lorenz factor*.

- The longitudinal Gaussian width of the peaks is represented by the matrix $\boldsymbol{M}$ which relates to the width as $\boldsymbol{M}^{-\frac{1}{2}}$. Figure 4.4 shows the width for the two types of scans reported is this work.

For accurate interpretations of scans with relatively few peaks (i.e. simple structures) the integrated intensity of each peak can be corrected properly. But in a scan with inter peak distances less than the Gaussian width the peaks will overlap hence mutually enhance each other. In its extreme consequence a dense distribution of peaks can form one broad peak.

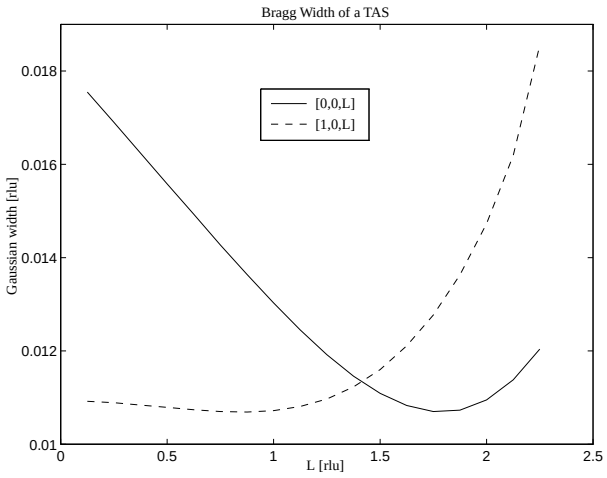

Figure 4.4: Longitudinal Gaussian width of the resolution function for the TAS.

4.4 Samples

Measurements have been performed on two $Ho_{90}Er_{10}$ and two $Ho_{50}Er_{50}$ crystals:

1. $25mm^3$ $Ho_{90}Er_{10}$ used in most of the scans.
2. $500mm^3$ $Ho_{90}Er_{10}$ used for inelastic scattering and a few comparative scans.
3. $5mm^3$ $Ho_{50}Er_{50}$ used in most of the scans.
4. $2mm^3$ $Ho_{50}Er_{50}$ used to verify data from sample 3.

All samples were random alloys cut from larger single crystals grown by the strained annealing method at AMES Lab, USA. The volumes of the three samples used for elastic measurements were small enough to exclude multiple scattering. The $Ho_{50}Er_{50}$ sample however showed some mosaic spread in the $[1, 0, l]$ scans but not in the $[0, 0, l]$ scans, hence the spread was in the *ab*-plane. The samples were mounted in a helium filled aluminium can and placed inside a displex, which in turn was mounted on the sample goniometer of the spectrometer. Unfortunately the exact origin and history of the samples is unknown. Hence the $Ho_{50}Er_{50}$ crystals, which seem to be the fractions of one rectangular crystal, could be the same as the one investigated earlier by (Howard and Bohr 1991, Pengra *et al.* 1994). The unidentified intermediate phase discussed in section 5.3.2 could therefore be a crystal specific phenomena.

The samples were aligned for scattering in the *ac*-plane using the $(1, 0, 0)$ and the $(0, 0, 2)$ Bragg peaks. The absolute position of these were also used to determine the crystal parameters as given in table 4.2. It is seen, that the alloys show lattice parameters consistently though very little larger than both of the elements, but this is believed to be a question of spectrometer alignment rather than a physical feature.

[Å]	Ho	$Ho_{90}Er_{10}$	$Ho_{50}Er_{50}$	Er
a	3.578	3.564	3.560	3.559
c	5.618	5.630	5.618	5.585
$\sqrt{3/8}c/a$	0.962	0.967	0.966	0.961

Table 4.2: Crystal parameters for Ho, Er and the alloys.

4.5 Scans

The elastic scattering results can be summarized in different types:

- Long $[h, k, l]$ scans varying l, hence revealing all the higher harmonics within the interval. However, these scans are a compromise between step size $\Delta L \sim c^*/200$, counting statistics > 10 and scanning time $\sim 4 - 10$ hours. Therefore long scans have only been performed at a rather coarse temperature stepping. The long scans can be fitted to the calculated scattering thus testing the theoretically predicted structures.

- A single Bragg peak can be studied by performing two perpendicular scans thereby finding the middle of the peak. These scans are fairly quick and can therefore be performed for several peaks at a number of temperatures. A series of single peak scans follows the position, width and amplitude of the peak as a function of temperature.

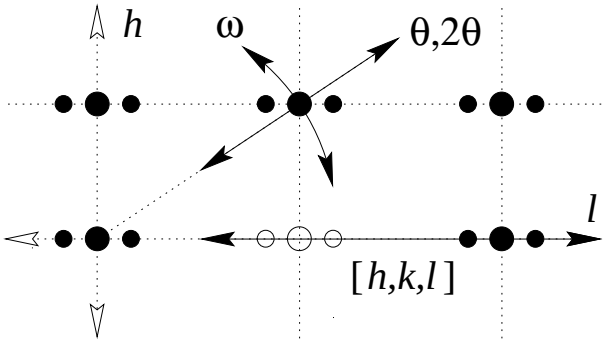

Figure 4.5: The scan in reciprocal space

The scans move along different lines in reciprocal space as illustrated in figure 4.5. The long scans are parallel to the l direction. The single peak scans consists of the two subsequent scans ω and $\theta, 2\theta$. The ω scan moves along a circle in the hl-plane, whereas the $\theta, 2\theta$ scan moves in a straight radial line.

Chapter 5

Results — alloy features

The experimental data can be summarized as:

$Ho_{90}Er_{10}$
- $[0, 0, 0.8 \rightarrow 2.1]$ and $[1, 0, -0.05 \rightarrow 1.05]$ scans at $T = 10$ K–100 K
- One-peak scans of $(1, 0, 0)$ and $(0, 0, 2 - Q)$
- Few inelastic scans at $(0, 0, l)$ points with $0 < \omega < 2$ meV

$Ho_{50}Er_{50}$
- $[0, 0, 0.8 \rightarrow 2.1]$ and $[1, 0, -0.05 \rightarrow 1.05]$ scans at $T = 10$ K–70 K
- One-peak scans of $(1, 0, 0)$, $(1, 0, Q)$, $(0, 0, 2 - Q)$ and $(0, 0, 2)$

The long scans can be used in two ways. Though coarse in temperature the peaks present can be mapped as in a one-peak scan, giving more points in the temperature dependence of the peaks. Secondly, the scans can be fitted directly to the calculated scattering from a calculated structure, hence comparing not only the peaks present in the scan but also exploring the possibility of unwanted additional peaks from a wrong guess of structure. Since the long scans contain all the higher harmonics, they supply information on the details of the structure, which in hand sheds light on the types and strengths of the interactions in the system.

Rather than basing the comparison between theory and experiment on the types of data or the types of calculations, each feature of the systems will be presented accompanied by the appropriate experimental and calculational results.

5.1 Common features

The features can be split into two groups — the common features which only differ quantitatively and the qualitatively different features, which are unique for each of the alloys.

As expected both samples showed an overall behaviour similar to Ho, starting with a basal plane *helix* at T_N and ending in a cone structure in the limit of

zero temperature. Of course the numbers characterizing the two phases (T_N, T_C, $Q(T)$, θ_{bunch} etc.) are different for each system. But on the other hand both alloys showed some interesting novel features such as a disordered state at low temperatures in $Ho_{90}Er_{10}$ and an intermediate phase in $Ho_{50}Er_{50}$.

5.1.1 Magnetic onset — T_N

The onset of magnetic ordering is characterized by the Néel temperature T_N, where both alloys develop a helix structure. Figure 5.1 shows the measured intensities of the main magnetic peak $(0, 0, 2 - Q)$ for the two crystals.

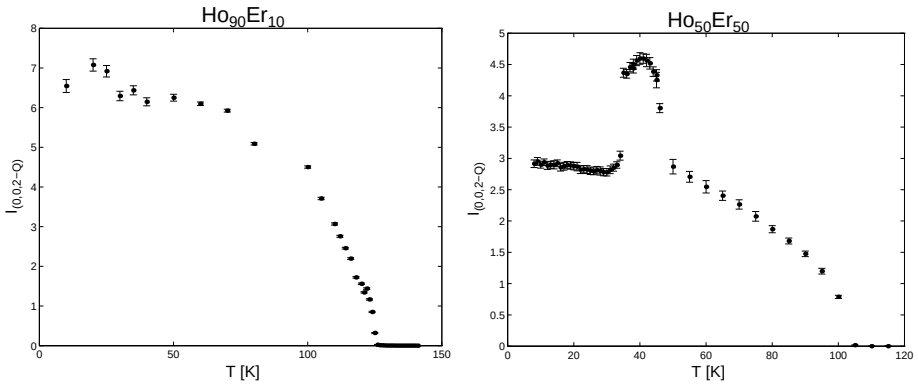

Figure 5.1: Intensities of the main magnetic peak $(0, 0, 2 - Q)$ for each of the two alloys.

The experimental transition temperatures deduced from figure 5.1 can be compared to a scaling of the known transition temperatures for the elements or to mean-field calculations of the transition as summarized in table 5.1.

T_N[K]	Experiment	Scaling	MF	Magnetization
Ho	133		132	131
$Ho_{90}Er_{10}$	125	128	126	126
$Ho_{50}Er_{50}$	104	109	105	106
Er	85		84	84

Table 5.1: The Néel temperature for magnetic ordering

The transition temperatures for the alloys are close to the simple weighted averages. Since all MF theories have a critical order parameter exponent of $\frac{1}{2}$ and the scattering intensity is proportional to $|\langle J \rangle|^2$ the MF calculations predict a linear rise in $I_{(0,0,2-Q)}$ which is clearly not the case. However, the predicted transition temperatures agree with the measured within the experimental error. The exchange parameters of the elements are determined paying respect to the

transition temperature which is therefore built into the model. But the data for the alloys shows that the scaled electron gas assumption does not lead to wrong transition temperatures.

In general mean-field theories are known to be inadequate in the vicinity of phase transitions, but the long range nature of the interactions in the three (as opposed to lower) dimensional rare earth systems ensures the unexpectedly good agreement of the transition temperatures T_N.

At zero temperature, the thermal expectation values $\langle \boldsymbol{J}_i \rangle$ becomes equal to the ground state expectation value, the direction of which can be chosen as the z-axis. Hence all of the moments will have their full length J at zero temperature and the order parameter is $\sigma = 1$. The saturation value of the magnetic peak $(0, 0, 2)$ must therefore correspond to this totally ordered state.

Theoretically, the saturation value for the magnetic peak should be:

$$\frac{I_{(0,0,2-Q)}}{I_{(0,0,2)}} = \frac{1}{4b^2} \left(\frac{\hbar \gamma e^2}{mc^2} \right)^2 \left\{ \tfrac{1}{2} g F \right\}^2 J^2, \tag{5.1}$$

assuming the structure to be totally ordered ($\sigma = 1$). The measured values are however about 40% to low, which must be explained in terms of extinction and absorption effects.

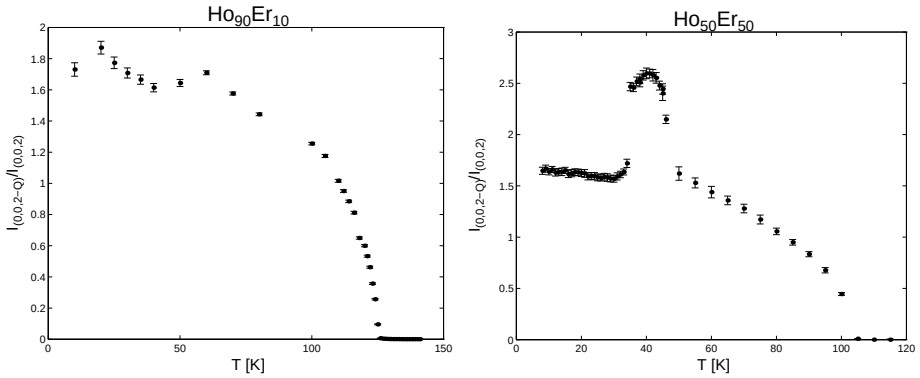

Figure 5.2: Relative intensities of the main magnetic peak $(0, 0, 2 - Q)$ for each of the two alloys.

5.1.2 Cone phase — T_C and cone angle

Both Ho and Er develops a ferromagnetic component in the c direction at $T_C =$ 20 K and 18 K respectively, while the basal plane component forms a helix. The *cone* phase is characterized by the transition temperature T_C and the *cone angle* $\sin\theta = \langle J_z \rangle / \langle J \rangle$ of the cone to the basal plane in the limit of zero temperature.

Since the geometric selection rules for magnetic neutron scattering requires the wave vector transfer to be perpendicular to the moments, the cone phase will

cause scattering in the basal plane, and since it is a constant c-axis component it corresponds to $Q = 0$ which means, that the magnetic scattering will coincide with the nuclear peaks.

The cone phase can thus be studied from the experimental data by considering the enhancement $I_{(1,0,0)}$ of the nuclear $(1,0,0)$ peak relative to the main magnetic peak $I_{(0,0,2-Q)}$. For the cone phase equation 4.24 gives the following relation between the two peaks of interest:

$$\frac{\langle J_z \rangle}{\langle J_x \rangle} = \frac{F(2-Q)}{F(1)} \sqrt{\frac{I_{(1,0,0)}}{I_{(0,0,2-Q)}}}. \tag{5.2}$$

Thus the cone phase transition can be investigated by scanning $(1,0,0)$ and $(0,0,2-Q)$ as a function of temperature. The relative intensity $(I_{(1,0,0)} - I^{\mathrm{nuc}}_{(1,0,0)})/I_{(0,0,2-Q)}$ Since the magnetic $(1,0,0)$ peak lies on top of the nuclear

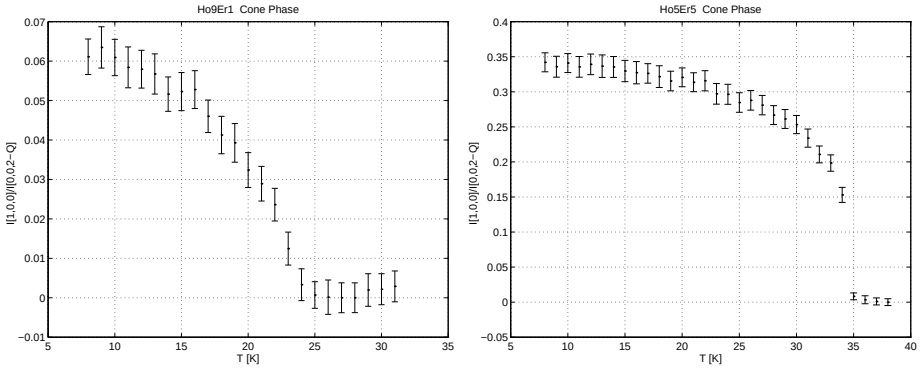

Figure 5.3: The cone phase transition T_C illustrated by $I_{(1,0,0)}$.

$(1,0,0)$ peak it is the enhancement of the peak that corresponds to $I_{(1,0,0)}$. The derivation of the angles is summarized in table 5.2.

	$\frac{F(2-Q)}{F(1)}$	$I_{(1,0,0)}/I_{(0,0,2-Q)}$	θ
$Ho_{90}Er_{10}$	0.945	0.06	13.4°
$Ho_{50}Er_{50}$	0.951	0.33	33.1°

Table 5.2: The numbers leading to the measured cone phases angles

As is seen from figure 5.3 and table 5.3 the cone phase appears at higher temperatures in the alloys than in the two elements. The explanation is to be found in the fact, that Ho enters the cone phase from a flat helix, whereas Er has a *cycloidal* structure above T_C. The reason for that is the difference in signs of B^0_l and especially B^0_2 which for Ho and Er favour respective small and large c-components. In the alloys the Ho moments will not form a cycloidal

	Ho	$Ho_{90}Er_{10}$	$Ho_{50}Er_{50}$	Er
T_C	20 K	24 K	35 K	18 K
T_C MF	21 K	unstable	10 K	meta-stable
Cone angle θ	10°	13.4°	33.1°	60°
θ MF	10.4°	–	32°	62°
Magnetization	13°	17°	37°	60°

Table 5.3: Cone phase transition temperature T_C and maximum cone angle θ.

structure and induces a helix but the out of plane attraction for Er shifts T_C for the cone phase upwards. Another explanation for the rise in T_C at intermediate compositions of Ho and Er is that the cone gives the two kind of moments a better chance to align slightly differently than is possible in the flat helix. The data is in good agreement with earlier magnetization measurements (Bozorth *et al.* 1972).

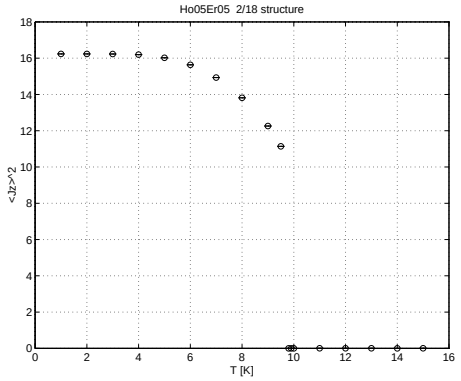

Figure 5.4: The cone phase transition T_C in $Ho_{50}Er_{50}$ calculated by mean field.

The success of MF calculations is limited with respect to the cone phase (5.4). Since for the pure elements the model coincides with those of (Jensen 1996a) and (Cowley and Jensen 1992) both T_C and θ are very well described in holmium.

In the case of erbium the cone phase turns out to be meta-stable which means, that the MF iterations converge both to a cone phase and a helix depending on the starting structure. However, the cone phase has approximately 1 meV higher free energy. Hence T_C cannot be predicted for erbium. Surprisingly (or perhaps accidentally) the VC–MF model works best for the $Ho_{50}Er_{50}$ case. The cone angle of $\theta_{\mathrm{MF}} = 33°$ agrees within the standard deviation of the experimental data. However, as is seen in figure 5.4 the transition temperature $T_{C\mathrm{MF}} = 10$ K is in direct contradiction for the tendency of higher T_C for the alloys.

In $Ho_{90}Er_{10}$ the cone phase is unstable upon iteration at all temperatures.

When iterated, a starting cone structure will decay into a helical structure with no or very little ferromagnetic component but with oscillations in the c-axis (figure 5.5).

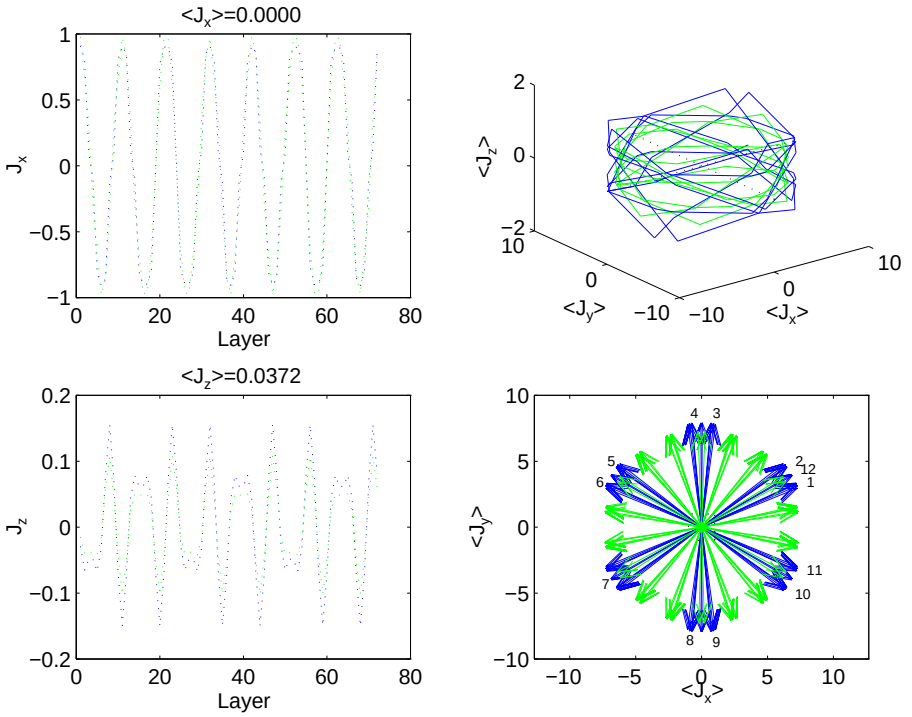

Figure 5.5: The converged 7/36 structure in $Ho_{90}Er_{10}$ at 1 K, Ho moments are blue, Er moments green.

The simplest and most transparent way to adjust the model to predict the right cone angle is by imposing an external field. In a field of 7.5 kOe in the c-direction the *Zeeman* term ensures the right cone angle of 13.4°, without disturbing the other interactions in the model. Therefore when fitting the cone phase data this unphysical field is used rather than trying to adjust the other parameters of the model. However, since magnetic scattering only probes the part of $\langle \boldsymbol{J} \rangle$ perpendicular to $\boldsymbol{\kappa}$, the cone phase only appears in the $[1, 0, l]$ scans.

5.1.3 Periodicity — $Q(T)$

The two-ion interactions are the mechanism responsible for the magnetic ordering. Of these the dominant is the *indirect exchange coupling* characterized by the Fourier transform $\mathcal{J}(\boldsymbol{q})$ of the coupling strength. The periodic structures is a consequence of the maximum of $\mathcal{J}(\boldsymbol{q})$ for nonzero $\boldsymbol{Q}_{\mathcal{J}} \parallel \boldsymbol{c}^*$. Except for small

corrections such as lock-in to commensurable periodicities $m\boldsymbol{c}^*/n$ the periodicity of the structures follows $\boldsymbol{Q}_{\mathcal{J}}$ as a function of temperature. The Fourier transformed of $\mathcal{J}(\boldsymbol{q})$ is shown in figure 5.6 for the four cases of interest. The

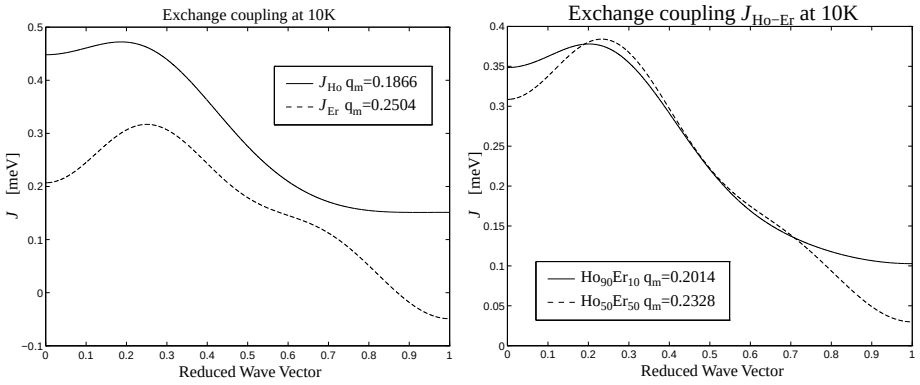

Figure 5.6: $\mathcal{J}(\boldsymbol{q})$ and $Q_{\mathcal{J}}$ for Ho, Er, $Ho_{90}Er_{10}$ and $Ho_{50}Er_{50}$

periodicity of the system as expressed by $\boldsymbol{Q}$ must be the structure with least free energy. Thus $\boldsymbol{Q}_{\mathrm{MF}} = m\boldsymbol{c}^*/N$ can be estimated by minimizing the calculated free energy for varying structures. Such calculated free energies for various structures are shown in figure 5.7.

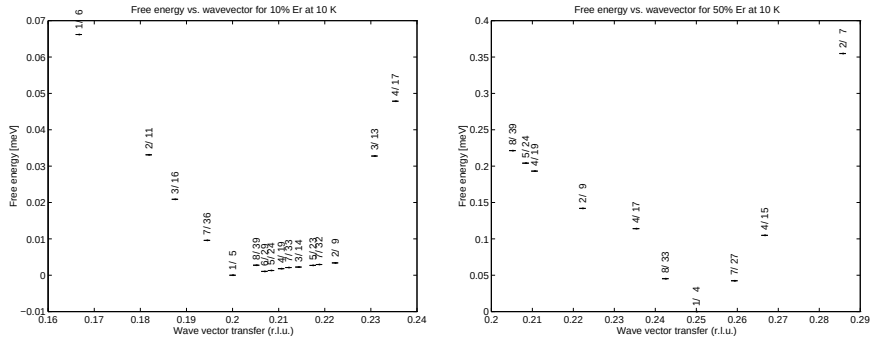

(a) $Ho_{90}Er_{10}$ at 10 K

(b) $Ho_{50}Er_{50}$ at 10 K

Figure 5.7: Calculated free energy for structures with different q

The non-simple form of the free energy and the difference between the minima Q_{MF} and $Q_{\mathcal{J}}$ are both reflecting the other parts of the Hamiltonian.

The main magnetic peaks $\tau \pm Q$ in the ordered phase have cross-sections of the same order as the nuclear cross-section, and are therefore easily and quickly measured with good accuracy. Figure 5.8 shows the periodicities $Q(T)$ as measured and as estimated from $Q_{\mathcal{J}}$ and Q_{MF}.

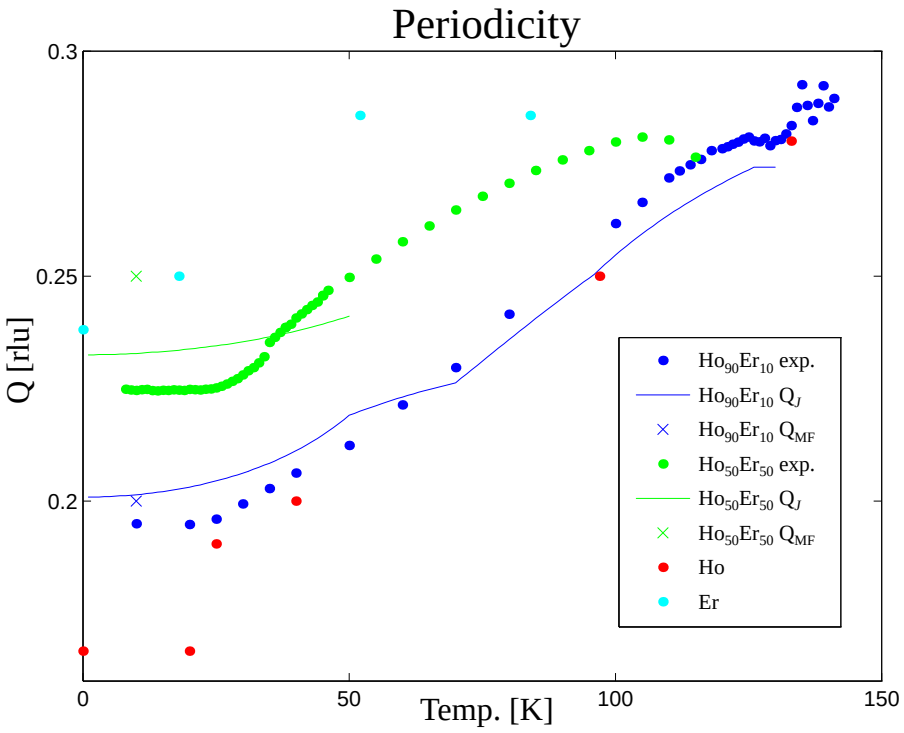

Figure 5.8: $Q(T)$ for $Ho_{90}Er_{10}$ and $Ho_{50}Er_{50}$.

There is a qualitative agreement, but as is seen, the minimum energy calculations cannot be used to find the actual structures of the system, since in that sense there is quite some difference between for instance the 1/5 structure and the modified 7/36 structure used in the fits at 10 K for this alloy. In terms of *spin slips* the two structures are respective (221) and (2221 221). And the scattering from the two structures is also very different. If the discrepancy is measured in units of the difference $Q_{Ho_{90}Er_{10}} - Q_{Ho}$ it is 20 percent. The periodicity Q must therefore be chosen to fit the experiments, but nevertheless the structure calculations are very useful. For instance, the cone phase in Er is only meta-stable according to MF free energy calculations (the basal plane helix is about 1 meV lower), but MF still predicts the right cone angle.

Even though the model does not predict the right Q value, the discrepancy amounts to of 0.01 meV which corresponds to 0.1 K. The very flat energy minimum for $Ho_{90}Er_{10}$ is the reason for the un-relaxed disordered structure observed below 25 K (see section 5.2.2). Although shifted relative to the observed periodicity, the flatness depicts the little energy gained by adjusting the structure to the absolute minimum. On the other hand it does not mean, that the system easily can change the structure. The hexagonal anisotropy constitutes an energy barrier for each spin that crosses a *hard axis*. Without any energetic

motivation and dis-encouraged by the hard axes, the system behaves like a spin glass, which cannot find the absolute minimum among the deep local minima.

Figure 5.8 reflects some interesting features of the temperature dependent exchange coupling:

- All four systems have the same starting periodicity $Q(T_N) \simeq 0.28$. It is this starting periodicity, that is determined by the exchange integral and the form of *Fermi surface*, which both are very similar for all the heavy rare earths.
- As the systems order, the conduction gas is polarized by the magnetic moments, hence distorting the Fermi surface. This polarization is dependent of the size of the moments, and it is seen, that the decrease in periodicity is monotonic with respect to the effective size of the magnetic moment in the alloys as predicted by Koehler *et al.* (1963) and Elliot and Wedgwood (1964).

5.1.4 Anisotropy, bunching angles and fifth harmonics

The *crystal field* and the anisotropic interactions give rise to modifications of the simple structures. These distortions of the structures are reflected by the presence of higher harmonics in the scattering cross-section.

MF calculations on a finite structure $Q_{\mathrm{MF}} = \frac{mc^*}{N}$ can only deal with corrections commensurable to N i.e. integer harmonics of Q_{MF}. But by increasing N keeping $Q_{\mathrm{MF}} \simeq Q_{\mathrm{exp}}$ the number of possible harmonics is increased to a desired level. Through equation 4.23 the scattering cross-section can be evaluated and compared to experimental scans. Such fits will be discussed in section 5.2.1 and 5.3.1. However, they do not directly elucidate the effect of the individual terms in the Hamiltonian. It can therefore be useful to consider the corrections to the pure structures one by one.

The most dominant correction comes from the crystal field term $B_6^6 O_6^6(J)$. As discussed in section 2.2.2, the hexagonal anisotropy can be expressed in terms of *hexants* separated by 6 hard axes resulting in the formation of spin slip structures. This distorted helix or cone structure is to first order of the form $\langle \boldsymbol{J}_i \rangle = J\sigma \cos\theta(\cos\phi_i, \sin\phi_i, \tan\theta)$, where θ is the cone angle and:

$$\phi_i = u_i + \gamma \sin 6u_i,\ u_i = Q \cdot \boldsymbol{R}_i. \tag{5.3}$$

The expansion parameter γ, which is connected to the *bunching angle*, can be estimated in three ways:

- The free energy expansion 2.44 gives an estimate of:

$$\gamma = \frac{12\boldsymbol{\kappa}_6^6}{(J\sigma)^2\{2\mathcal{J}(\boldsymbol{q}) - \mathcal{J}(5Q) - \mathcal{J}(7Q)\}}, \tag{5.4}$$

- The calculated mean-field structures can be fitted to the structure expansion varying γ and u_0, using the mean square residue method.

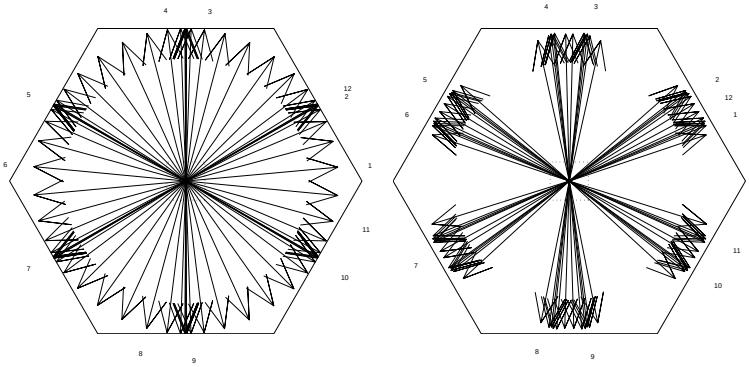

Figure 5.9: The γ-structure and the MF structure

Although the resulting γ is reasonable, there is quite some discrepancy in the actual structures as seen from figure 5.9. The simple low order expansion can of course not contain the complexity of the spin slip structures.

- As mentioned earlier the relative amplitude of the fifth harmonics should be $\gamma^2/4$, from which a direct experimental estimate can be made.

The three different estimates shown in table 5.4 for the two temperatures 10 K and 70 K are seen to be within the same order of magnitude at both temperatures.

T[K]		1.	2.	3.
10	Ho	0.217	0.211	0.2
	$Ho_{90}Er_{10}$	0.186	0.185	0.219
	$Ho_{50}Er_{50}$	0.109	0.125	0.110
	Er	-0.219	-0.249	(-)0.2
50	$Ho_{50}Er_{50}$	0.0253	0.0258	0.0245
70	$Ho_{90}Er_{10}$	0.009	0.010	0.020

Table 5.4: The parameter γ estimated from 1. free energy minimization, 2. fit to MF structure and 3. experiment

The reasonable agreement is quite surprising in the view of two different complications. At low temperatures the *bunching* effect is substantial, and a γ around 0.2 is not a small expansion parameter. At higher temperatures, where the expansion might be expected to be valid, γ is very sensitive to the right value for the ordering parameter.

5.2 $Ho_{90}Er_{10}$

The results of the long scans can be summarized in a 3D plot of the intensity as a function of position and temperature or a plot showing the peak locations at different temperatures (figures 5.10 and 5.11).

Above T_N only the nuclear Bragg peaks $(0,0,2)$, $(1,0,0)$ and $(1,0,1)$ are present. Below T_N the main magnetic peaks $\boldsymbol{\kappa} = \boldsymbol{\tau} \pm \boldsymbol{Q}$ (i.e. $(0,0,2-Q)$, $(1,0,Q)$ and $(1,0,1-Q)$) grows to magnitudes comparable to the nuclear peaks. As the temperature decreases the anisotropic interactions start to modify the pure structure resulting in higher harmonics. The most dominant are the 5'th harmonics $\boldsymbol{\kappa} = \boldsymbol{\tau} \pm 5\boldsymbol{Q}$, which since $Q \sim \frac{1}{5}$ are drowned in the mosaic tails of the nuclear peaks in the $[1,0,l]$ scans. In the $[0,0,l]$ scans the two 5'th harmonics $(0,0,5Q)$ and $(0,0,2-5Q)$ are accompanied by an unexpected peak at $(0,0,1)$, all three developing around 70 K. At 50 K the 7'th harmonics $(0,0,7Q)$, $(1,0,7Q-1)$ and $(1,0,2-7Q)$ appear and finally around 20 K the 11'th and 13'th harmonics $[0,0,4-11Q]$, $(1,0,3-11Q)$, $(0,0,4-13Q)$, $(1,0,3-13Q)$ and $(1,0,13Q-2)$ can be identified. Two third harmonics $(1,0,1-3Q)$ and $(1,0,3Q)$ appears already at 60 K in the $[1,0,l]$ scan, whereas the $(0,0,2-3Q)$ only appears as a faint shoulder to the $(0,0,7Q)$ below 20 K. The $(6n\pm1)Q$ peaks are mainly due to the hexagonal anisotropic crystal field. The 3'rd harmonics are distortions mainly in the c-direction due to the trigonal coupling.

The peak at $(0,0,1)$ is not readily explainable, since the *nuclear structure factor* forbids the peak. The peak can either be magnetic or nuclear of origin. A first guess would be magnetic scattering, since it seems to develop at the same T as the 5'th harmonics, and in that case it would probably be connected to the bunching of the moments. The phenomena could be related to the different *hard axes* in Ho and Er, but it has also been reported in experiments from pure erbium and holmium: Lin *et al.* (1992) draws the conclusion, that the $(0,0,1)$ peak comes from nuclear scattering due to breaking of the *hcp* symmetry induced by magnetostrictive effects. The peak is present in the figures of Cowley and Jensen (1992); In holmium Cowley and Bates (1988) and Bates *et al.* (1988) denotes it to second order scattering, but this cannot be the case. The $(0,0,1)$ reflection corresponds to a distinguishing between the basal plane components of the two planes in the unit cell, which seems implausible.

The temperature independency of the tiny bump at (0,0,1.65) suggests, that it is not from the sample.

Around $l = 1.5$ the $[0,0,l]$ scans show an increase in the background by a factor of 5. This feature which is constant up to 100 K could be a result of shielding problems, but no similar behaviour is seen in the $Ho_{50}Er_{50}$ sample. It could be diffuse scattering due to thermal effects, disordering or stress. The negligible temperature dependency rules out the thermal diffuse scattering, but the presence of 10% Er atoms could very likely cause stress, as well as the randomness is a kind of disorder.

The diffuse scattering is seen as very broad tails around the strong peaks. Along $[1,0,l]$ the tails from $(1,0,0)$ and $(1,0,1)$ overlap, hence producing the flat background seen in the scans along $[1,0,l]$.

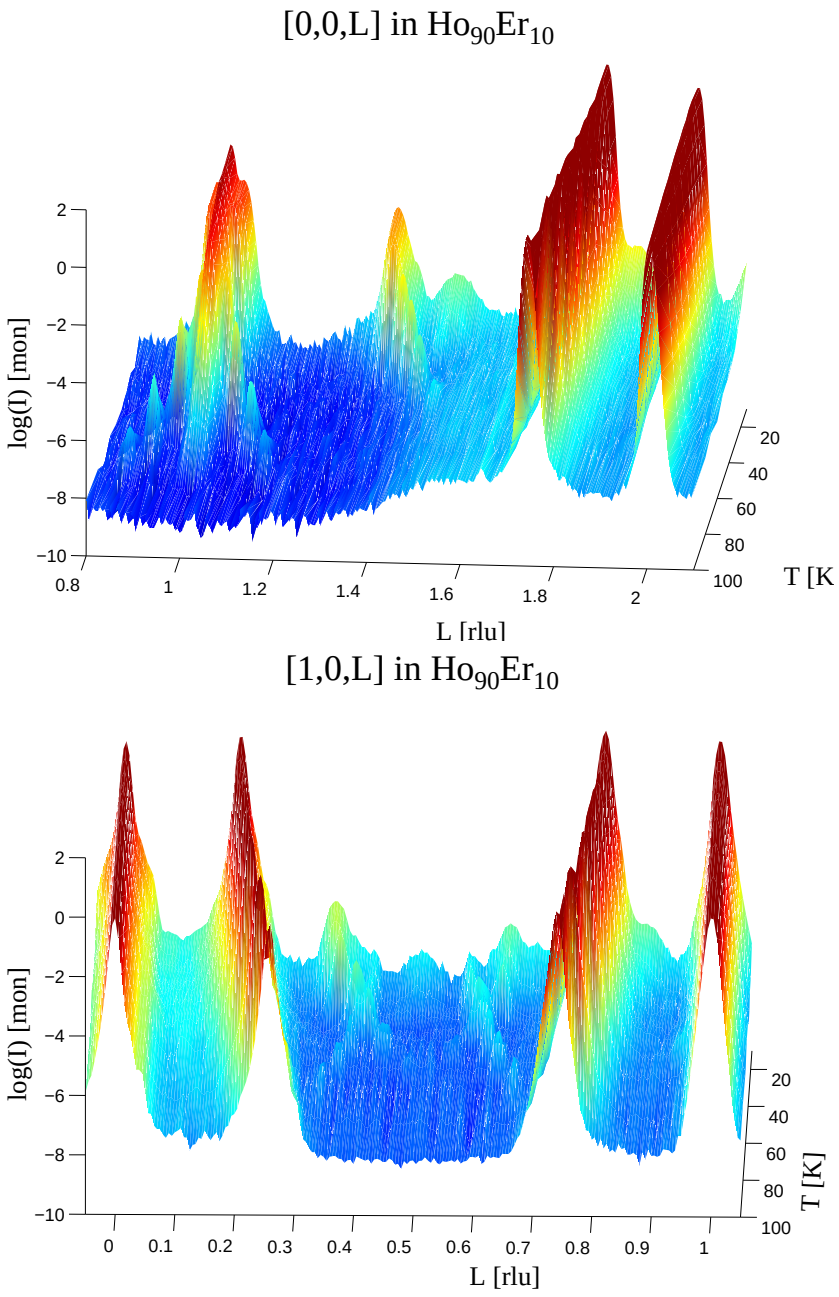

Figure 5.10: Scans in $Ho_{90}Er_{10}$

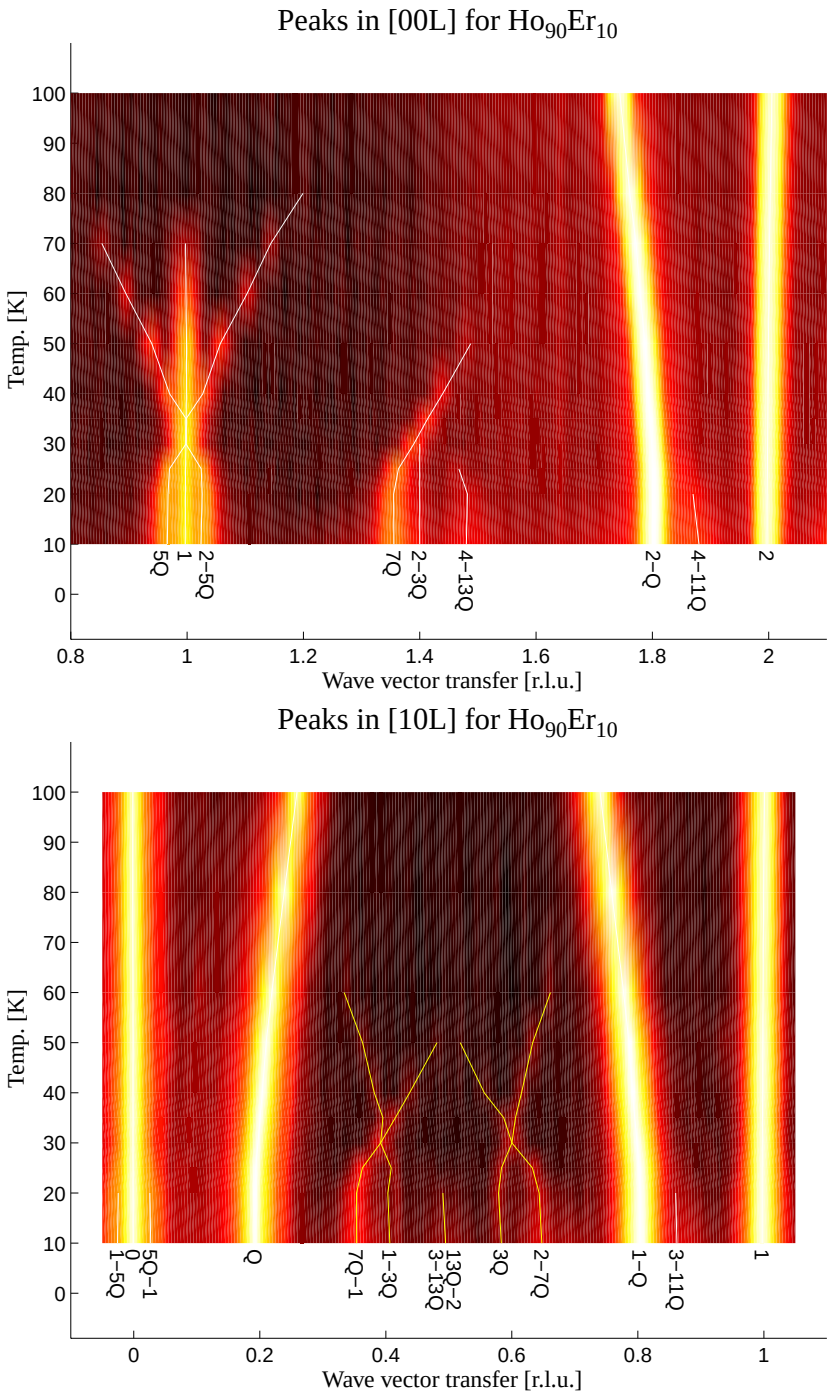

Figure 5.11: Peaks in $Ho_{90}Er_{10}$

5.2.1 Structure fits

Rather than interpreting the long scans in terms of structural parameters, they are compared directly to the calculated scattering from the structures reached by mean-field theory.

$Ho_{90}Er_{10}$ is assumed to order helical just as pure Ho. The starting structure for the mean-field calculations is therefore chosen as a helix with the periodicity $Q_{\mathrm{MF}} = m/N$ close to the measured Q. By design, the mean-field structures are commensurate, but by increasing N keeping the approximately right Q_{MF}, the commensurate effects can be investigated and avoided if they are not present in the data.

The overall magnetic scattering intensity is taken from the main magnetic peak, which is then automatically fitted correctly, since its position determines m/N. The magnetic scattering amplitude could in principle be related to the nuclear amplitude, thereby allowing an estimate of the degree of order given by the ordering parameter $\sigma(T)$. This procedure is however of limited success due to *absorption* and *extinction* effects. A more direct estimate of $\sigma(T)$ relies of the fact, that $\sigma = 1$ in the limit of zero temperature.

The agreement of a such fit is characterized by two things, namely the existence of the right number of peaks, and the position and amplitude of each peak.

Disregarding the $(0, 0, 1)$, peak the calculated structures results in the right number of peaks, which all have the right positions. The positions are determined as multiples of Q, which was chosen by hand, and the agreement in positions is therefore expected.

That the relative amplitudes are in reasonable agreement means that the anisotropic interactions are of the right strengths.

The tendency for the MF scattering to underestimate the $(1, 0, Q)$ peak can be explained by extinction and absorption effects.

5.2.2 Low temperature disordered $7/36$ phase

Below 25 K the $Ho_{90}Er_{10}$ alloy enters a phase with a long range ordering periodicity of $q = 7/36$, but with a short range disorder. The disorder is seen as a broadening of the higher harmonics beyond the widths caused by the experimental resolution. The broadening is most profound along $[0, 0, l]$ at 10 K, and hence the attention is directed to fitting this particular scan.

The widths of the scan is a combination of a broadening due to non-perfect order and the experimental resolution discussed in section 4.3.2. A folding of two different widths will roughly inherit the largest of the two.

Apart from the normalization factor N, the resolution function causes an averaging of the scattering, so that close lying peaks mutually lifts each other on the account of isolated peaks, which decreases in relative amplitude. Eventually close lying peaks can be folded into one broad peak. In the pure $7/36$ structure the minimum separation between the peaks is $1/36 \simeq 0.028 rlu$. With a width of 0.01 as seen in the scans the overlap from peak to peak is around 2%, and

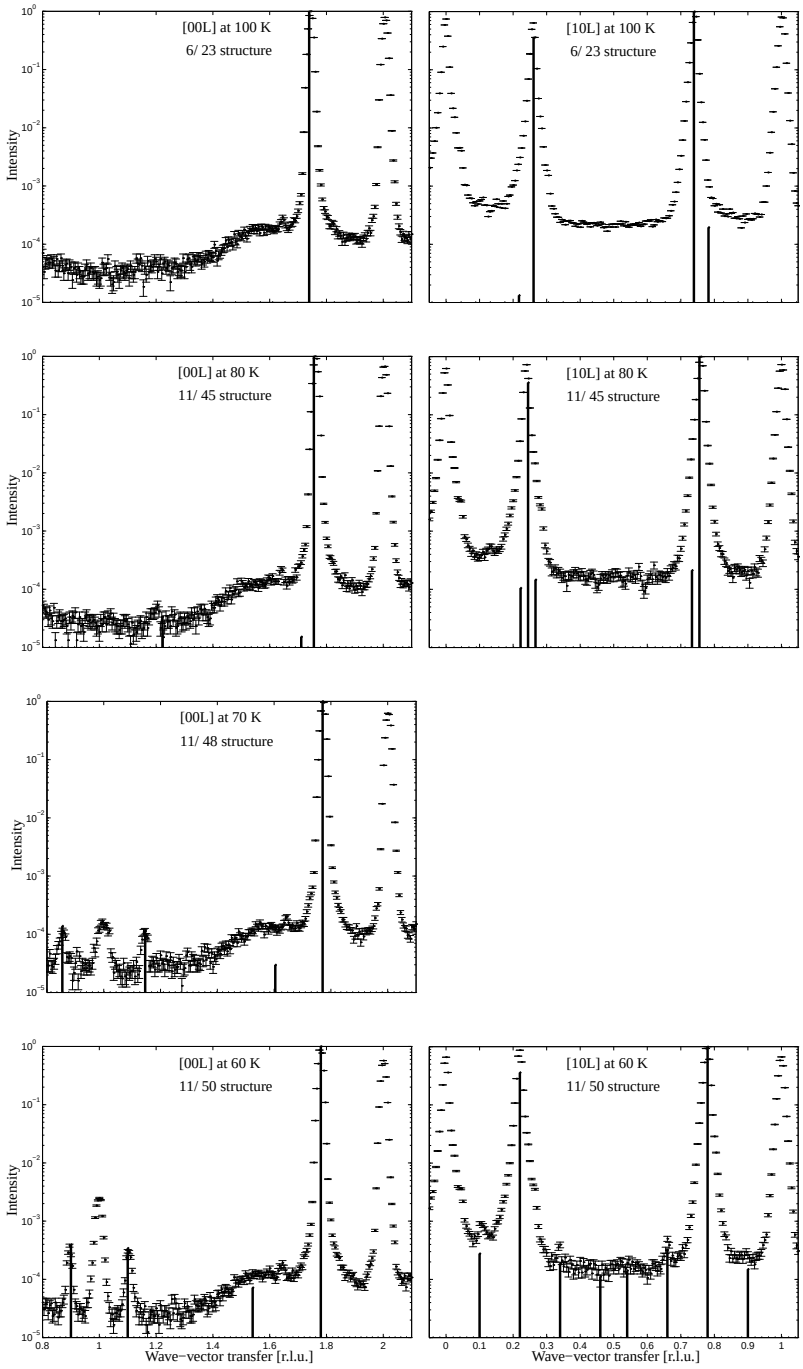

Figure 5.12: Scans from $Ho_{90}Er_{10}$ fitted with MF structures 100 K to 60 K.

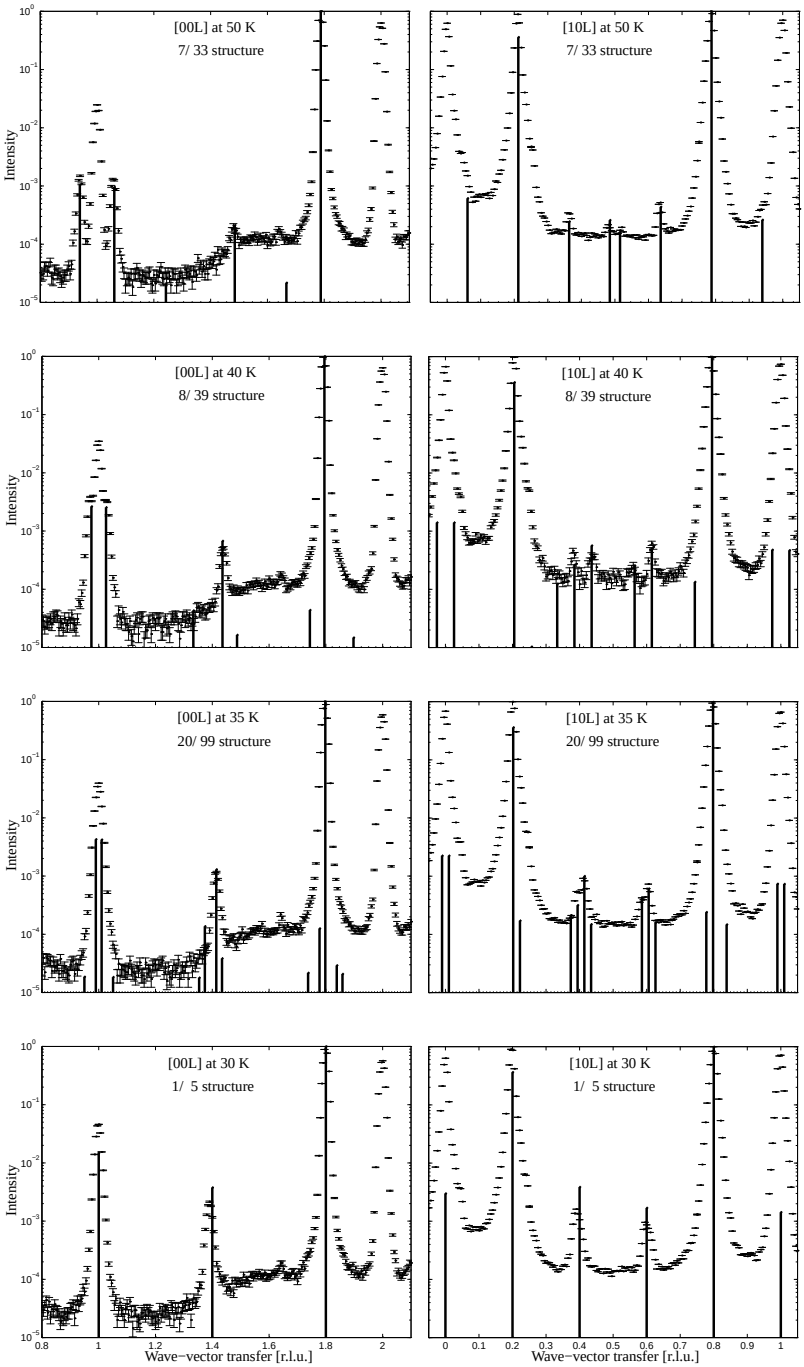

Figure 5.13: Scans from $Ho_{90}Er_{10}$ fitted with MF structures 50 K to 30 K.

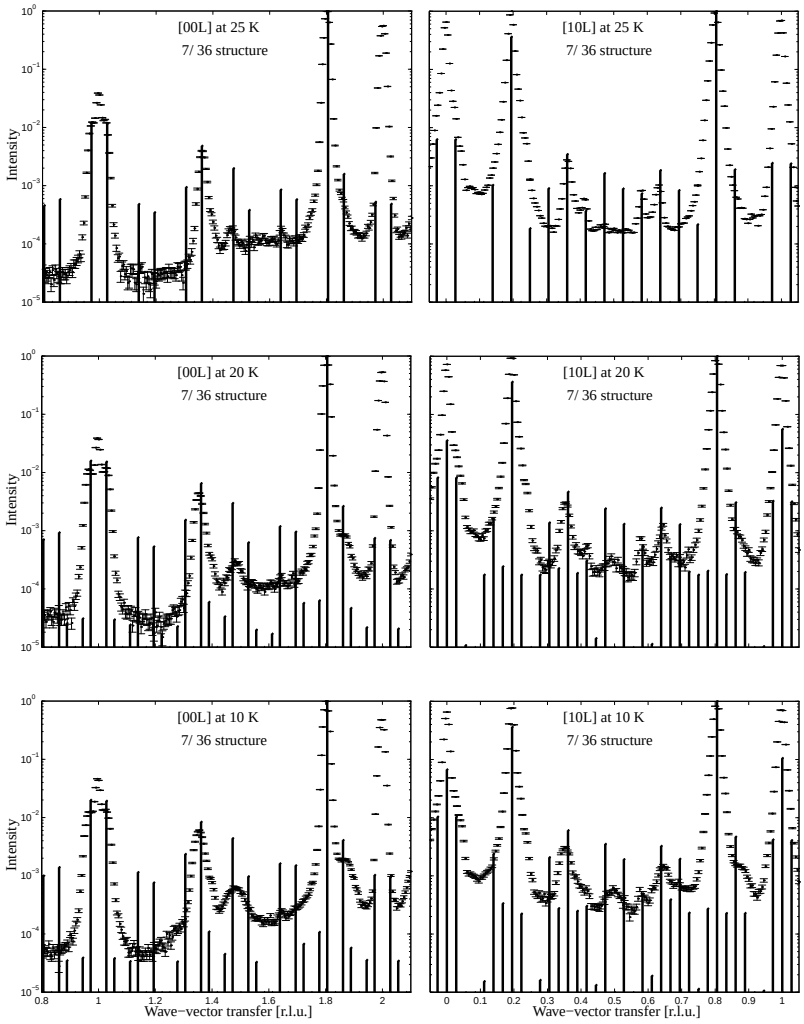

Figure 5.14: Scans from $Ho_{90}Er_{10}$ fitted with MF structures 25 K to 10 K.

hence the resolution effects are not enough to model the broad peaks, and even less successful in reducing the unwanted peaks as seen in figure 5.14

A disordered structure can in contrast to a pure periodic structure not be described by a discrete Fourier transformation. Instead of ideally sharp Bragg peaks it will have a periodicity distribution and hence peaks with finite widths. The higher harmonics which are multiples of the main peak should be expected to have a similar multiplied broadening. Therefore only the highest harmonics (7'th and up) will reveal their intrinsic width beyond the experimental resolution.

The origin of disorder can be explained by the fact that in a random alloy there can be regions with differing concentration. Or that the solute atoms are blocking the relaxation of the structure, so that the actual structure is a mixture of different basal structures. For the 7/36 structure this can simulated by appending a string of 7/35, 7/36 and 7/37 structures, but as seen in figures 5.15(b) and 5.15(c) the result is not satisfactory.

Upon closer examination the 7/36 structure is a *spin slip* structure described by (2221 221), which means that after 3 doublets (i.e. 6 single layers) comes a singlet (spin slip) then two doublets and finally a singlet before the structure is repeated. In other words the helix makes 7/6 turns during 12 single layers, and hence makes 7 full turns after 72 single layers or 36 double layers. One manifestation of disorder could be, that the (2221) and (221) blocks do not follow each other periodically, but are mixed more or less randomly. By mixing $6n$ of each of the two blocks, thus ensuring the right Q and that the structure ends with $7n$ complete turns, disorder can be introduced into the system. Denoting by $(1+p)/2$ the probability, that a (221) structure follows a (2221) structure, the disorder can be continuously turned on, since $p = 1$ corresponds to the pure (2221 221) and $p = 0$ corresponds to a completely random distribution of the two blocks.

It can be seen from figure 5.16 that only the $p = 0$ structure with a completely random distribution of the two blocks have no other peaks, than those seen in the experiments. Most interesting is the fit to the $[0, 0, l]$ scan at 10 K shown in figure 5.17. The best fit is obtained for a random mixing of equally many blocks of $\{4\}$ and $\{3\}$, and an experimental width of the $(0, 0, 2-Q)$ peak of 0.008 r.l.u.. It should of course be remembered that no attempts are made to fit the nuclear peaks. Disregarding the $(1, 0, 0)$ peak the agreement is very satisfactory. It is seen, that the calculated background is to high. But the discrepancy is less than a factor of five on a quantity four orders of magnitudes smaller than the main magnetic peak. All the features including the right shoulder to $(0, 0, 2-Q)$ are qualitatively depicted in the fit.

The disordered 7/36 structure described above is therefore a very good candidate for the low temperature structure in $Ho_{90}Er_{10}$. The reason for this disorder, which is in contrast to the extremely well ordered magnetic systems observed in most of the rare earths can have different explanations:

- The 10% Er atoms does introduce a randomness and a microscopic concentration fluctuation, but within the MF model presented here these effects are averaged over an entire basal plane, and should therefore be negligible. If this effect should be investigated, the model should be reformed to three dimensions with an increasing finite block size. The *virtual-crystal* model could also be abandoned in favour of a random distribution of a finite number of Ho and Er atoms.

- It could also be, that the reason for the disorder effect to appear in this particular system is a coincidence between periodicity and low temperatures. The periodicity corresponds to an average distance $b = 6$ single

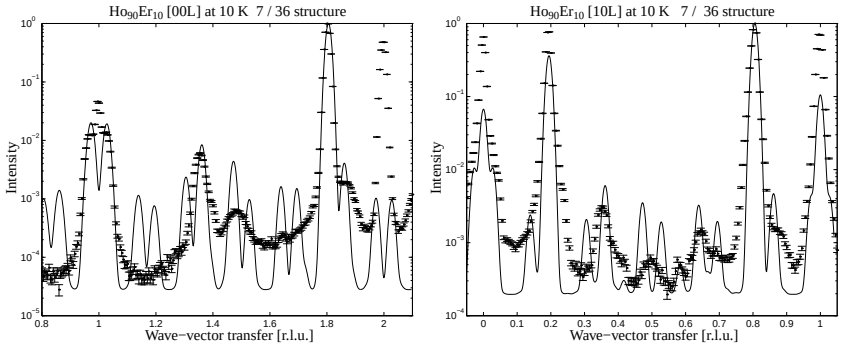

(a) Pure 7/36 with finite width

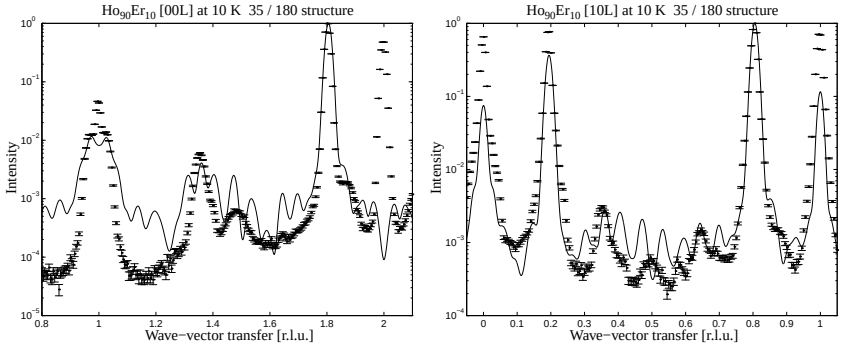

(b) Mixed (7/35)3(7/36)(7/37)

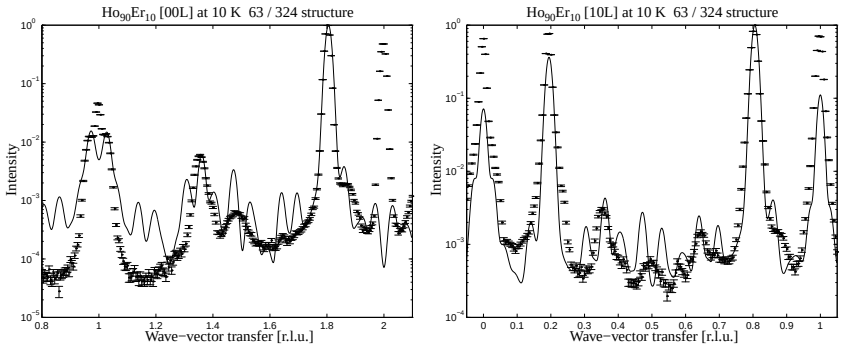

(c) Mixed (7/35)7(7/36)(7/37)

Figure 5.15: Scans along $[0, 0, l]$ in $Ho_{90}Er_{10}$ at 10 K fitted with different structures.

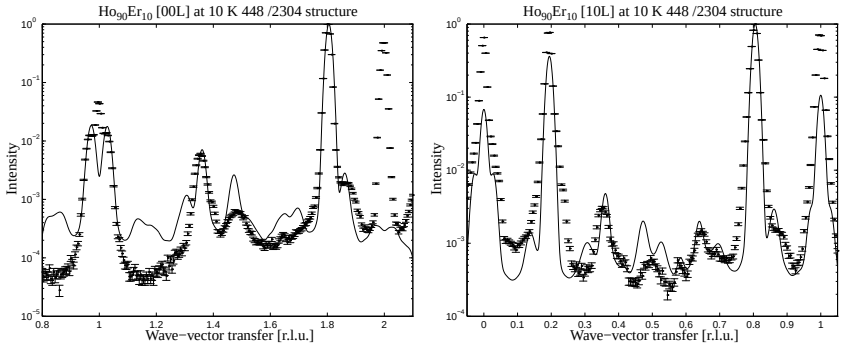

(a) Disordered with $p = 0.6$

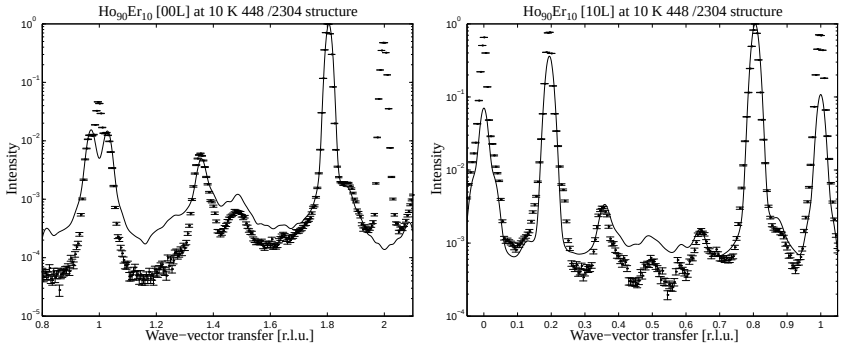

(b) Totally disordered with $p = 0$

Figure 5.16: Scans along $[0, 0, l]$ in $Ho_{90}Er_{10}$ at 10 K fitted with disordered structures.

layers between the spin slips, which cannot be satisfied by a simple spin slip structure. A simple spin slip structure must have b odd, equal to 2 times the number of pairs plus one for the spin slip itself. The average distance $b = 6$ is satisfied by a $\{43\}$ structure. Where blocks of respective $\{3\}$ and $\{4\}$ *hexants* between the spin slips occur with equal rate.

The interchanging of a $\{3\}$ block and a $\{4\}$ block is actually accomplished by moving a single spin from a pair to a adjacent spin singlet. At low temperatures, where the hexagonal anisotropy is large, the barrier for doing so is very large. Since little energy is gained, the structure cannot relax. The ordering of the moments into a structure must be assumed to start at many different places. These individual growing domains have no phase coherence (the phase of the helix), and when they meet, phase shifts and hence disordering of the perfect spin slip structure takes place.

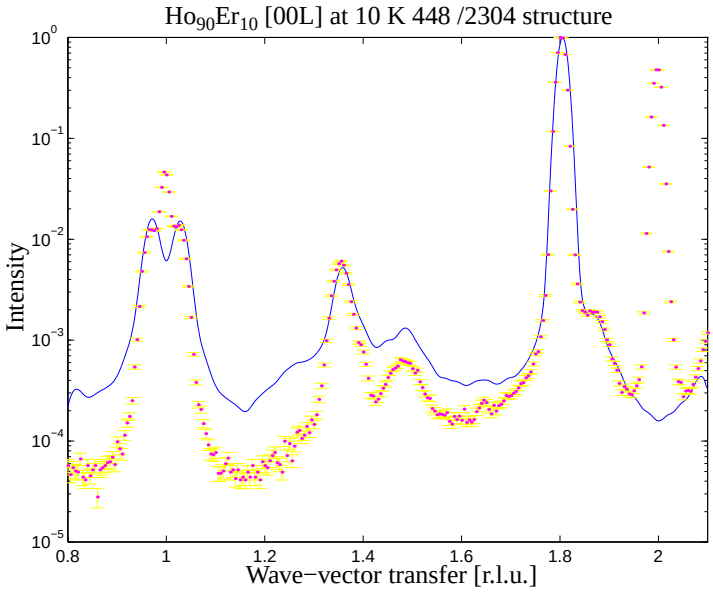

Figure 5.17: Best fit to the $[0, 0, l]$ scan in $Ho_{90}Er_{10}$ at 10 K.

- The flatness of the free energy minimum depicted in figure 5.7(a) means, that there are a wealth of *meta-stable* local minima. In that sense the system resembles a spin glass, where the number of meta-stable states is so large, that the system will not relax even after long time. Therefore, although the absolute minimum free energy is obtained for an ideally alternating sequence of {3} and {4} blocks, the energy difference and the thermal fluctuations are so mall, that the system is quenched in a meta-stable state.

5.2.3 No tilted helix

The *tilted helix* discussed in section 3.1 has not been observed in any system, although MF calculations predict it to be very close in free energy to the cone phase. During the first series of experiments the cone phase transition was measured in $Ho_{90}Er_{10}$. Figure 5.18, sample 1a shows an interesting jump in $I_{(1,0,0)}$ at 12 K from the level of the nuclear peak. This indicated, that the finite ferromagnetic component of the cone phase develops in a sharp transition at 12 K but disappears continuously around $T_C = 25$ K.

This new phase could be just a basal plane helix, but a tilted helix would explain the sharp transition. There is no simple continuous path form the cone to the tilted helix and hence a transition between the two structures will be sharp. The cone-helix transition should be continuous and secondly it seems less plausible that the system should go from the helix to the cone and then

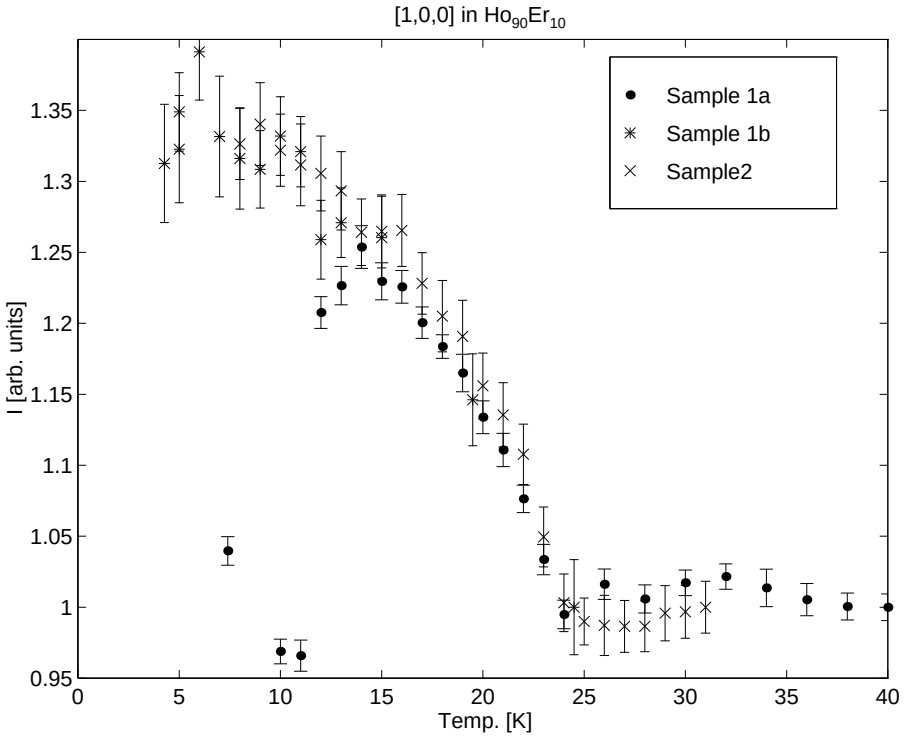

Figure 5.18: $I_{(1,0,0)}$ as a function of temperature.

back to the helix.

Since only a few points (3-5) promoted the tilted helix the results were sought verified in the second beam period. But as apparent in figure 5.18 no evidence of the tilted helix phase was found neither in sample 1b o in sample 2.

In conclusion the evidence for the tilted helix could be ruled out as an experimental error, although no such explanation seems evident. The temperature was well stabilized during a period much longer than the scanning time, and the spectrometer was thoroughly aligned at the Bragg peak prior to the scan. Since the one peak scans follow the peak constantly adjusting to the maximum position, a badly aligned starting point could converge to the maximum during a number of points. But even this could not explain the quite sudden jump from the first three points to the next.

I believe, that the first measurement really did catch a perhaps *meta-stable* tilted helix or even an ordinary helix. Accidentally the uncontrolled cooling process must have quenched the cone transition, which was released upon heating above 12 K. The second experiment was performed in a different cryostat, and hence the cooling conditions were not the same. If fast and controlled cooling is performed the tilted helix might be reachable. However, the purpose of forcing the system into an artificial state can be discussed.

5.3 $Ho_{50}Er_{50}$

The $Ho_{50}Er_{50}$ crystals were expected to be more difficult to investigate - partly due to the more complicated structures in the less well described Er - partly since the $50-50$ composition is most far away from the two models of the elements. Therefore this sample was offered the least attention during the limited amount of beam time. The long scans taken are shown in figures 5.19 and 5.20.

As seen in $Ho_{90}Er_{10}$ the main magnetic peak is accompanied by higher harmonics as the temperature is lowered. Between 50 K and 30 K the two fifth harmonics as well as the $(0,0,1)$ peak discussed earlier appears. Without any indications at 40 K all higher harmonics suddenly becomes evident at 30 K.

The hexagonal anisotropy is responsible for the fifth, seventh and eleventh harmonics, whereas the $(0,0,1+4Q)$, $(1,0,2Q)$ and $(1,0,1-2Q)$ peaks are generated by the trigonal coupling.

In comparison with $Ho_{90}Er_{10}$ there are some differences worth noting.

- The relative amplitudes of the higher harmonics is about an order of magnitude weaker. This is a consequence of the opposite bunching directions in Ho and Er.
- On the other hand, apart from the mosaic tails along $[1,0,l]$ there are no broadening of the peaks.
- And also the diffuse scattering tails seen in $Ho_{90}Er_{10}$ are either absent or much weaker, resulting in a lower background.

All in all the a priori conclusion is that the anisotropic effects are less pronounced, and that no disordered low temperature phase is observed.

5.3.1 Structure fits

The structure fits show that the substantially weaker 5'th harmonics are almost perfectly fitted except for the scan at 40 K, which will be discussed in the following section. The other harmonics are generally a bit overestimated and at 10 K a few peaks are predicted where none are observed. However, the agreement is sufficient to conclude, that the calculated structures are right, and only some details mismatch. Adjusting the anisotropy parameters could reduce the discrepancy, but not enough to justify an abandoning of the parameter free model.

5.3.2 Intermediate phase at $35\ \mathbf{K} < T < 45\ \mathbf{K}$

An intermediate phase was found in $Ho_{50}Er_{50}$. The phase characterized by sharp transitions and anomalies is not believed to be a pure helix as proposed earlier. Possible explanations are discussed but none are found to be completely satisfactory. The phenomena is believed to go beyond a change in the scattering cross-section due to a magnetic structure phase transition.

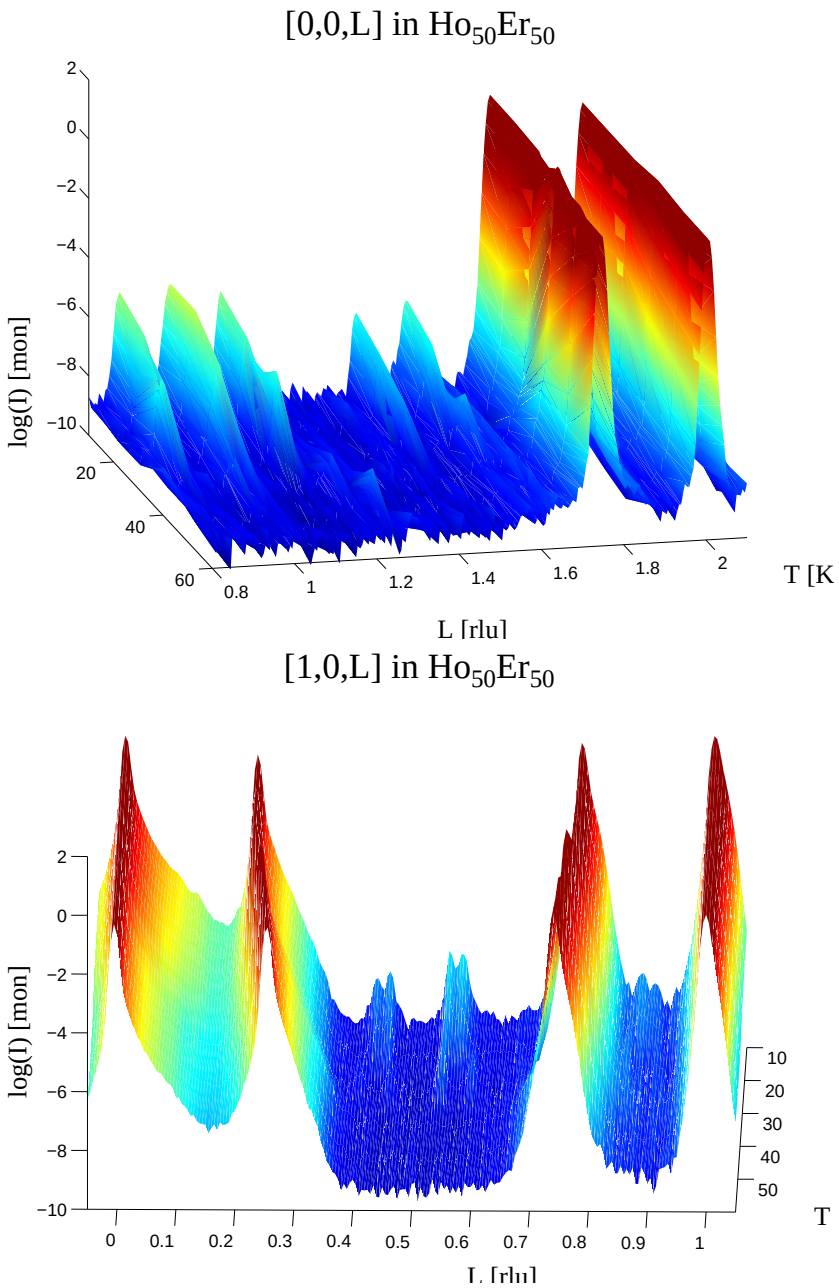

Figure 5.19: $[0, 0, l]$ scans in $Ho_{50}Er_{50}$

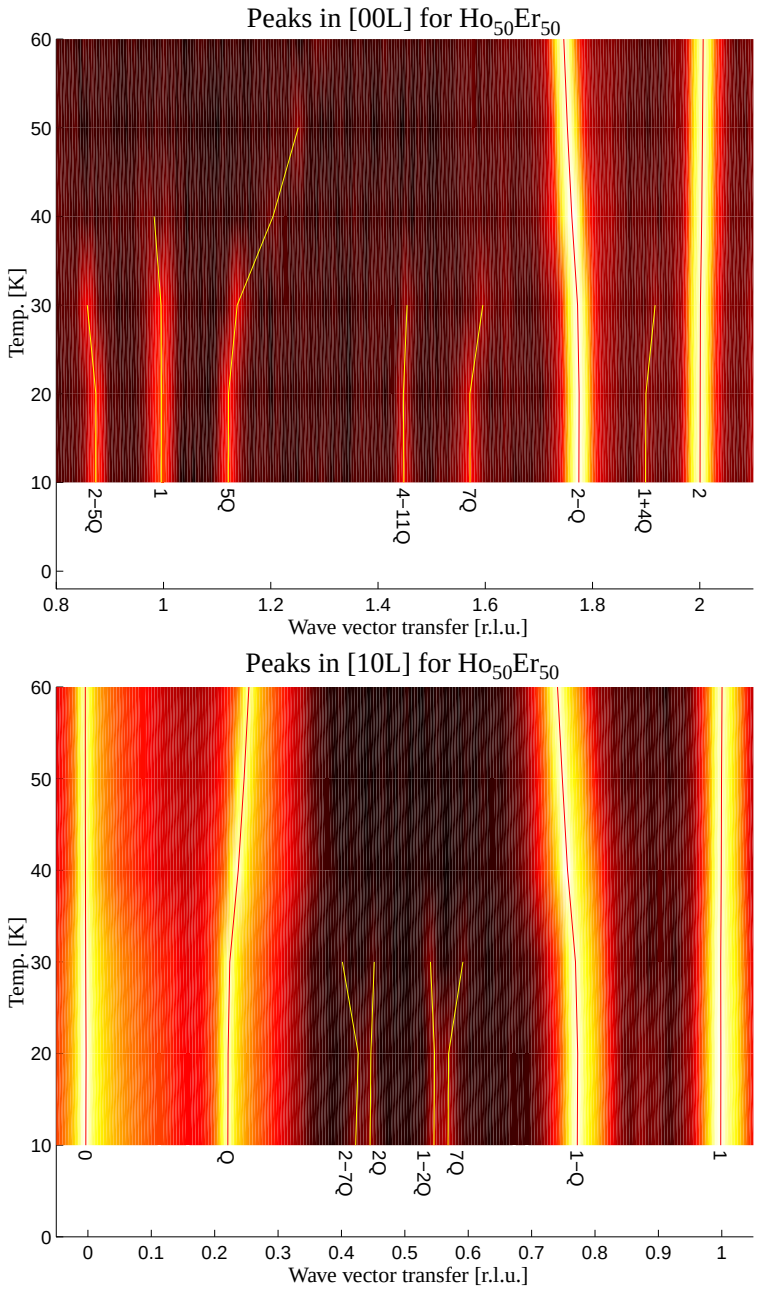

Figure 5.20: Peaks in $Ho_{50}Er_{50}$

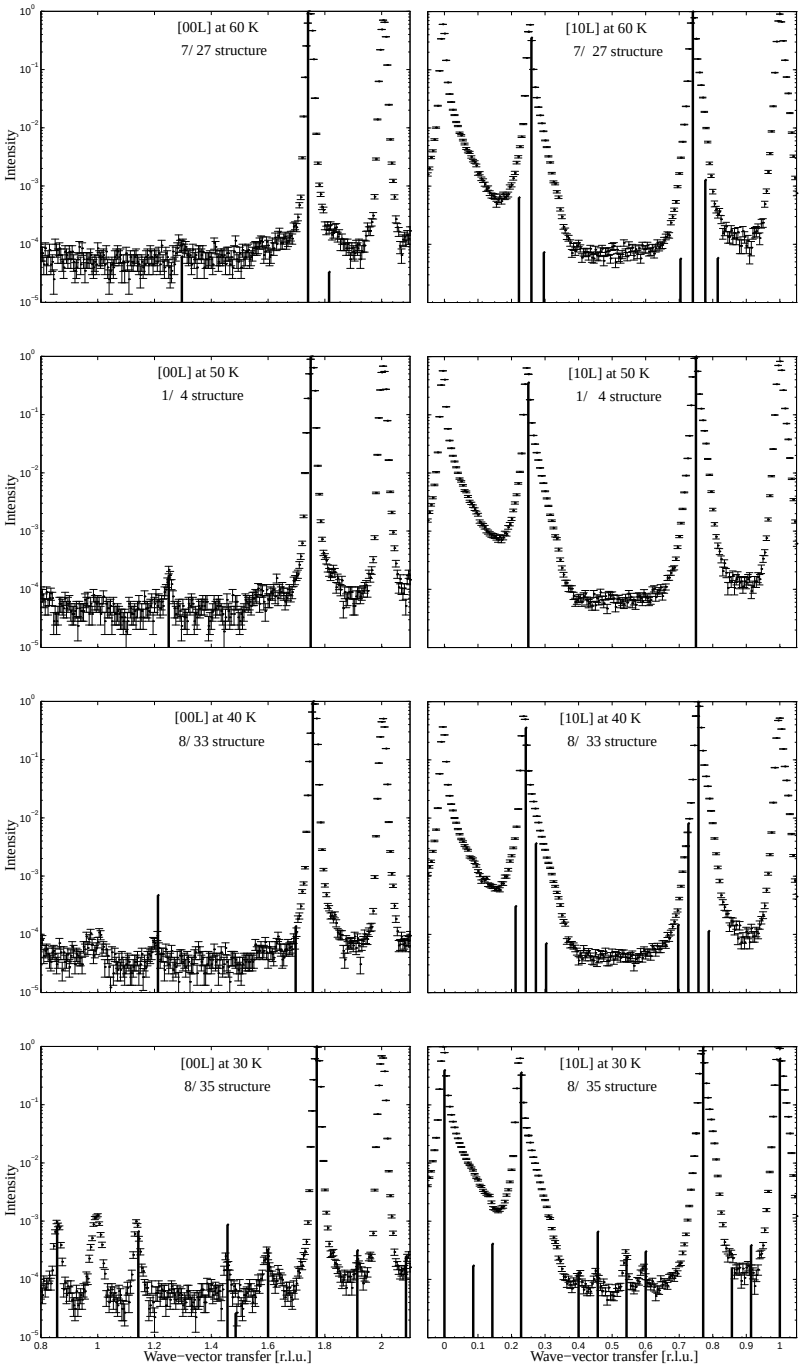

Figure 5.21: Scans from $Ho_{50}Er_{50}$ fitted with MF structures 60 K to 30 K.

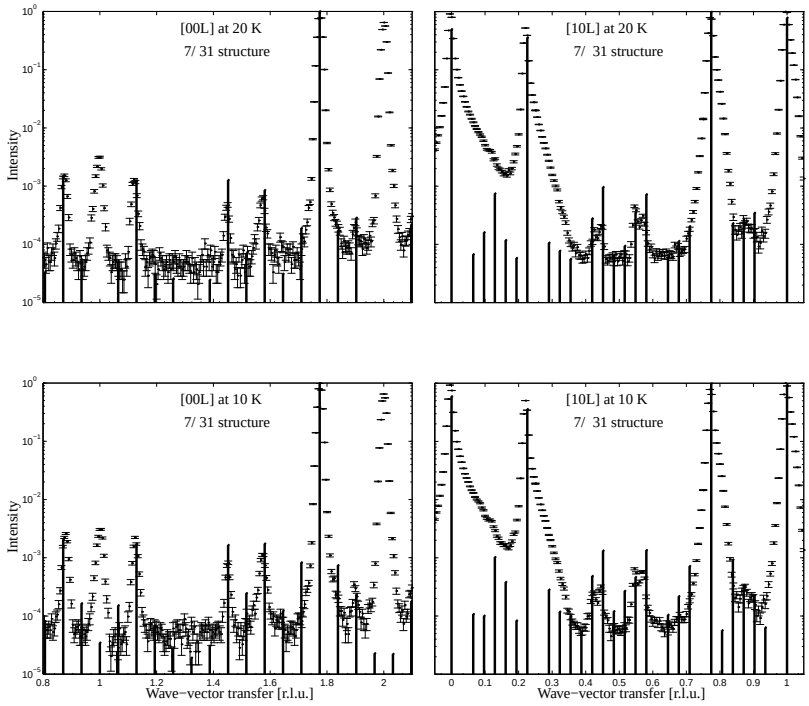

(a) With the trigonal coupling

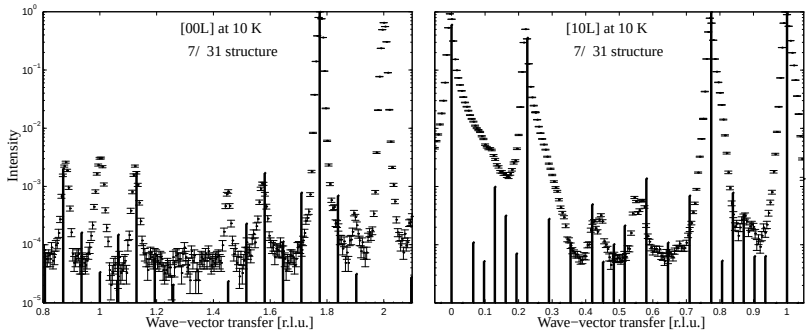

(b) Without the trigonal coupling, the $2Q$ and $4Q$ peaks are not properly fitted.

Figure 5.22: Scans from $Ho_{50}Er_{50}$ fitted with MF structures 20 K and 10 K.

The $Ho_{50}Er_{50}$ crystals displayed three distinct phases as also found by Howard and Bohr (1991). The low temperature cone phase as identified in the $I_{(1,0,0)}$ peak disappears in a rather sharp transition at $T_C = 35$ K. The nuclear amplitude $I_{(1,0,0)}$ remains constant from 35 K to above T_N which means, that there are no other occurrences of the cone phase.

An intermediate phase is seen as an abrupt 50% increase of the $(0, 0, 2 - Q)$ peak at 35 K which disappears slightly less sudden around 45 K. Howard and Bohr (1991) explains the behaviour with a flat helix in the intermediate region followed by a *binary tilted helix* above 45 K. This proposal is abandoned as an unphysical artifact of the scattering model. Their proposed cone angle with $\cos^2 20° \simeq 0.88$ is insufficient to account for the drop in $I_{(0,0,2-Q)}$ below 35 K.

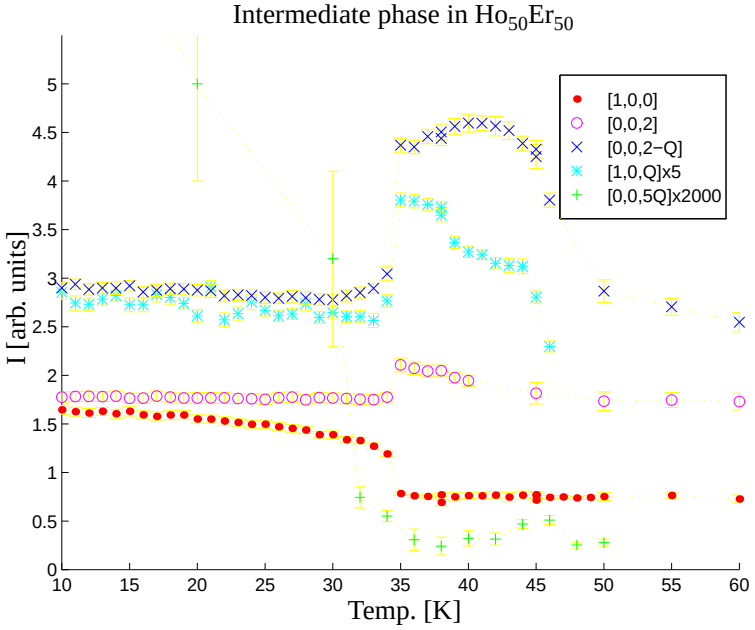

Figure 5.23: The behaviour of the $(0, 0, 2 - Q)$, $(0, 0, 2)$, $(1, 0, 0)$ and $(1, 0, Q)$ peaks within the intermediate phase.

At temperatures just below $T_N = 104$ K, the Er moments must be forced to order by the more strongly coupling Ho moments, as was also seen with resonant x-ray scattering by Pengra *et al.* (1994). While the crystal field is unimportant and the conduction gas is still unpolarized only the exchange coupling is relevant, and the only difference between the two elements is the size of the total spin S. On that basis a possible binary structure cannot be expected in the high temperature regime. If, as is also observed to a much smaller degree in the MF calculations, the two types of moments were to have different directions within the same plane, it should be at low temperatures, where the opposite crystal

fields are significant.

Disregarding this intermediate temperature range $I_{(0,0,2-Q)}$ grows smoothly from a 2. order phase transition at T_N to a zero temperature saturation value. The smooth development of $I_{(0,0,2-Q)}$ from T_N until saturation is identified as the formation of a helical structure. The major problem for that assumption is that the saturation value of $I_{(0,0,2-Q)}$ corresponds to full length moments and hence maximum scattering cross-section. Without further assumptions the increased scattering in the intermediate phase would correspond to angular momenta larger than J which cannot be the case.

The intermediate region was investigated through the $(0, 0, 2 - Q)$, $(0, 0, 2)$, $(1, 0, 0)$ and $(1, 0, Q)$ peaks as well as the fifth harmonic $(0, 0, 5Q)$. As seen in figure 5.23 also the nuclear peak $(0, 0, 2)$ shows anomalies which indicate either a ferromagnetic basal plane component or a more complicated phenomena than a simple magnetic phase transition.

The explanation could be related to the phenomena called extinction relief. Primary *extinction* can cease in case of a domain formation with incoherent phase shifts across domain boundaries. This explanation is however contradicted by the $(0, 0, 5Q)$ peak which does not increase, but suffers a decrease within the same temperature interval. In spite of the poor statistical uncertainty caused by the low intensity of the fifth harmonic it is clearly seen how the peak decreases within the temperature region, comes back above 45 K, but then dies away due to the strong temperature dependence of the fifth harmonics.

The weakening of the fifth harmonic could suggest a pure helix without hexagonal anisotropy — perhaps due to a cancellation of the two competing crystal field directions. Of course the main magnetic peak of the pure helix is more intense than that of a bunched helix, which losses some of its intensity to the higher harmonics. However, this difference can only account for a few percent at most. Secondly since the anisotropic bunching only takes place below 50 K the structure is already pure above this temperature.

Chapter 6

Conclusion

Since conclusions have been drawn at the end of each of the preceding chapters, this chapter is intended to summarize the most important results of this work.

6.1 Structures

The agreement between the measurements and the calculated scattering is sufficient to uniquely determine the main structures in both alloys to be a basal plane *helix* succeeded at low temperatures by a cone structure. As Ho possesses the largest moments and the strongest interactions, the alloys were expected in general to reflect this. However three novel features have been observed:

- Disordered non-equilibrium 7/36 phase in $Ho_{90}Er_{10}$
- Increased stability of the cone phase
- Unidentified intermediate phase in $Ho_{50}Er_{50}$

Whereas the ordering temperature T_N scales linearly between the values of the elements, the cone phase region is extended from $T_C \simeq 20$ K in both elements to $T_C = 35$ K in $Ho_{50}Er_{50}$. This can intuitively be understood in terms of the competition between the basal plane helix in Ho and the *ac*-plane *cycloid* in Er.

The disordered phase in $Ho_{90}Er_{10}$ has been identified with a *spin slip* structure, where the ideal arrangement of alternating 3 and 4 *hexants* between the spin slips are mixed at random. The relaxation of the disordered state lacks motivation due to the flatness of the free energy minimum and is blocked by the hexagonal anisotropy The occurrence of disorder in this particular alloy is believed to be an accidental consequence of the combination of periodicity and temperature.

The intermediate phase in $Ho_{50}Er_{50}$ has been studied. Abandoning the implausible high-temperature *binary tilted helix* structure proposed by Howard and Bohr (1991) leaves the intermediate phase unexplainable. Without introduction

of scattering related phenomena, the increased magnetic scattering would correspond to angular momenta substantially larger that in Ho. Furthermore, the nuclear peaks shows anomalies around the transitions, and the phenomena is most probably results from scattering effects, such as changes in the *extinction* as the crystal passes through a phase transition.

6.2 Interactions

Based on the agreement with the VC-MF model it can be concluded that the alloys are governed by the same types of interactions as the elements. Concerning the numerical strength, a few points are worth noting:

- The *indirect exchange coupling* is mediated by an averaged conduction electron gas. Thus the three different interactions Ho-Ho, Ho-Er and Er-Er all have the same form scaled with the appropriate $(g-1)$ factors.
- The one extra $4f$ electron in Er has the dramatic effect of changing the sign of the *crystal field*. Hence the hexagonal anisotropy leads to different *bunching* directions for the two types of spins. The resulting substantially weaker fifth harmonics in the scans from $Ho_{50}Er_{50}$ are well described by the model.
- Clear evidence of the trigonal coupling is seen as otherwise unexplainable peaks in both $Ho_{90}Er_{10}$ and $Ho_{50}Er_{50}$, although the numerical strength of the coupling could not be determined.

6.3 The VC-MF model

The VC-MF model constructed on the basis of models for Ho and Er has the desirable property of having essentially no free parameters. It provides a remarkably good description of the alloys. The physical importance of the model can be discussed.

If only the structure is of interest, the MF-VC model can be considered a sophisticated means of generating good structure guesses. In general the generated structures produce scattering sufficiently close to the measured to be of use.

On the other hand, given the models for Ho and Er, it is a microscopic model, which can provide physical information. As such it has it successes and failures:

- Neither the periodicity Q or the relative magnetization σ can be deduced from the model. Therefore these two quantities have to be imposed on the calculations — effectively introducing two parameters to the model.
- The first transition temperature T_N is by construction right in pure Ho and Er, and also the alloys are well described.

- The mean-field model for Er only predicts the cone phase in Er to be *meta-stable*. The failure of the VC-MF model to describe the cone phase in the alloys was expected. Surprisingly $Ho_{50}Er_{50}$ is predicted to have a cone phase with the right cone angle but wrong transition temperature.
- The relative intensity of the fifth harmonics are reproduced within a factor of 1.4, which means that the competing hexagonal anisotropic bunching angles are well described.
- Disorder as observed in $Ho_{90}Er_{10}$ can only be treated in model introduced by hand. A more native description of disorder must be based on a regular modification of the model.
- Within the intermediate phase in $Ho_{50}Er_{50}$. the model does not predict any transitions at all. The intermediate phase could be the result of a pure scattering phenomenon with an unchanged structure, but more likely it is a magnetostrictive coupling between the lattice and the magnetic ordering. The investigation of such a coupling would require a comprehensive extension of the model.
- In general, the right higher harmonics are predicted, but the amplitudes are only partly satisfactory. This is interpreted as the right choice of interactions, but a not perfect choice of parameters.

The model could be sought improved by adjustment of the parameters, but that would change it to a completely phenomenological model. Furthermore, once the interaction parameters are set free, the present experimental material is insufficient to uniquely fix them again. In that case more detailed measurements including field dependence and a study of the dynamics must be performed.

I believe that the limit of success for the model is drawn by the unsatisfactory description of the relatively large anisotropic interactions in pure Er. Perhaps if the model for Er is improved also the alloys would be better described.

Appendix A

Dynamics

Within the MF model for a magnetic structure like those those described so far the configuration of each spin is determined by the corresponding crystal field in competition with the exchange field.

For a given site the energy difference from the ground state to the first excited state is in the order of 5 meV $\simeq$ 60 K. Such single spin excitations are of little interest first because they require a large excitation energy, second because they are not eigenstates of the system and will decay rapidly. However, there exist a different type of excitations, called spin waves or magnons. These collective excitations are similar to the quantized collective modes of the crystal motion called phonons.

A.1 Linear response theory — generalized susceptibility

The classical magnetic susceptibility is defined as the linear response in the form of magnetization in a magnetic material due to an external field $M = \chi H$.

This concept can be generalized to include the response of the system to a perturbation varying in space an time. There are many possibilities for the definition of such a response. The presentation chosen here is not in general the most convenient, but for this specific purpose there is no need to bring the full (and overlapping) set of definitions found in the literature into action.

Consider the linear effect of a perturbation Hamiltonian $\mathcal{H} = Af(t)$ on the ensemble average $\langle B(t)\rangle$ of a macroscopic physical observable. This is best expressed in terms of the Fourier transforms with respect to time, where it takes the form:

$$\langle B(\omega)\rangle = \chi_{BA}(\omega) f(\omega). \tag{A.1}$$

In principle the generalized susceptibility is not well defined for real values of ω, but is defined as $\chi(\omega) = \lim_{\epsilon\to 0^+} \chi(\omega + i\epsilon)$.

Since χ_{AB} is an analytical function, complex functional theory implies certain relations regarding symmetry and between the real and imaginary parts.

With the aid of the equation of motion in the interaction picture χ can be derived from the operators A and B:

$$\begin{aligned}\chi_{AB}(\omega) &= \lim_{\epsilon\to 0^+}\sum_{ab'}\frac{\langle a|\,B\,|b\rangle\,\langle b|\,A\,|a\rangle}{E_b-E_a-\hbar\omega+i\hbar\epsilon}(n_a-n_b)\\ &= \lim_{\epsilon\to 0^+}\left\{\sum_{ab'}^{E_a\neq E_b}\frac{\langle a|\,B\,|b\rangle\,\langle b|\,A\,|a\rangle}{E_b-E_a-\hbar\omega+i\hbar\epsilon}(n_a-n_b)\right.\\ &\quad\left.+\frac{1}{k_BT}\frac{i\epsilon}{\omega+i\epsilon}\sum_{ab'}^{E_a=E_b}\langle a|\,B\,|b\rangle\,\langle b|\,A\,|a\rangle\,n_a-\langle B\rangle\,\langle A\rangle\right\}.\end{aligned}\tag{A.2}$$

There is a close relationship between the defined χ and the time retarded Green function $G_{AB}(t)\equiv\langle\langle B(t);A(0)\rangle\rangle$in that $G_{AB}(\omega)=-\chi_{AB}(\omega)$.

A.2 Random phase approximation

The mean-field approximation was introduced in order to separate the two-ion part of the Hamiltonian into single-ion operators by neglecting the two-ion fluctuations. The spin waves however are collective fluctuations, and hence it is necessary to improve the approximation. The i'th Hamiltonian in the presence of a small perturbing field $h_i(t)$ can be written as:

$$\mathcal{H}=\mathcal{H}_{\mathrm{MF}}(i,t)-(\boldsymbol{J}_i(t)-\langle\boldsymbol{J}_i\rangle)\cdot\left\{\sum_j\boldsymbol{\mathcal{J}}(ij)(\boldsymbol{J}_j(t)-\langle\boldsymbol{J}_j\rangle)+\boldsymbol{h}_i(t)\right\}.\tag{A.3}$$

The MF approximation corresponds to putting $\boldsymbol{J}_j(t)$ equal to $\langle\boldsymbol{J}_j\rangle$. With $\langle\boldsymbol{J}_i(\omega)\rangle$ as the Fourier transform of $\langle\boldsymbol{J}_i(t)\rangle-\langle\boldsymbol{J}_i\rangle$ this defines $\langle\boldsymbol{J}_i(\omega)\rangle_{\mathrm{MF}}=\boldsymbol{\chi}_i^0(\omega)h_i(\omega)$. This one-ion susceptibility just reflects the single ion excitations.

Using equation A.2 it can be calculated from the eigenstates and eigenvalues obtained from the mean-field structure calculations. The imaginary infinitesimal $i\epsilon$ is kept finite, which causes a smearing of the susceptibility. This broadening in energy can be adjusted directly to fit the experimental resolution. Or, as long as it is chosen smaller, it will be "eaten" when folded with the resolution function.

A less drastic approximation would be to replace $\boldsymbol{J}_j(t)$ with $\langle\boldsymbol{J}_j(t)\rangle$. This would be valid if the differences for each j were uncorrelated in which case the j sum would be a sum over random phase factors and hence cancel out. For this reason it is called the random phase approximation. Within the RPA,

$$\langle\boldsymbol{J}_i(\omega)\rangle=\boldsymbol{\chi}_i^0(\omega)\boldsymbol{h}_i^{\mathrm{eff}}(\omega)\quad,\quad\boldsymbol{h}_i^{\mathrm{eff}}(\omega)=\boldsymbol{h}_i(\omega)+\sum_j\boldsymbol{\mathcal{J}}(ij)\,\langle\boldsymbol{J}_j(\omega)\rangle\,.\tag{A.4}$$

Another general way of expressing the response is through the two-ion susceptibility coupling the i'th fluctuation to all the $\boldsymbol{h}_j$'s:

$$\langle \boldsymbol{J}_i(\omega) \rangle = \sum_j \boldsymbol{\chi}(ij,\omega)\boldsymbol{h}_j(\omega). \tag{A.5}$$

These two expressions for the i'th fluctuation combine into the self consistence RPA equation:

$$\boldsymbol{\chi}(ij,\omega) = \boldsymbol{\chi}_i(\omega)^0 \left[\delta_{ij} + \sum_{j'} \boldsymbol{\mathcal{J}}(ij')\boldsymbol{\chi}(j'j,\omega)\right]. \tag{A.6}$$

A.3 The RPA equation

The RPA equation is in general an infinite set of coupled equations. Depending on the system under consideration the existence of translational symmetry can be used to Fourier transform the equations into a finite matrix equation. In the following the ω dependence will be suppressed.

A.3.1 The Heisenberg ferromagnet

In the ferromagnet $\boldsymbol{\chi}_i^0 = \boldsymbol{\chi}^0$ and with the Fourier transformations:

$$\begin{aligned} \boldsymbol{\mathcal{J}}(\boldsymbol{q}) =& \sum_i \boldsymbol{\mathcal{J}}(ij) e^{-i\boldsymbol{q}\cdot(\boldsymbol{R}_i - \boldsymbol{R}_j)} \\ \boldsymbol{\chi}(\boldsymbol{q}) =& \frac{1}{N}\sum_{ij} \boldsymbol{\chi}(ij) e^{-i\boldsymbol{q}\cdot(\boldsymbol{R}_i - \boldsymbol{R}_j)}, \end{aligned} \tag{A.7}$$

the equation is solved as:

$$\boldsymbol{\chi}^0(\boldsymbol{q}) = \left[\mathbf{1} - \boldsymbol{\chi}^0\boldsymbol{\mathcal{J}}(\boldsymbol{q})\right]^{-1}\boldsymbol{\chi}^0. \tag{A.8}$$

A.3.2 The commensurate helix

In the alloy there are two complications: first there are M different one ion susceptibilities and second there are two different types of ions. The first problem is overcome straight forwardly by extending the Fourier transformation:

$$\begin{aligned} \boldsymbol{\chi}^0(n) =& \frac{1}{N}\sum_i \boldsymbol{\chi}_i^0 e^{-in\boldsymbol{Q}\cdot\boldsymbol{R}_i} \\ \boldsymbol{\chi}(n,\boldsymbol{q}) =& \frac{1}{N}\sum_{ij} \boldsymbol{\chi}(ij) e^{-i\boldsymbol{q}\cdot(\boldsymbol{R}_i - \boldsymbol{R}_j)} e^{-in\boldsymbol{Q}\cdot\boldsymbol{R}_i}. \end{aligned} \tag{A.9}$$

Upon insertion, the RPA equations A.6 can be solved using the identity relation $1 = \sum_{i'} \delta_{ii'} = 1/N \sum_{i'm} e^{-im\boldsymbol{Q}\cdot(\boldsymbol{R}_{i'}-\boldsymbol{R}_i)}$, which enables a separation by change of summation:

$$\begin{aligned}
\boldsymbol{\chi}(n,\boldsymbol{q}) =& \frac{1}{N}\sum_{ij}\boldsymbol{\chi}_i^0\left[\delta_{ij}+\sum_{j'}\boldsymbol{\mathcal{J}}(ij')\boldsymbol{\chi}(j'j))\right]e^{-i\boldsymbol{q}\cdot(\boldsymbol{R}_i-\boldsymbol{R}_j)}e^{-in\boldsymbol{Q}\cdot\boldsymbol{R}_i}\\
=&\boldsymbol{\chi}_i^0(n)+\frac{1}{N}\sum_{ii'jj'}\delta_{ii'}\boldsymbol{\chi}_i^0\boldsymbol{\mathcal{J}}(i'j')\boldsymbol{\chi}(j'j)e^{-i\boldsymbol{q}\cdot(\boldsymbol{R}_{i'}-\boldsymbol{R}_j)}e^{-in\boldsymbol{Q}\cdot\boldsymbol{R}_i}\\
=&\boldsymbol{\chi}_i^0(n)+\frac{1}{N^2}\sum_{ii'jj'm}\boldsymbol{\chi}_i^0\boldsymbol{\mathcal{J}}(i'j')\boldsymbol{\chi}(j'j)\\
&\qquad\times e^{-i\boldsymbol{q}\cdot(\boldsymbol{R}_{i'}-\boldsymbol{R}_j)}e^{-in\boldsymbol{Q}\cdot\boldsymbol{R}_i}e^{-im\boldsymbol{Q}\cdot(\boldsymbol{R}_{i'}-\boldsymbol{R}_i)}\\
=&\boldsymbol{\chi}_i^0(n)+\frac{1}{N^2}\sum_{ii'jj'm}\boldsymbol{\chi}_i^0e^{-i(n-m)\boldsymbol{Q}\cdot\boldsymbol{R}_i}\boldsymbol{\mathcal{J}}(i'j')e^{-i(\boldsymbol{q}+m\boldsymbol{Q})\cdot(\boldsymbol{R}_{i'}-\boldsymbol{R}_{j'})}\\
&\qquad\times\boldsymbol{\chi}(j'j)e^{-i\boldsymbol{q}\cdot(\boldsymbol{R}_{j'}-\boldsymbol{R}_j)}e^{-im\boldsymbol{Q}\cdot\boldsymbol{R}_{j'}}\\
=&\boldsymbol{\chi}_i^0(n)+\sum_m\boldsymbol{\chi}^0(n-m)\boldsymbol{\mathcal{J}}(\boldsymbol{q}+m\boldsymbol{Q})\boldsymbol{\chi}(m,\boldsymbol{q}).
\end{aligned}\tag{A.10}$$

With the definitions:

$$\begin{aligned}
\widetilde{\boldsymbol{\chi}}(\boldsymbol{q}) \equiv&\{\boldsymbol{\chi}(n,\boldsymbol{q})\}\\
\widetilde{\boldsymbol{\chi}}^0 \equiv&\{\boldsymbol{\chi}^0(n)\}\\
\widetilde{\widetilde{\boldsymbol{M}}}_{nm}(\boldsymbol{q}) \equiv&\boldsymbol{\chi}^0(n-m)\boldsymbol{\mathcal{J}}(\boldsymbol{q}+m\boldsymbol{Q}),
\end{aligned}\tag{A.11}$$

the equation can be brought to matrix form and solved:

$$\widetilde{\boldsymbol{\chi}}(\boldsymbol{q}) = \widetilde{\boldsymbol{\chi}}^0+\widetilde{\widetilde{\boldsymbol{M}}}(\boldsymbol{q})\widetilde{\boldsymbol{\chi}}(\boldsymbol{q}) \tag{A.12.a}$$

$$= (\mathbf{1}-\widetilde{\widetilde{\boldsymbol{M}}}(\boldsymbol{q}))^{-1}\widetilde{\boldsymbol{\chi}}^0. \tag{A.12.b}$$

Hence the two-ion susceptibility can be calculated from the one-ion mean-field susceptibility by constructing and inverting a finite matrix $(1-\widetilde{\widetilde{\boldsymbol{M}}}(\boldsymbol{q}))$ for each $(\boldsymbol{q},\omega)$ point. The dimension of the matrix is N^2 times the dimension of $\boldsymbol{\chi}_i^0$.

As an extension of the mean-field program, a program has been developed for the calculation of the two-ion susceptibility. For a given grid of $(\boldsymbol{q},\omega)$ points, $\boldsymbol{\chi}^0(\omega_m)$ and $\boldsymbol{\mathcal{J}}(\boldsymbol{q}+m\boldsymbol{Q})$ has to be calculated once for each ω and $\boldsymbol{q},m$ respectively. In practice this leads to substantial computational tasks. For this reason the calculations has been limited to a few illustrative cases.

A.3.3 The binary alloy

The binary alloy described by $\boldsymbol{J}_i \equiv c_i \boldsymbol{J}_{1i} + (1-c_i)\boldsymbol{J}_{2i}$ is treated in the *virtual-crystal* approximation. The mean-field exchange Hamiltonian for the i'th site containing an atom of type r is approximated by replacing the alloy configuration variable c_{ri} in the mean-field term with the configurational average $c_r = \sum_i c_{ri}$:

$$\begin{aligned}\mathcal{H}_r^{\mathrm{MF}}(i) =& - c_{ri}(\boldsymbol{J}_{ri} - \frac{1}{2}\langle \boldsymbol{J}_{ri}\rangle)\sum_{js} \boldsymbol{\mathcal{J}}_{rs}(ij) c_{sj}\langle \boldsymbol{J}_{sj}\rangle \simeq \\ \mathcal{H}_r^{\mathrm{VC}}(i) =& - c_{ri}(\boldsymbol{J}_{ri} - \frac{1}{2}\langle \boldsymbol{J}_{ri}\rangle)\sum_{js} \boldsymbol{\mathcal{J}}_{rs}(ij) c_{s}\langle \boldsymbol{J}_{sj}\rangle. \end{aligned} \tag{A.13}$$

From this the one-ion susceptibilities $\boldsymbol{\chi}_{ri}^0$ can be defined and calculated according to equation A.2. The corresponding two-ion susceptibilities $\boldsymbol{\chi}_{rs}(ij)$ are then given by the RPA equation:

$$\boldsymbol{\chi}_{rs}(ij) = \boldsymbol{\chi}_{ri}^0(\delta_{rs}\delta_{ij} + \sum_{j's'} \boldsymbol{\mathcal{J}}_{rs'}(ij')\boldsymbol{\chi}_{s's}(j'j)). \tag{A.14}$$

Writing the exchange coupling as:

$$\boldsymbol{\mathcal{J}}_{rs}(\boldsymbol{q}) = \gamma_{rs}\boldsymbol{\mathcal{J}}(\boldsymbol{q}), \text{ where } \gamma_{rs} = (g_r - 1)(g_s - 1),$$

and defining:

$$\widetilde{\widetilde{\boldsymbol{M}}}_{nm,r}(\boldsymbol{q}) = \boldsymbol{\chi}_r^0(n-m)\boldsymbol{\mathcal{J}}(\boldsymbol{q} + mQ), \tag{A.15}$$

equation A.12.a can be generalized and solved:

$$\begin{aligned} \widetilde{\boldsymbol{\chi}}(\boldsymbol{q}) =& \delta_{rs}\widetilde{\boldsymbol{\chi}}_r^0 + \sum_{s'} \widetilde{\widetilde{\boldsymbol{M}}}_r(\boldsymbol{q})\gamma_{rs'}\widetilde{\boldsymbol{\chi}}_{s's}(\boldsymbol{q}) \\ \sum_{s'}\left(\delta_{rs'} - \widetilde{\widetilde{\boldsymbol{M}}}_r(\boldsymbol{q})\gamma_{rs'}\right)\widetilde{\boldsymbol{\chi}}_{s's}(\boldsymbol{q}) =& \delta_{rs}\widetilde{\boldsymbol{\chi}}_r^0 \\ \left(\underline{\underline{1}} - \underline{\underline{\widetilde{\widetilde{\boldsymbol{M}}}}}(\boldsymbol{q})\underline{\underline{\gamma}}\right)\underline{\underline{\widetilde{\boldsymbol{\chi}}}}(\boldsymbol{q}) =& \underline{\underline{\widetilde{\boldsymbol{\chi}}}}^0\underline{\underline{1}} \\ \underline{\underline{\widetilde{\boldsymbol{\chi}}}}(\boldsymbol{q}) =& \left(\underline{\underline{1}} - \underline{\underline{\widetilde{\widetilde{\boldsymbol{M}}}}}(\boldsymbol{q})\underline{\underline{\gamma}}\right)^{-1}\underline{\underline{\widetilde{\boldsymbol{\chi}}}}^0. \end{aligned} \tag{A.16}$$

Again the two-ion susceptibilities can be found by inverting a finite matrix for each $(\boldsymbol{q}, \omega)$ point.

The scattering cross-section for an alloy is obtained by substituting:

$$(\tfrac{1}{2}gF(\boldsymbol{q}))^2\boldsymbol{\chi}(\boldsymbol{q},\omega) \to \sum_{rs}(\tfrac{1}{2}g_rF_r(\boldsymbol{q}))\boldsymbol{\chi}_{rs}(\boldsymbol{q},\omega)(\tfrac{1}{2}g_sF_s(\boldsymbol{q})). \tag{A.17}$$

A.3.4 Other couplings

The static structures determine the eigenstates from which the one-ion susceptibilities are calculated. In the evaluation of these eigenstates, the full model Hamiltonian is used, but as presented above only the exchange interaction has been directly included in the dynamic calculations. The *dipole coupling* is straightforwardly treated by including it in the $\boldsymbol{\mathcal{J}}_{zz}$ component.

The quadrupolar coupling in Er can be introduced by writing the interaction Hamiltonian in terms of generalized spins:

$$\begin{aligned}
\overset{(5)}{J} &= (J_x, J_y, J_z, O_3^2, O_3^{-2}) \\
\overset{(5)}{\mathcal{H}} &= -\frac{1}{2}\sum_{ij} \overset{(5)}{\boldsymbol{J}_i}\overset{(5)}{\boldsymbol{\mathcal{J}}}(ij)\overset{(5)}{\boldsymbol{J}_j} \\
\overset{(5)}{\boldsymbol{\mathcal{J}}} &= \begin{pmatrix} \boldsymbol{\mathcal{J}} & 0 \\ 0 & \boldsymbol{\kappa}_{33}^{2-2} \end{pmatrix},
\end{aligned} \tag{A.18}$$

and defining the corresponding 5×5 dimensional susceptibility $\overset{(5)}{\boldsymbol{\chi}}$.

The trigonal coupling is more complicated to incorporate, since it partially breaks the translational symmetry into $\boldsymbol{\mathcal{J}}(ij) = (-1)^i \boldsymbol{\mathcal{J}}(i-j)$.

A.4 Scattering cross-section — magnon dispersion

As mentioned in section 4.1.2 the scattering cross-section is directly proportional to the imaginary part of the generalized two-ion susceptibility. A naive comparison with measurements is therefore just a problem of adjusting the artificial width introduced through the imaginary energy $i\epsilon$ in equation A.2 to fit the experimental resolution.

If however, the susceptibility is interpreted in terms of spin waves or magnons, then the peaks along ω in the susceptibility form the dispersion relation, the width corresponding to a finite life time. Therefore plots of the imaginary part of the susceptibility depicts both the expected scattering from the system as well as the structure of the excitations.

Without any experimental data to compare with, a relatively simple 1/5 structure existing in $Ho_{90}Er_{10}$ around 30 K is chosen as an example. A few inelastic scans along ω has been performed on the large $Ho_{90}Er_{10}$ sample. However, as seen from figure A.2 the energy resolution of the TAS1 spectrometer and neutron flux are insufficient to perform such experiments. Clear peaks along ω are apparent, but they are very uncertain. In the scans are too few for a dispersion relation to be determined.

However there is some resemblance between the scan and a calculation performed at $(0, 0, 1.6)$. Unfortunately the 7/36 requires too long computational

Figure A.1: Calculated scattering from a 1/5 structure in $Ho_{90}Er_{10}$.

time for a calculation like figure A.1 to be performed. But with reasonable data at hand, the effort could be rewarded with important knowledge about the form of the interactions in the system.

A.5 Rotating coordinate system

The spin wave dispersion relation in the $[0, 0, l]$ direction for a helical structure consists of two branches each centred around $\tau \pm q$ corresponding to the spin wave propagating parallel or anti parallel to the helix. If the dispersion relation is considered in a rotating coordinate system, these two branches becomes equal, and the picture becomes simpler.

Introducing $\phi_i = 2\pi i/n = \boldsymbol{Q} \cdot \boldsymbol{R}_i$ such a rotation is accomplished by the transformation:

$$\begin{aligned} J_{x'} =& J_x \cos\phi + J_y \sin\phi \\ J_{y'} =& J_y \cos\phi - J_x \sin\phi \end{aligned} \tag{A.19}$$

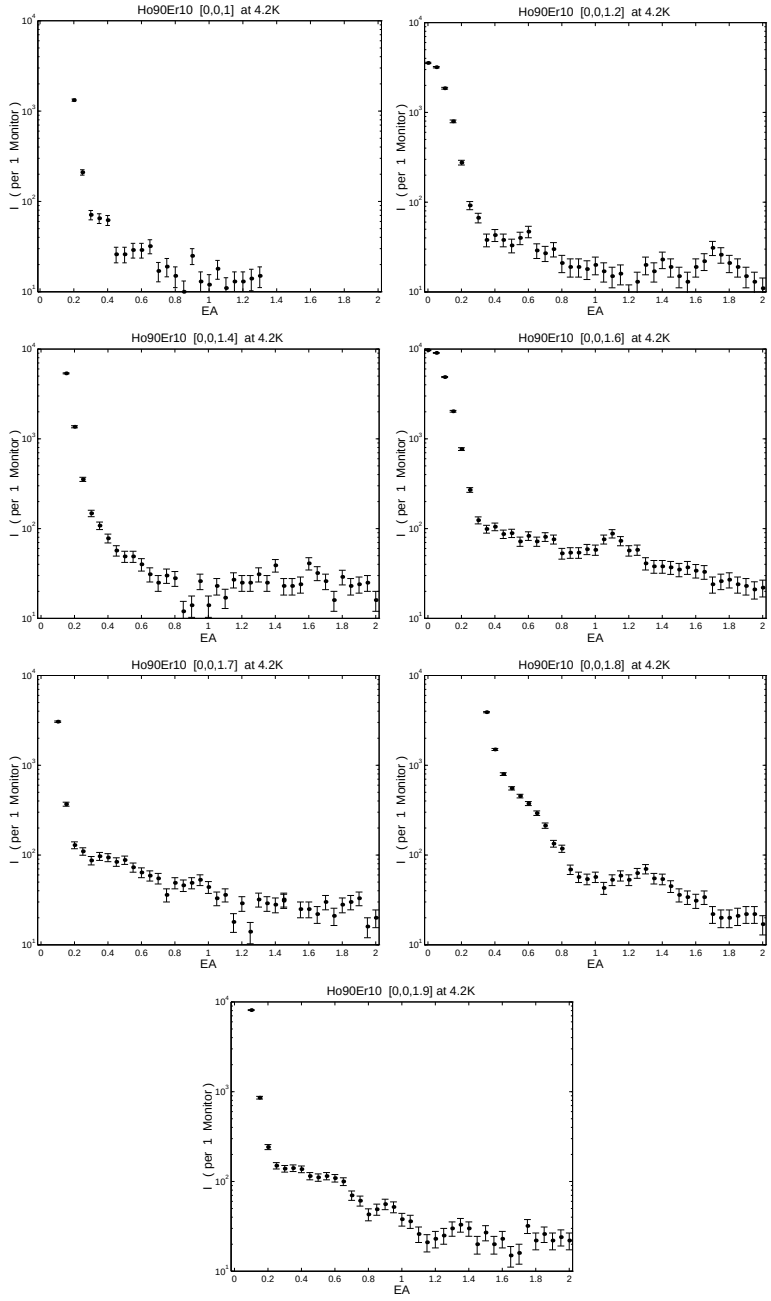

Figure A.2: Inelastic scattering from $Ho_{90}Er_{10}$ at 4.2 K

or $\boldsymbol{J}' = \boldsymbol{R}\boldsymbol{J} = \boldsymbol{J}\boldsymbol{R}^\dagger$, where $\boldsymbol{R}(\phi) = \begin{pmatrix} \cos\phi & \sin\phi & 0 \\ -\sin\phi & \cos\phi & 0 \\ 0 & 0 & 1 \end{pmatrix}$.

This influences the one-ion Green functions through the terms $\langle \boldsymbol{J}' \rangle \cdot \langle \boldsymbol{J}' \rangle = \boldsymbol{R}\langle \boldsymbol{J} \rangle \cdot \boldsymbol{R}\langle \boldsymbol{J} \rangle = \boldsymbol{R}\langle \boldsymbol{J} \rangle \cdot \langle \boldsymbol{J} \rangle \boldsymbol{R}^\dagger$, and hence $\boldsymbol{\chi}_i' = \boldsymbol{R}\boldsymbol{\chi}_i\boldsymbol{R}^\dagger$.

The rotation of $O_3^{\pm 2}(\boldsymbol{J})$ is a bit different, since $J_\pm' = J_\pm e^{\mp i\phi}$:

$$O'^{\pm}_2 = \frac{1}{2\sqrt{\pm 1}}(J_+^2 e^{-2i\phi} \pm J_-^2 e^{2i\phi}) = O_2^{\pm}\cos 2\phi \pm O_2^{\mp}\sin 2\phi. \tag{A.20}$$

Writing $\overset{(5)}{\boldsymbol{J}} = \{J_x, J_y, J_x, O_3^2, O_3^{-2}\}$ this can be incorporated into a 5×5 rotation matrix $\boldsymbol{R}$, keeping in mind that $\boldsymbol{R}^\dagger = \boldsymbol{R}^{-1}$ and $\boldsymbol{R}^{-1}(\phi) = \boldsymbol{R}(-\phi)$.

Now considering the coupling parameters, the coupling term of the Hamiltonian can be written as $\boldsymbol{J}_i\boldsymbol{\mathcal{J}}(ij)\boldsymbol{J}_j = \boldsymbol{J}_i'(\boldsymbol{R}_i^\dagger)^{-1}\boldsymbol{\mathcal{J}}\boldsymbol{R}_j^{-1}\boldsymbol{J}_j'$, and hence $\boldsymbol{\mathcal{J}}' = \boldsymbol{R}_i\boldsymbol{\mathcal{J}}\boldsymbol{R}_j'$. However, since $\boldsymbol{\mathcal{J}}$ is diagonal $\boldsymbol{\mathcal{J}}' = \boldsymbol{R}(\phi_i - \phi_j)\boldsymbol{\mathcal{J}}$. Since $\phi_i - \phi_j = (\boldsymbol{R}_i - \boldsymbol{R}_j)\cdot\boldsymbol{Q}$, for instance $\boldsymbol{\mathcal{J}}(ij)\cos(\phi_i - \phi_j)$ becomes $\frac{1}{2}(\boldsymbol{\mathcal{J}}(\boldsymbol{q}+\boldsymbol{Q}) + \boldsymbol{\mathcal{J}}(\boldsymbol{q}-\boldsymbol{Q}))$ under Fourier transformation. Similar for the rest of the elements and in summary:

$$\begin{aligned}
\mathcal{J}'_{xx}(\boldsymbol{q}) = \quad \mathcal{J}'_{yy}(\boldsymbol{q}) &= \frac{1}{2}(\mathcal{J}(\boldsymbol{q}+\boldsymbol{Q}) + \mathcal{J}(\boldsymbol{q}-\boldsymbol{Q})) \\
\mathcal{J}'_{xy}(\boldsymbol{q}) = -\mathcal{J}'_{yx}(\boldsymbol{q}) &= \frac{1}{2i}(\mathcal{J}(\boldsymbol{q}+\boldsymbol{Q}) - \mathcal{J}(\boldsymbol{q}-\boldsymbol{Q})) \\
\mathcal{J}'_{zz}(\boldsymbol{q}) = \quad \mathcal{J}_{zz}(\boldsymbol{q}) & \\
\mathcal{K}'_{22}(\boldsymbol{q}) = \mathcal{K}'_{-2-2}(\boldsymbol{q}) &= \frac{1}{2}(\mathcal{K}(\boldsymbol{q}+2\boldsymbol{Q}) + \mathcal{K}(\boldsymbol{q}-2\boldsymbol{Q})) \\
\mathcal{K}'_{2-2}(\boldsymbol{q}) = -\mathcal{K}'_{-22}(\boldsymbol{q}) &= \frac{1}{2i}(\mathcal{K}(\boldsymbol{q}+2\boldsymbol{Q}) - \mathcal{K}(\boldsymbol{q}-2\boldsymbol{Q})).
\end{aligned} \tag{A.21}$$

Upon rotation the dispersion relations in figure A.1 becomes simpler, as depicted in figure A.3. The overall form of the curve is roughly given by $-\mathcal{J}(\boldsymbol{q})$, whereas the gaps are effects of the *spin slip* structure. There are two spin slips during the ten single layers in a 1/5 structure, and they cause gaps in the magnon energies. Therefore the scattering from a 7/36 structure should have the same overall form due to the exchange coupling, but different (if any) spin gaps.

Figure A.3: Calculated scattering from a rotated 1/5 structure in $Ho_{90}Er_{10}$.

Appendix B

X-ray measurements

X-ray measurements have been performed on the $Ho_{90}Er_{10}$ crystal at the rotating anode, Risø in the period 18-22/7. Due to the last minute nature of the work, the results have not been thoroughly analyzed, and are therefore only reported in this appendix. Although ordinary x-ray scattering does not probe the magnetic structure, three questions could be addressed:

- The high resolution of an x-ray spectrometer could reveal the details of the nuclear peaks. A perfectly homogeneous random alloy with well defined effective lattice parameters would give a sharp symmetric peak. A crystal with composition fluctuations would give a peak, the shape of which reflects the lattice parameter distribution. In the extreme case of macroscopic clusters of Er, two distinct peaks should be observed.
- If the unexpected peak at $(0, 0, 1)$ occurring below 70 K was purely magnetic of origin, it would not be observed with x-rays. On the other hand, a peak due to lattice distortion should also be observed with x-rays.
- More generally, the improved resolution and intensity of x-ray measurements would enable an investigation of the magnetostrictive effects in the system. Magnetostriction is the coupling between the lattice and the magnetic structures.

B.1 Results

Since with x-ray scattering, the Bragg peaks can be resolved sufficiently to observe splitting and other effects, the definition of the lattice parameters and hence the *reciprocal lattice* units is not unambiguously defined. Therefore the results are reported in units of inverse Ångstroms. The relation to reciprocal lattice units is roughly: 1 rlu $\simeq 1.11$ Å^{-1}.

The two fundamental peaks at $(0, 0, 2)$ and $(0, 0, 4)$ were scanned in order to identify any splitting. As evident in figure B.1 the peaks are not ideally sharp and symmetric.

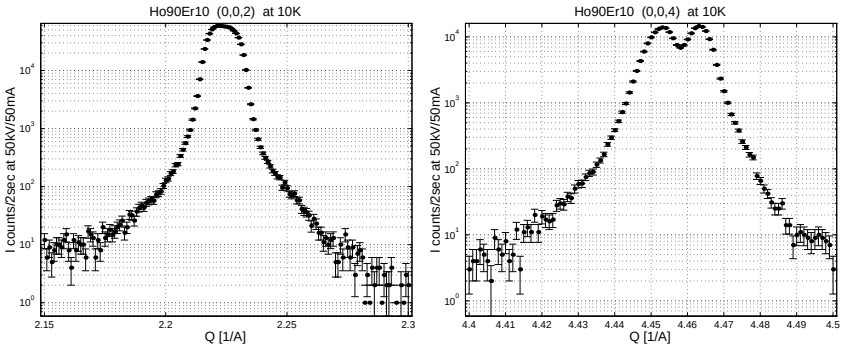

Figure B.1: X-ray scan of the peaks $(0, 0, 2)$ and $(0, 0, 4)$

The $(0, 0, 4)$ peak actually splits into two peaks separated by 0.01 Å. The rotating anode is tuned to the CuK_α, which actually contains two wavelengths corresponding to α_1 and α_2 respectively, and the splitting could simply be the two different incident wavelengths. However figure B.2 depicts that one of the two peaks around $(0, 0, 5)$ disappears, which could not be the case if it was an α splitting. Therefore the splitting of the $(0, 0, 4)$ peak is believed to reflect the existence of different lattice parameters in the crystal.

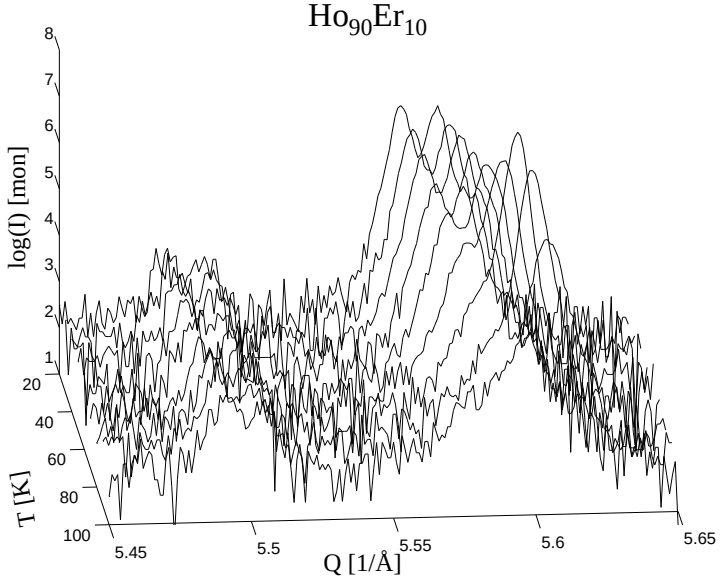

Figure B.2: X-ray scans around $(0, 0, 5)$.

Even a perfectly random alloy can not be completely uniform, since every

one out of ten atoms is an Er atom. This does introduce lattice distortions which might explain also the quite non trivial behaviour around the forbidden $(0, 0, 5)$ peak depicted in figure Although the details of the peaks is not immediately explainable, their presence proves, that lattice distortions do exist.

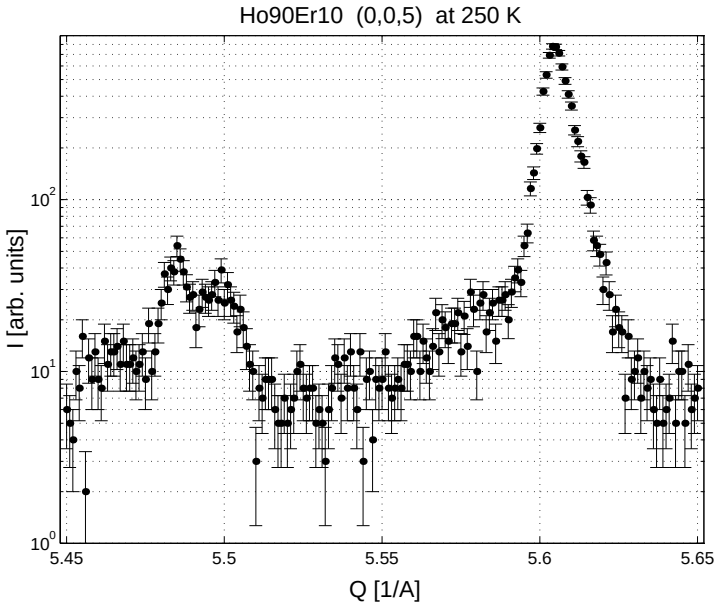

Figure B.3: X-ray scan around $(0, 0, 5)$ at 250 K.

Not depicted in figure B.2 is a scan at 250K, where the strongest peak still occur. This means, that it cannot be a lattice distortion caused by the magnetic ordering, which does not enter before $T_N = 125$ K. On is seen, that the other initially (at low temperatures) equally strong peak decays with increasing temperature, disappearing between 70 K and 80 K. this agrees with the decay of the unexpected $(0, 0, 1)$ peak in the neutron results. This suggests a magnetostrictive coupling between the lattice and the magnetic ordering. However if the two latter peaks are connected, it is not clear, why the first peak around $(0, 0, 5)$ does not appear in the neutron data.

Also the $(0, 0, 1)$ and $(0, 0, 3)$ peaks could be observed, although very faint. Scattering due to lattice distortions is proportional to Q^2, which could explain the low intensity of the $(0, 0, 1)$ and the $(0, 0, 3)$ peaks. But the $(0, 0, 3)$ should be positioned around 3.33 $\text{Å}^{-}1$, and the offset is not believed to be an alignment problem.

The overall conclusion of the x-ray results must be, that the alloying does introduce some distortions to the lattice, effectively breaking the symmetry slightly. A discussion of the type of lattice distortions and their connections to the composition of Ho and Er would require a thorough modeling and data analysis, for which the time was too short.

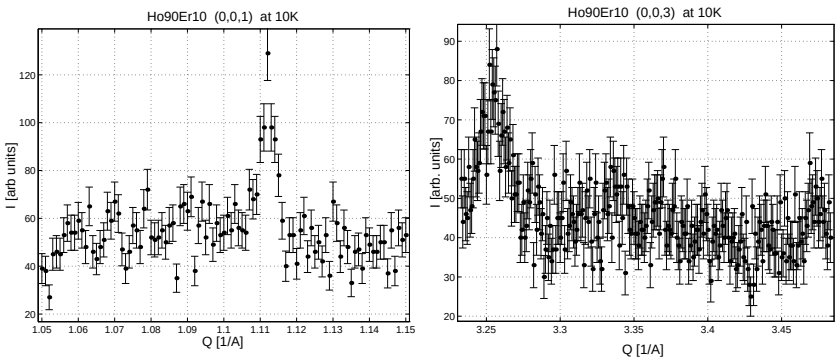

Figure B.4: X-ray scans of the peaks $(0, 0, 1)$ and $(0, 0, 3)$.

Bibliography

O. Andersen (1975),
Linear methods in band theory,
Phys. Rev. B **12**, 3060.

O. Andersen and O. Jepsen (1984),
Explicit, First-Principles Tight-Binding Theory,
Phys. Rev. Lett. **53**, 2571.

O. Andersen, O. Jepsen and D. Glötzel (1985),
Highlights of Condensed Matter Theory,
Horth Holland.

S. Bates, C. Patterson, G. McIntyre, S. Palmer, A. Mayer, R. Cowley and R. Melville (1988),
The magnetic structure of holmium: II,
J. Phys. C **21**, 4125–4141.

R. Bozorth, A. Clark and R. Gambino (1968),
Magnetization, Crystal Anisotropy and Fanning in Single Crystals of Ho-Er Alloys,
in *Proceedings of the Eleventh International Conference on Low Temperature Physics*, edited by J.F.Allen,
pp. 1106–1109.

R. Bozorth, A. Clark and J. van Vleck (1972),
Magnetic Crystal Anisotropies of Holmium-Erbium Alloys,
Intern. J. Magn. **2**, 19–31.

E. Callen and H. Callen (1965),
Magnetostriction, Forced Magnetostriction, and Anomalous Thermal Expansion in Ferromagnets,
Phys. Rev. **139**(2A), A455–A471.

N. Chesser and J. Axe (1972),
Derivation and Experimental Verification of the Normalized Resolution Function for Inelastic Neutron Scattering,
Acta Crystallogr. **A29**, 160+.

M. Cooper and R. Nathans (1967),
The Resolution Function in Neutron Diffractometry,
Acta Crystallogr. **23**, 357+.

R. Cowley and S. Bates (1988),
The magnetic structures of holmium: I,
J. Phys. C **21**, 4113–4124.

R. Cowley and J. Jensen (1992),
Magnetic structures and interactions in erbium,
J. Phys. C **4**, 9673+.

R. Cowley and J. Jensen (1993),
Non-Planar Magnetic Structures and Trigonal Interactions in Erbium,
Europhys. Lett. **21**(6), 705–710.

R. Elliot and F. Wedgwood (1964),
The temperature dependence of magnetic ordering in the heavy rare earth metals,
Proc. Phys. Soc. **84**, 63–75.

D. Gibbs, D. Harsmann, E. Isaacs, D. McWhan, D. Mills and C. Vettier (1988),
Polarization and Resonance Properties of Magnetic X-Ray Scattering in Holmium,
Phys. Rev. Lett. **61**(10), 1241–1244.

J. Hannon, G. Trammel, M. Blume and D. Gibbs (1988),
X-Ray Resonance Exchange Scattering,
Phys. Rev. Lett. **61**(10), 1245–1248.

P. Hohenberg and W. Kohn (1964),
Inhomogenous Electron Gas,
Phys. Rev. **136**, B864–B871.

B. Howard and J. Bohr (1991),
Binary Magnetic Structures in HoEr,
Phys. Scr. T **39**, 96.

J. Jensen (1974),
Anisotropic exchange interaction in the conical magnetic phase of erbium,
J. Phys. F **4**, 1065–1072.

J. Jensen (1996a),
Theory of comensurable magnetic structures in holmium,
To be published.

J. Jensen (1996b),
The three-fold symmetric two-ion coupling in the hcp rare-earth metals,
To be published.

J. Jensen and A. Mackintosh (1991),
Rare earth Magnetism: Structures and Excitations,
Oxford University Press.

J. Jensen and A. Mackintosh (1992),
Novel Magnetic Pahses in Holmium,
J. Magn. Magn. Mater **104**, 1481–1484.

S. Keeton and T. Loucks (1968),
Electronic Structure of Rare-Earth Metals. I. Relativistic Augmented-Plane-Wave Calculations,
Phys. Rev. **168**(3), 672–678.

W. Koehler, H. Child, E. Wollan and J. Cable (1963),
J. App. Phys. **34**, 1335.

W. Kohn and L. Sham (1965),
Self-Consistent Equations Including Exchange and Correlation Effects,
Phys. Rev. **140**, A1133–A1138.

C. Larsen (1987),
Magnetic Excitations in Heavy Rare Earth Alloys,
Ph.D. thesis,
Risø National Laboratory.

C. Larsen, J. Jensen and A. Mackintosh (1987),
Magnetic Excitations in Commensurable Periodic Structures,
Phys. Rev. Lett. **59**(6), 712–715.

C. Larsen, J. Jensen, A. Mackintosh and B. Beaudry (1988),
Spin dynamics of thulium ions in terbium,
J. Phys. (Paris) **49**, C8–331.

C. Larsen, A. Mackintosh, H. B. Møller, S. Legvold and B. Beaudry (1986),
Rare earth solutes and the magnetic properties of terbium,
J. Magn. Magn. Mater **54-57**, 1165–1166.

H. Lin, M. Collins, T. Holden and W. Wei (1992),
Magnetic structures of erbium,
Phys. Rev. B **45**(22), 12873–12883.

P.-A. Lindgård, B. Harmon and A. Freeman (1975),
Theoretical Magnon Dispersion Curves for Gd,
Phys. Rev. Lett. **35**(6), 383–386.

D. Pengra, N. Thoft, M. Wulff, R. Feidenhans'l and J. Bohr (1994),
Resonance-enhanced magnetic x-ray diffraction from a rare-earth alloy,
J. Phys. C **6**, 2409–2422.

D. Sherrington (1972),
Prediction of a Possible New Intermediate Spin Ordering in Holmium,
Phys. Rev. Lett. **28**(6), 364–367.

J. Simpson, D. McMorrow, R. Cowley and D. Jehan (1995),
Trigonal interactions in holmium,
Phys. Rev. B **51**(22), 16073–16082.

H. Skriver (1984),
The LMTO Method,
Springer-Verlag.

G. Squires (1978),
Thermal Neutron Scattering,
Cambridge University Press.

C. Zener (1951),
Interaction Between the d Shells in the Transition Metals,
Phys. Rev. **81**, 440–444.

C. Zener (1954),
Classical Theory of the Temperature Dependence of Magnetic Anisotropy Energy,
Phys. Rev. **96**, 1335–1337.

List of Figures

List of Tables

Index

ISBN 87-550-2221-9